Differential Canard Deflection for Generation of Yawing Moment on the X-31 With and Without the Vertical Tail

by

Matthew Robert Whiting

B.S. Aerospace Engineering, Dec. 1991, Parks College of Saint Louis University

A Thesis submitted to

The Faculty of

The School of Engineering and Applied Science
of The George Washington University in partial satisfaction
of the requirements for the degree of Master of Science

1/9/96

This research was conducted at NASA LaRC.

Abstract

The feasibility of augmenting the available yaw control power on the X-31 through differential deflection of the canard surfaces was studied as well as the possibility of using differential canard control to stabilize the X-31 with its vertical tail removed. Wind-tunnel tests and the results of departure criteria and linear analysis showed the destabilizing effect of the reduction of the vertical tail on the X-31. Wind-tunnel testing also showed that differential canard deflection was capable of generating yawing moments of roughly the same magnitude as the thrust vectoring vanes currently in place on the X-31 in the post-stall regime. Analysis showed that the X-31 has sufficient aileron roll control power that with the addition of differential canard as a yaw controller, the wind-axis roll accelerations will remain limited by yaw control authority. It was demonstrated, however, that pitch authority may actually limit the maximum roll rate which can be sustained. A drop model flight test demonstrated that coordinated, wind-axis rolls could be performed with roll rates as high as 50 deg/sec (full scale equivalent) at 50 deg angle of attack. Another drop model test was conducted to assess the effect of vertical tail reduction, and an analysis of using differential canard deflection to stabilize the tailless X-31 was performed. The results of six-degree-of-freedom, non-linear simulation tests were correlated with the drop model flights. Simulation studies then showed that the tailless X-31 could be controlled at angles of attack at or above 20 deg using differential canard as the only yaw controller.

Acknowledgments

The author would like to thank everyone at NASA Langley Research Center whose participation made this study possible. In particular, special recognition should go to the entire drop model team who worked together to make the drop model flights happen in the face of adversity. Specifically, thanks go to Mark Croom, who has been my mentor throughout this project, and Dr. Vladislav Klein, who has served as my academic advisor. The author would also like to make special mention of Kevin Cunningham, who made the simulator studies possible, and Lee Pollard for his excellent work on short notice assembling graphics.

Table of Contents

List of Symbols

C_D Drag coefficient

C_L Lift coefficient

$C_{L\,max}$ Maximum lift coefficient

C_l Rolling moment coefficient

C_{lp} Roll damping coefficient, $\frac{\partial C_l}{\partial\left(pb/2V_T\right)}$ (per rad)

C_{lr} Rolling moment coefficient due to yaw rate, $\frac{\partial C_l}{\partial\left(rb/2V_T\right)}$ (per rad)

$C_{l\beta}$ Dihedral Effect, $\frac{\partial C_l}{\partial \beta}$ (per deg or per rad)

$C_{l\delta a}$ Rolling moment coefficient due to aileron deflection, $\frac{\partial C_l}{\partial \delta a}$ (per deg)

$C_{l\delta r}$ Rolling moment coefficient due to rudder deflection, $\frac{\partial C_l}{\partial \delta r}$ (per deg)

C_m Pitching moment coefficient

$C_{m\alpha}$ Pitch stiffness, $\frac{\partial C_m}{\partial \alpha}$ (per deg or per rad)

C_n Yawing moment coefficient

C_{np} Yawing moment coefficient due to roll rate, $\frac{\partial C_n}{\partial\left(pb/2V_T\right)}$ (per rad)

C_{nr} Yaw damping coefficient, $\frac{\partial C_n}{\partial\left(rb/2V_T\right)}$ (per rad)

$C_{n\beta}$ Static directional stability, $\frac{\partial C_n}{\partial \beta}$ (per deg or per rad)

$C_{n\beta,\,dyn}$ Directional divergence parameter (per deg)

$C_{n\delta a}$ Yawing moment coefficient due to aileron deflection, $\frac{\partial C_n}{\partial \delta a}$ (per deg)

$C_{n\delta r}$ Yawing moment coefficient due to rudder deflection, $\frac{\partial C_n}{\partial \delta r}$ (per deg)

C_Y Sideforce coefficient

C_{Y_p} Sideforce coefficient due to roll rate, $\frac{\partial C_Y}{\partial\left(pb/2V_T\right)}$ (per rad)

C_{Y_r} Sideforce coefficient due to yaw rate, $\frac{\partial C_Y}{\partial\left(rb/2V_T\right)}$ (per rad)

$C_{Y\beta}$ Sideforce coefficient due to sideslip, $\frac{\partial C_Y}{\partial \beta}$ (per deg or per rad)

$C_{Y\delta a}$ Sideforce coefficient due to aileron deflection, $\frac{\partial C_Y}{\partial \delta a}$ (per deg)

$C_{Y\delta r}$ Sideforce coefficient due to rudder deflection, $\frac{\partial C_Y}{\partial \delta r}$ (per deg)

$\overline{C}_{lp}$ Roll Damping Parameter from Forced Oscillation Test, $C_{lp} + C_{l\beta}\sin(\alpha)$

$\overline{C}_{nr}$ Yaw Damping Parameter from Forced Oscillation Test, $C_{nr} - C_{n\beta}\cos(\alpha)$

D Drag force, $\bar{q}SC_D$ (lbs)

F_T Thrust (lbs)

g Acceleration of gravity (ft/sec^2)

I_X Moment of inertia about the X axis (slug ft^2)

I_{XZ} Cross moment of inertia (slug ft^2)

I_Y Moment of inertia about the Y axis (slug ft^2)

I_Z Moment of inertia about the Z axis (slug ft^2)

K_{SRI} Roll stick to rudder interconnect gain

L Lift force or rolling moment, $\bar{q}SC_L$ (lbs) or $\bar{q}SbC_l$ (ft lbs)

L_p Rolling moment due to roll rate, $\frac{\bar{q}Sb^2C_{lp}}{2V_T}$ (ft lbs per rad/sec)

L_r Rolling moment due to yaw rate, $\frac{\bar{q}Sb^2C_{lr}}{2V_T}$ (ft lbs per rad/sec)

L_β Rolling moment due to sideslip, $\bar{q}SbC_{l\beta}$ (ft lbs per rad)

$L_{\delta a}$ Rolling moment due to aileron deflection, $\bar{q}SbC_{l\delta a}$ (ft lbs per deg)

$L_{\delta r}$ Rolling moment due to rudder deflection, $\bar{q}SbC_{l\delta r}$ (ft lbs per deg)

m Mass (slug)

M Pitching moment, $\bar{q}S\bar{c}C_m$ (ft lbs)

N Yawing moment, $\bar{q}SbC_n$ (ft lbs), or linear dimensional scale factor

N_p Yawing moment due to roll rate, $\frac{\bar{q}Sb^2C_{np}}{2V_T}$ (ft lbs per rad/sec)

N_r Yawing moment due to yaw rate, $\frac{\bar{q}Sb^2C_{nr}}{2V_T}$ (ft lbs per rad/sec)

N_β Yawing moment due to sideslip, $\bar{q}SbC_{n\beta}$ (ft lbs per rad)

$N_{\delta a}$ Yawing moment due to aileron deflection, $\bar{q}SbC_{n\delta a}$ (ft lbs per deg)

$N_{\delta r}$ Yawing moment due to rudder deflection, $\bar{q}SbC_{n\delta r}$ (ft lbs per deg)

q Body axis pitch rate (deg/sec or rad/sec) (see Fig. 1)

$\bar{q}$ Dynamic pressure (psf)

p Body axis roll rate (deg/sec or rad/sec) (see Fig. 1)

r Body axis yaw rate (deg/sec or rad/sec) (see Fig. 1)

S Wing reference area (ft^2)

U_0 Initial x component of airspeed (ft/sec)

u X component of airspeed (ft/sec) (see Fig. 1)

V_D Sink rate (ft/sec)

V_T Total airspeed (ft/sec)

v Y component of airspeed (ft/sec) (see Fig. 1)

W Weight (lbs)

W_0 Initial z component of airspeed (ft/sec)

w Z component of airspeed (ft/sec) (see Fig. 1)

Y Sideforce, $\overline{q}SC_Y$ (lbs)

Y_p Sideforce due to roll rate, $\frac{\overline{q}SbC_{Y_p}}{2V_T}$ (lbs per rad/sec)

Y_r Sideforce due to yaw rate, $\frac{\overline{q}SbC_{Y_r}}{2V_T}$ (lbs per rad/sec)

Y_β Sideforce due to sideslip, $\overline{q}SC_{Y_\beta}$ (lbs per rad)

$Y_{\delta a}$ Sideforce due to aileron deflection, $\overline{q}SC_{Y_{\delta a}}$ (lbs per deg)

$Y_{\delta r}$ Sideforce due to rudder deflection, $\overline{q}SC_{Y_{\delta r}}$ (lbs per deg)

$Y_{\delta v}$ Sideforce due to thrust vectoring, $\frac{\partial Y}{\partial \delta v}$ (lbs per deg)

α Angle of attack (deg or rad)

β Sideslip angle (deg or rad)

δa Aileron deflection (deg)

δdc Differential canard deflection (deg)

δf Flap deflection (deg)

δ_j Isentropic jet turning angle (deg)

δr Rudder deflection (deg)

δv Thrust Vectoring Vane Deflection (deg)

ϕ Bank angle (deg or rad)

γ Glideslope, positive descending (deg)

θ_0 Initial pitch angle (deg)

σ Ratio of model to full scale air density

Abbreviations

FCL Flight Control Law

LCDP Lateral control divergence parameter (per deg)

PCM Pulse Code Modulation

List of Tables

List of Figures

1. Introduction

Historically, the evolution of fighter aircraft has involved a steady progression in higher speeds and engagement of targets at longer ranges. Modern fighters are now capable of engaging targets beyond visual range, more than 90 miles away in some cases.[1] However, the capability to attack targets at long range does not preclude the possibility that close range engagements will still occur. In today's arena of combat, rules of engagement may require visual identification of targets, and the advent of stealth technologies may severely close the distance at which target aircraft may be detected. It has become apparent that the next generation of fighter designs will be driven by new technologies that allow them to survive in close range air-to-air combat.[2] Within-visual-range combat requires high levels of agility to maneuver into firing position (and out of a vulnerable position) as quickly as possible. It has also been demonstrated that a tactical advantage can be gained through all-aspect nose pointing, or the ability to point the aircraft without regard to the direction of the velocity vector.[3] This ability requires fully controlled flight at angles of attack well into the post-stall region.

Controlled post-stall flight is a significant aerodynamic challenge. The concept of all-aspect nose pointing requires not only a pitch-up to high angle of attack but also the ability to perform controlled rolls about the wind-axis with high turning rates. As the angle of attack increases, the yawing moment required to perform a wind-axis roll quickly increases while the body axis rolling moment required decreases. This increase in yawing moment demand occurs while the amount of yawing moment available from conventional

means (e.g. rudders) is decreasing becauase the vertical tails and rudders are immersed in the low energy wake of the wing and fuselage. This problem can be compounded by asymmetric vortices which may develop around the forebody at high angles of attack.[4] The yawing moment produced by these flow asymmetries would place a further demand on the lateral-directional controllability which can limit the turning rates available or even cause a nose-slice departure where the asymmetry exceeds the available yaw control authority and the aircraft diverges into a possible spin entry condition.[5]

Another factor which has recently become a major driver in fighter design is stealth technology.[6] Key to the radar cross section and visual observability is the profile silhouette and the vertical tail is one of the major contributors to this profile.[7] This has created an interest in aircraft designs with reduced vertical tails or no vertical tail at all (e.g. the B-2 aircraft), and the unconventional yaw controls required to stabilize these designs.

Elimination of the need for a vertical tail surface would add a new element of design freedom which could be exploited for improved performance. For example total aircraft weight could be reduced by removing the vertical tail surface provided the method used to generate yaw control weighs less than the vertical tail and rudder control components. Possibly trim drag could be reduced resulting in better cruise efficiency.

Since, as stated previously, the vertical tail surfaces tend to lose effectiveness in the wake of the wings, reducing the vertical tail surfaces may not strongly affect the stability of the aircraft at high angles of attack. However, excursions into the post-stall regime are expected to be infrequent and of short duration. Most flying, particularly

take-off and landing, will still take place at lower angles of attack where the vertical tails and rudders are relied on for lateral-directional stability and control.

The ineffectiveness of vertical surfaces at high angles of attack and the desire to reduce or remove them for stealth or performance reasons has created an increasing demand for alternate yaw control methods. Recent studies have looked into forebody vortex controls such as nozzle blowing or actuated strakes,[8] but these methods have focused on the post-stall regime. Many high-angle-of attack flight programs have relied on thrust vectoring to achieve yaw control power, and it has been shown that thrust vectoring should be sufficient to provide directional stability at low angles of attack for aircraft with reduced vertical tails.[7,9] However, these methods require functioning thrust vectoring actuators and engines operating at high levels of thrust. If a failure were to occur in either of these systems, the aerodynamic instability of the tailless airframes could create an unrecoverable situation, and an alternate form of yaw control to provide redundancy would be desirable.

This study investigates differential canard control--a purely aerodynamic yaw control method which may be available for future aircraft designs. Previous studies[10,11] have shown that differential deflection of canard surfaces has the potential to produce significant yawing moments, and in this study, this potential is investigated in some detail for a particular airframe, the X-31. First the effect of reducing or removing the vertical tail from the X-31 as studied in wind-tunnel tests will be described. The data from these tests are applied to the linear equations of motion as well as divergence criteria to determine the influence of the vertical tail on the controllability of the aircraft. Then

wind-tunnel data demonstrating the control power of differential canard deflection are presented to qualify the effectiveness of differential canards as a yaw controller. With that information, the differential canard control authority is considered, along with the other aerodynamic controls available to determine whether yaw, roll, or pitch control would saturate first to become the limiting factor for turn performance. The results of drop model flight tests are shown to correlate with the wind-tunnel predictions for differential canard control power and controllability with reduced vertical tail. Finally, a simulator study is described which demonstrates the success of the six-degree-of-freedom, nonlinear simulation in predicting drop model behavior, and control laws are developed for that simulation to control the X-31 with its vertical tail removed.

2. The X-31

The X-31 is a lightweight, experimental fighter designed as part of the Enhanced Fighter Maneuverability program to study the tactical advantages of post-stall maneuvering. It is a delta wing-canard configuration with a single vertical tail and a single engine with three thrust vectoring vanes. The X-31 has a low wing with a planform illustrated in Fig. 2. The wing has a pair of leading edge flaps, segmented at the point of the change in leading edge sweep, which are used for high-angle-of-attack lift augmentation. The wing also has a pair of trailing edge devices on each side. These surfaces are normally used together as if they were a single pair of flaperons for pitch and roll and will be referred to in this paper as the flaps (symmetric deflection) and the ailerons (asymmetric deflection). The single vertical tail on the X-31 is shown in Fig. 3.

The X-31 has had a very successful flight test program and has performed extremely well throughout its flight envelope which includes angles of attack as high as 70 deg. Recently, interest was raised in using the thrust vectoring system normally reserved for post-stall control to stabilize the X-31 with a reduced vertical tail. In fact, flight tests were conducted using the quasi-tailless technique in which the flight control system uses destabilizing feedback to the rudder to simulate a reduced tail aircraft; these tests demonstrated that thrust vectoring should be sufficient to control the X-31 with a reduced vertical tail.[9] However, complete reliance on thrust vectoring for stability on a single engine aircraft creates a situation where a single string failure could eliminate

controllability. This report investigates the use of differential canard to provide redundancy and satisfy this flight safety issue.

The results described in this study were obtained using a 13.3% scale model of the X-31 in Langley's 12-Foot Low Speed Tunnel, a 19% scale model in Langley's 30- by 60-Foot Tunnel, and a 27% dynamically scaled drop model. A three-view drawing of the X-31 is shown in Fig. 4, and the dimensions of its primary components are described in Tables 1 and 2, in which the coordinate system used for dimensions declared as FS, BL, or WL is illustrated in Fig. 5. Table 3 lists the relationship between full scale and dynamically scaled models for various dimensional quantities.

The all-moving canards are normally only deflected symmetrically, for pitch control, but because this paper will investigate the effect of asymmetrically deflected canard surfaces, the deflections of the canards include both symmetric and differential deflections. Canard deflections are given in degrees with trailing edge down deflections considered positive. Symmetric canard deflection, δc, is defined as (right canard + left canard)/2, and differential deflection of the canard will be referred to as δdc which is defined as (right canard - left canard)/2.

The position of the leading edge flaps is given in this paper in degrees of leading edge down deflection normal to the hinge line as (inboard)/(outboard).

The positions of the trailing edge devices referred to in this paper will be given for flaps and ailerons separately where flap deflection, δf, is defined as (right trailing edges + left trailing edges)/2 and aileron deflection, δa, is defined by (right trailing edges - left

trailing edges)/2. The angles given are in degrees of deflection with positive being trailing edge down for each surface.

Unless stated otherwise, the baseline configuration as it was tested for this study had the following characteristics, where the names of specific components used during the original wind-tunnel testing are specified in parentheses:

Symmetric Canards, δc: -40 (40 deg symmetric trailing edge up).

Leading Edge Flaps: 40/32 (40 deg inboard, 32 deg outboard leading edge down).

Trailing Edge Flaps, δf: 0 (0 deg symmetric deflection).

Ailerons, δa: 0 (0 deg symmetric deflection).

Nose Boom: (J13) projects to -79.2 FS with -4 deg incidence.

Leading Edge Strakes: (M86) about 5.3 inches wide, extending forward to 148 FS from the leading edges of the wings similar to a leading edge extension.

Nose Strakes: (5B) 0.6 inches wide by 20 inches long.

Aft Strakes: 6 inches wide by 65 inches long. They are placed at an incidence of 11 deg with no dihedral.

Inlet Lip: closed (0 deflection).

Thrust Vectoring Vanes: nominal position.

Nose Radius: 0.6"

Fig. 6 shows the basic longitudinal areodynmaic characteristics of the X-31 as tested with the 19% scale model in the 30- by 60-Foot Tunnel with two different symmetric canard settings. The X-31 has a maximum lift coefficient, $C_{L\,max}$, of about 1.2

at 32 deg angle of attack. This configuration is designed to be statically unstable in trimmed, subsonic flight at low angles of attack in order to improve transonic performance.

The full series of data for the effect of incremental vertical tail reduction on lateral-directional static stability is only available from the 12-Foot Low Speed Tunnel, so a comparison of the results between the separate tests is made in Fig. 7. The figure shows good agreement in the data for C_{l_β} and C_{Y_β} throughout the angle-of-attack range and in C_{n_β} for angles of attack above 60 deg and below 40 deg. In the range from 40 to 60 deg angle of attack, however, the results from the 13.3% scale model test are shown to be significantly more stable in static directional stability, C_{n_β}, than the 19% scale model test. Because of this discrepancy, stability analyses are made based on data from the test in the 30- by 60-Foot Tunnel where superior flow quality and model accuracy produce results more representative of the full scale aircraft. Fig. 8 shows that the change in C_{n_β} which occurs when the vertical tail is reduced from 100% to 20% does correlate well between the separate wind-tunnel tests. Therefore, the data from the full series of vertical tail sizes from the 13.3% scale model test will be shown with the understanding that the incremental effect of each step in the vertical height reduction would be expected to correlate with data obtained for the 19% scale model in the larger wind-tunnel.

3. Vertical Tail Reduction

The lateral-directional stability of the X-31 aircraft in its basic configuration with 100% vertical tail has regions of instability both in static directional stability, C_{n_β}, and dihedral effect, C_{l_β}. As can be seen in Fig. 7, the X-31 is directionally stable at angles of attack below 20 deg and between 32 deg and 45 deg. On the other hand, C_{l_β} is stable except at angles of attack below 10 deg where a very slight instability can be seen. The X-31 was not originally designed with the intention of removing its vertical tail and rudder, and with the directional stability already negative in some regions, there is some concern about the impact of the reduction of the vertical tail surface. To address this issue, the vertical tail surface was reduced in several stages and tested to assess the contribution of each section to the overall lateral-directional stability. The vertical tail was reduced by cutting the tail along a horizontal line at a given height as shown in Fig. 3, and is expressed in terms of percent of the full size tail. The tail height is measured from the bottom of the spin chute compartment which itself represents 20% of the total vertical tail. It may be noted that the spin chute housing is an integral part of the airframe and is not likely to be removed from the full scale aircraft; therefore, methods to control the "tailless" aircraft were tested with 20% vertical tail surface. The spin chute housing was removed for the purposes of the wind-tunnel testing only and is shown as the 0% tail configuration.

3.1 Static Wind-Tunnel Testing

Fig. 9 shows the effect on static lateral-directional stability of stepwise reduction of the vertical tail surface. At 0 deg angle of attack the relationship between vertical tail height and $C_{n\beta}$ is highly linear. $C_{n\beta}$ varies from almost 0.002 with the full tail to almost -0.004 with no tail at all, crossing the stability boundary between 80% and 60% tail. By 15 deg angle of attack, however, the contribution of the lowest 40% of the tail is no longer significant. Surprisingly, at angles of attack between 24 deg to 34 deg, the 20% and 0% configurations are actually more stable than even that with 60% vertical tail; which may be due to a cross flow at the vertical tail location, but this phenomenon was not studied further. At 50 deg angle of attack, the vertical tail becomes completely immersed in the wing wake, and any contribution to $C_{n\beta}$ is essentially negligible. In fact, the minimal effect of the vertical tail appears to be destabilizing in this angle of attack range.

The impact of the vertical tail reduction on $C_{l\beta}$ is more predictable. In the low angle of attack range from 0 deg to 30 deg there appears to be a linear relationship between $C_{l\beta}$ and vertical tail height from 100% down to 40% below which the contribution is minimal. At angles of attack above 30, the vertical tail does not have a significant effect on $C_{l\beta}$.

In the high angle of attack range from 40 deg to 70 deg, which is within the flight envelope of the X-31, the data in Fig. 9 showed that reduction of the vertical tail caused no detriment in performance since it is completely blanketed behind the wing. In the low angle of attack range from 0 deg to 20 deg, however, it is seen that reducing the tail

would be extremely destabilizing. To maintain positive levels of C_{n_β}, at least 80% of the vertical tail height must be intact. Further reduction of the tail would create the need for augmentation of the lateral-directional stability through some other means. As reduction of the vertical tail height necessarily means reduction of the rudder as well, some control method other than the conventional rudder would be required in order to achieve the 20% tail, which is the goal for the "tailless" configuration. It has been shown that the thrust vectoring system already in use on the X-31 should be sufficient to maintain controlled flight without the vertical tail,[9] but flight safety issues prohibit total reliance on thrust vectoring for stability. It would therefore be desirable to have an alternate method of control to provide redundancy in the event of an engine or vectoring failure.

3.2 Forced Oscillation Wind-Tunnel Testing

The effect of the vertical tail on the static stability parameters was shown to be quite profound, but the effects on dynamic stability are also of importance. Forced oscillation wind-tunnel tests were conducted with the 19% scale model in the 30- by 60-Foot Tunnel to study the influence of the vertical tail on the dynamic lateral-directional stability. Fig. 10 shows that the vertical tail's contribution to roll damping, $\overline{C}_{l_p}$, is decidedly minimal, however as would be expected, Fig. 11 shows that the yaw damping, $\overline{C}_{n_r}$, is greatly reduced below 30 deg angle of attack by removing the vertical tail. Rather surprising are the results from 32 deg to 65 deg angle of attack which show that reduction of the vertical tail actually improves the yaw damping somewhat. This could be due to a cross flow phenomenon at the vertical tail, but since this does not

correlate to a similar effect in the static stability, it is more likely due to an unsteady flow effect.

3.3 Equations of Motion

To interpret the overall effect on lateral-directional stability of the vertical tail, the linearized, decoupled equations of motion (Reference 12) will now be analyzed for both the 100% and 20% vertical tails. The sideforce equation

$$m(\dot{v} + U_0 r - W_0 p) = mg\sin(\phi)\cos(\theta_0) + Y,$$

solved for the time rate of change of the y component of airspeed is

$$\dot{v} = g\sin(\phi)\cos(\theta_0) - U_0 r + W_0 p + \frac{Y}{m}.$$

Differentiating the relation

$$\sin(\beta) = \frac{v}{V_T}$$

results in the expression

$$\dot{\beta}\cos(\beta) = \frac{\dot{v}V_T - v\dot{V}_T}{V^2_T}.$$

Applying the small angle assumption to ϕ and assuming that $\dot{V}_T = 0$ to decouple the lateral-directional part of the equation, this expression becomes

$$\dot{\beta} = \frac{g\cos(\theta_0)}{V_{T0}\cos(\beta)}\phi - \frac{U_0}{V_{T0}\cos(\beta)}r + \frac{W_0}{V_{T0}\cos(\beta)}p + \frac{Y}{mV_{T0}\cos(\beta)}.$$

Applying the small angle assumption to β, this can be reduced to

$$\dot{\beta} = \frac{g\cos(\theta_0)}{V_{T0}}\phi + \sin(\alpha_0)p - \cos(\alpha_0)r + \frac{Y}{mV_{T0}}.$$

The equation for the time rate of change of the bank angle is given by

$$\dot{\phi} = p + \tan(\theta_0)[q\sin(\phi) + r\cos(\phi)],$$

which can be linearized by assuming small perturbations to

$$\dot{\phi} = p + \tan(\theta_0)r.$$

The relationship between the lateral-directional components of angular acceleration and aerodynamic moments is given by the equations

$$L = Ix\dot{p} - Ixz\dot{r}$$

$$N = Iz\dot{r} - Ixz\dot{p}.$$

Which can be solved for the angular accelerations

$$\dot{p} = \frac{IzL + IxzN}{IxIz - I^2xz}$$

$$\dot{r} = \frac{IxzL + IxN}{IxIz - I^2xz}.$$

If we define the lateral-directional states to be x,

$$x = \begin{bmatrix} \beta \\ \phi \\ p \\ r \end{bmatrix}$$

and the standard lateral-directional controls to be u,

$$u = \begin{bmatrix} \delta a \\ \delta r \end{bmatrix}$$

we can write the full decoupled, linearized, lateral-directional equations of motion as follows:

$$\dot{x} = \begin{bmatrix} \frac{Y_\beta}{mV_{T_0}} & \frac{g\cos(\theta_0)}{V_{T_0}} & \frac{Y_p}{mV_{T_0}} + \sin(\alpha_0) & \frac{Y_r}{mV_{T_0}} - \cos(\alpha_0) \\ 0 & 0 & 1 & \tan(\theta_0) \\ \frac{IzL_\beta + IxzN_\beta}{IxIz - I^2xz} & 0 & \frac{IzL_p + IxzN_p}{IxIz - I^2xz} & \frac{IzL_r + IxzN_r}{IxIz - I^2xz} \\ \frac{IxzL_\beta + IxN_\beta}{IxIz - I^2xz} & 0 & \frac{IxzL_p + IxN_p}{IxIz - I^2xz} & \frac{IxzL_r + IxN_r}{IxIz - I^2xz} \end{bmatrix} x + \begin{bmatrix} \frac{Y_{\delta a}}{mV_{T_0}} & \frac{Y_{\delta r}}{mV_{T_0}} \\ 0 & 0 \\ \frac{IzL_{\delta a} + IxzN_{\delta a}}{IxIz - I^2xz} & \frac{IzL_{\delta r} + IxzN_{\delta r}}{IxIz - I^2xz} \\ \frac{IxzL_{\delta a} + IxN_{\delta a}}{IxIz - I^2xz} & \frac{IxzL_{\delta r} + IxN_{\delta r}}{IxIz - I^2xz} \end{bmatrix} u$$

As will be shown later, the "tailless" X-31 was controlled in flight simulation down to 20 deg angle of attack. Therefore this example will be carried out for this flight condition. With the baseline configuration previously described, the wind-tunnel data shows the following stability derivatives at 20 deg angle of attack:

	Vertical Tail	
	100%	20%
C_{l_β} (1/deg)	-0.00204	-0.000180
C_{n_β} (1/deg)	0.00295	-0.00374
C_{Y_β} (1/deg)	-0.0180	-0.0124
C_{l_p} (1/rad)	-0.228	-0.254
C_{n_p} (1/rad)	-0.0260	-0.142
C_{Y_p} (1/rad)	0.0732	0.405
C_{l_r} (1/rad)	0.328	0.303
C_{n_r} (1/rad)	-0.830	-0.00780
C_{Y_r} (1/rad)	1.40	-0.321

$C_{Y_{\delta a}}$ (1/deg)	0.00271
$C_{l_{\delta a}}$ (1/deg)	-0.00287
$C_{n_{\delta a}}$ (1/deg)	-0.000445
$C_{Y_{\delta r}}$ (1/deg)	0.00202
$C_{l_{\delta r}}$ (1/deg)	0.000327
$C_{n_{\delta r}}$ (1/deg)	-0.00126

Because flight testing was conducted with the 27% scale drop model, and simulations of that drop model were conducted, the control laws developed in this study were designed for this scale. Therefore the linearized equations of motion will be evaluated for the 550 lb, unpowered model. Assuming a dynamic pressure of 38.4 psf which corresponds to descending trim flight at an angle of attack of 20 deg and an altitude of 5000 ft, the lateral-directional equations of motion for the drop model become:

$$\begin{bmatrix} \dot{\beta} \\ \dot{\phi} \\ \dot{p} \\ \dot{r} \end{bmatrix} = \begin{bmatrix} -0.1968 & 0.1659 & 0.3422 & -0.9355 \\ 0 & 0 & 1.0 & 0.060 \\ -3.890 & 0 & -0.1208 & 0.1754 \\ 0.0054 & 0 & -0.0001 & -0.0033 \end{bmatrix} \begin{bmatrix} \beta \\ \phi \\ p \\ r \end{bmatrix} + \begin{bmatrix} 0.0005 & 0.0004 \\ 0 & 0 \\ -0.0955 & 0.0110 \\ -0.0001 & -0.0003 \end{bmatrix} \begin{bmatrix} \delta a \\ \delta r \end{bmatrix}$$

for the 100% vertical tail, which have open loop poles at

$$0.0683 \pm 1.191i,$$

$$-0.4544, \text{ and}$$

$$-0.0030.$$

The lateral-directional equations of motion for the 20% vertical tail are

$$\begin{bmatrix} \dot{\beta} \\ \dot{\phi} \\ \dot{p} \\ \dot{r} \end{bmatrix} = \begin{bmatrix} -0.1357 & 0.1659 & 0.3433 & -0.9407 \\ 0 & 0 & 1.0 & 0 \\ -0.3164 & 0 & -0.1340 & 0.1605 \\ -0.0518 & 0 & -0.0005 & -0.0001 \end{bmatrix} \begin{bmatrix} \beta \\ \phi \\ p \\ r \end{bmatrix} + \begin{bmatrix} 0.0005 \\ 0 \\ -0.0955 \\ -0.0001 \end{bmatrix} [\delta a],$$

which have open loop poles at

$$0.0706 \pm 0.3457i,$$

$$-0.3803, \text{ and}$$

$$-0.0307.$$

Therefore, with the loss of the vertical tail, the unstable mode has been further destabilized. This is indicated both the the movement of the unstable pair away from the imaginary axis as well as the significant reduction of unstable damping ration. As will be shown later, the effect on the closed loop poles due to the loss of the rudder further compounds the problem.

3.4 Dynamic Divergence Parameters

In addition to the static and dynamic aerodynamic derivatives, there are two calculated parameters, the directional divergence parameter $C_{n\beta,\,dyn}$ and the lateral control divergence parameter LCDP, which have been successful at predicting departure susceptibility.[13]

$$C_{n\beta,\,dyn} = C_{n\beta}\cos(\alpha) - \frac{I_Z}{I_X} C_{l\beta}\sin(\alpha)$$

$$LCDP = C_{n\beta} - C_{l\beta}\left(\frac{C_{n\delta a} + K_{SRI} C_{n\delta r}}{C_{l\delta a} + K_{SRI} C_{l\delta r}}\right)$$

where K_{SRI} refers to the roll stick to rudder interconnect gain. Fig. 12 shows the values of $C_{n\beta,\,dyn}$ for the X-31 with both the 100% and 20% vertical tails, and the values of LCDP are shown in Fig. 13. The values of $C_{n\beta,\,dyn}$ are plotted against the corresponding LCDP for the 100% vertical tail in Fig. 14 and the 20% vertical tail in Fig. 15. As these figures of the departure criteria described in reference 13 show, the X-31 with 100% vertical tail is expected to be departure free until the loss of rudder control effectiveness at 50 deg angle of attack results in a negative LCDP where a "mild initial yaw departure followed by roll reversal" is expected. For the case of the 20% vertical tail, however, the loss of

the rudder has resulted in a negative LCDP over nearly the entire range of angle of attack. This is expected to produce a "mild initial yaw departure followed by roll reversal" at the higher angles of attack, but below 25 deg angle of attack, $C_{n\beta,dyn}$ becomes negative with the loss of the vertical tail, and a "strong directional divergence with roll reversal" is anticipated.

It is evident that some kind of yaw control device will be required to stabilize the tailless X-31 throughout the angle-of-attack range, and with 100% vertical tail, the yawing moment capability will have to be augmented in order to prevent departures above 45 deg angle of attack. Whereas the full-scale aircraft relies on thrust vectoring to generate additional yawing moments, this paper investigates the possibility of using differential deflection of the canards to produce the required yawing moment aerodynamically.

4. Wind-Tunnel Testing of Differential Canard Control

The X-31 has a pair of canards which are normally deflected symmetrically for pitch control, but the fact that they move in the same direction is merely the result of the flight control system. On the full scale aircraft, there exist separate actuators which are capable of driving the canards independently of each other. It has been shown in previous studies that asymmetrically deflected canards can create yawing moments on other aircraft.[10,11] These studies demonstrated that configurations with tall fuselage shapes at the position of the differential canard showed higher differential canard control power than those with wide fuselages. The similarity in the fuselage shapes between the X-31 and configuration A in Fig. 16[11] points to the strong possibility that differential canards would be effective as a yaw controller on the X-31.

If asymmetric deflection of the canards produces significant yawing moments, it is possible that they may be used as a lateral-directional control on the X-31 with a minimum of modification to the actual aircraft. Differential canard deflection was tested initially in the 12-Foot Low Speed Tunnel. Combinations which showed promise were tested more thoroughly in the 30- by 60-Foot Tunnel, and the results shown are from this latter test.

The data of Fig. 17 show the results of deflecting the left (port) canard trailing edge up and the right (starboard) canard trailing edge down by equal amounts away from the baseline -40 deg symmetric canard deflection with the full size vertical tail in place. In the low angle of attack range (0 deg to 20 deg), a significant amount of negative

yawing moment is produced. The data show no dead band down to differential deflections as small as 5 deg and control power which remains unsaturated at 30 deg. The amount of control power available does vary highly with angle of attack even within this range. The 30 deg δdc case produces negative ΔC_n which improves from -0.015 at 0 deg alpha to -0.03 at 20 deg angle of attack.

The resulting incremental pitching moment, ΔC_m, in this angle-of-attack range does not become significant until 20 deg deflection. However, any deflection creates a small, positive rolling moment, ΔC_l which increases as ΔC_n does with angle of attack to a peak of 0.0075 for the 30 deg δdc case.

At higher angles of attack (40 deg to 80 deg), Fig. 17 shows yawing moments far greater than those seen in the low angle of attack range. The 30 deg δdc case produces ΔC_n from -0.05 at 40 deg angle of attack to -0.06 at 80 deg with a peak of -0.09 at 60 deg angle of attack. As was the case in the low angle of attack range, the data shows no dead band with differential deflections as small as 5 deg and no saturation with 30 deg .

As with the low alpha case, the resulting rolling moments, although they are adverse in this range, only reach -0.075. The pitch up effect with 20 deg or more deflections is smaller than that seen at low angle of attack and fades away completely by 65 deg angle of attack.

The angle of attack range from 20 to 40 deg shows a distinct loss of yaw control power particularly near stall where ΔC_n becomes virtually negligible. Based on the data in some of the other curves within Fig. 17, it is curious that this minimum in ΔC_n occurs at the same time as a maximum in the sideforce, ΔC_Y. This indicates that while

differential canard deflection generates significant levels of side force, the center of pressure of that side force has moved back almost to the center of gravity. This is also evidenced by the behavior of the ΔC_l curve at that same point. A reversal in the rolling moment effect occurs at 20 deg angle of attack (the same point where ΔC_n begins to decrease) and reaches a strong peak at 34 deg angle of attack (the center of the low ΔC_n range). At angles of attack immediately above that, the ΔC_l effect reverses again until 45 deg angle of attack where the final reversal occurs.

Flow visualization tests were conducted in the 12-Foot Low Speed Tunnel using smoke and a laser sheet to study this phenomenon further. Most of the yawing moment would be expected to be caused by the difference in pressure near each canard acting against the side of the fuselage well ahead of the center of gravity. However, the flow visualization shows that unexpected behavior of the vortices generated by the canards as they continue aft is responsible for the strong effects seen in the mid angle of attack range. Figs. 18, 19, and 20 show a series of illustrations for this configuration with the canards set to δc=-40 deg, δdc=-20 deg at angles of attack 20 deg, 30 deg, and 40 deg respectively. (Note that this is the opposite deflection from that shown in Fig. 17 and therefore the lateral-directional coefficients are expected to reverse in sign.) At 20 deg angle of attack, the unloaded (right) canard is at -40 deg incidence to the freestream, and as such, its vortex is deflected up away from the fuselage as it travels aft. The left canard, on the other hand, is now at 0 deg incidence to the freestream, and its vortex stays down close to the fuselage as it passes aft. As the pair of vortices reaches the vertical tail, the vortex from the left side is in close proximity to the vertical tail while the vortex from the

other side has been deflected away from the vertical tail. The low pressure field of this vortex results in a negative sideforce acting at the vertical tail for a positive change in the yawing moment (and a negative rolling moment). As the angle of attack is increased to 30 deg, the vortex from the right side still passes well above the aft portion of the aircraft, but the vortex originating from the left canard can be seen to actually cross over the fuselage where it is now impinging on the opposite side of the vertical tail. This results in a reversal of the sideforce acting at the vertical tail which accounts for the loss of yawing moment as well as the sign reversal in the rolling moment. Finally, by 40 deg angle of attack, the vortex from the left canard has crossed back to the left side of the vertical tail, restoring the positive yawing moment. As further evidence of the impact of the canard vortex interaction with the vertical tail, it will be shown hereafter that removal of the vertical tail eliminates both the loss of yawing moment and the reversal in the rolling moment for this configuration at 30 deg angle of attack.

In order to put differential canard control power into perspective, its effect is shown along with the incremental yaw control power of both the rudder and thrust vectoring system in Fig. 21. The rudder power was obtained from wind-tunnel tests. The thrust vectoring system provides a propulsive rather than an aerodynamic yawing moment. Therefore, to compare, thrust vectoring control power must be reduced to coefficient form which requires specifying a flight condition. Mach 0.4 at 30,000 ft altitude (full scale) is representative of a typical subsonic flight condition and results in a dynamic pressure of 70.3 psf. At this condition, the engine installed in the X-31 may

produce thrust levels on the order of 5,200 lbs at maximum afterburner. Based on studies of post-exit-vanes similar to those on the X-31[14,15] it seems reasonable to assume an isentropic jet turning angle of around 16 deg with the X-31's maximum vane deflection of 34 deg. With a three-paddle geometry like that of the X-31, the sideforce which can be produced by a single paddle deflected into the exhaust plume is given by

$$Y_{\delta v} = F_T \sin(\delta_j)\cos(30°)\,.$$

The cos(30°) in the above equation is the result of the position of the sideforce generating paddles at 30 deg away from the horizontal plane. The sideforce multiplied by the moment arm gives the estimated yawing moment available. Table 2 shows the center of pressure of the post-exit-vanes to be at FS 480 with the center of gravity at FS 269.2, for a moment arm of roughly 17.6 ft. Making these assumptions results in a yawing moment of 21,850 ft lbs for an effective ΔC_n of 0.06. It should be noted that several simplifying assumptions have been made in order to estimate the yaw control power of thrust vectoring which is included only to provide a basis of comparison to the control powers of the aerodynamic controllers; parameter identification studies conducted in reference 16 suggest that the ΔC_n realized during flight may be lower than this linear approximation. As shown in Fig. 21, the estimated ΔC_n due to thrust vectoring is roughly the same as the peak levels of either rudder or differential canard for this condition. Below 30 deg angle of attack, the rudder is very nearly as powerful as the thrust vectoring system, and the differential canards are as powerful as the thrust vectoring above 50 deg angle of attack. Even in the range between 30 deg and 50 deg angle of attack where neither the rudder nor the differential canard have as much control power as the thrust

vectoring paddles, the sum of the control power from the two aerodynamic surfaces is roughly equivalent to the propulsive yaw control authority.

In order to be effective as a yaw controller, the differential canard would have to remain effective over a reasonable range of sideslip. The increment in the lateral-directional aerodynamic coefficients due to 20 deg differential canard deflection over a range of sideslip from -30 to 30 deg is shown in Fig. 22. This figure shows that the effect of sideslip on the yawing moment produced by differential canard deflection is highly dependent on the angle of attack. At the two extreme angles of attack shown in Fig. 22, 24 deg and 50 deg, this differential canard deflection is more powerful in producing negative yaw at negative sideslip angles than at positive sideslip angles. This may be beneficial for the use of differential canard for artificial directional stabilization because the differential canards have a stronger stabilizing control power than destabilizing power for these angles of attack. In contrast, the differential canard yaw control power which was minimal at 32 deg angle of attack with 0 deg sideslip can be seen to decrease with small negative angles of sideslip, and although it does increase with positive sideslip, the benefit of this increase is questionable. Finally, the curve at 40 deg angle of attack demonstrates a loss of yaw control power for small sideslip in either direction. It should be noted that the differential canard deflection remains at least somewhat effective at producing yawing moment out to -30 deg of sideslip.

The same combination of controls was tested in the 30- by 60-Foot Tunnel, with the vertical tail removed and only the lowest 20% (the portion encompassing the spin chute compartment) intact. In this test the left canard was deflected trailing edge down and the right canard trailing edge up so that the yawing moment produced would be positive.

As can be seen in Fig. 23, the yawing and pitching moments generated by these controls in the low and high angle of attack ranges are very similar to those seen with the vertical tail on, although the opposite differential canard deflection causes the ΔC_n to be opposite in sign. It is in the angle of attack range from 20 deg to 40 deg that a difference can be seen in the yawing moment. While there still exists a local minimum of ΔC_n through this range, the effect is hardly as prevalent as it was with the tail on. In this case the ΔC_n only drops to 0.030 at 34 deg angle of attack, although the control power does appear to be saturated with -20 deg differential deflection in this range.

The trace of ΔC_l in Fig. 23 also shows distinct differences from the case with the tail on. The rolling moment in the low angle of attack range is now insignificant, and while ΔC_l still increases into the mid angle of attack range to reach a peak of 0.013 at 32 deg angle of attack, the reversal in roll direction never occurs as it does with the tail on.

These data indicate that the pinch-point in the yawing moment effectiveness seen in Fig. 17 is due to the low pressure field of the sideforce generating vortex approaching the vertical tail. Further flow visualization was conducted in the 12-Foot Low Speed Tunnel with the 20% tail on the model. Fig. 24 illustrates the behavior of the canard vortices as they continue aft along the tailless fuselage at 30 deg angle of attack. This

time as the angle of attack is increased to 30 deg, the vortex from the left canard can be seen pass directly over the spin chute compartment. Apparently the absence of the vertical tail makes it impossible for the vortex to completely cross over to the other side of the fuselage with this configuration. The result is only a reduction in the total yawing moment rather than total cancellation.

The information presented so far indicates that differential canard has the potential of being used as an effective yaw control. In fact, the yawing moment generated in the high angle of attack range may be roughly equivalent to that generated by the thrust vectoring system which is currently relied on for yaw control in this range where the tail and rudder are naturally ineffective. However, these control deflection combinations would not be representative of the X-31 in normal, low angle of attack, flight where the current control system would command much lower symmetric canard deflection. In order to be effective as a yaw controller, any control scheme would have to be effective in the low angle of attack range. In the event that thrust vectoring were to fail on the full-scale aircraft, it is unlikely that the pilot would be concerned with post-stall maneuverability, at least once the aircraft is stabilized in level flight. Certainly, the priority would be to land the aircraft safely, which would require adequate lateral-directional stability in the low angle of attack range.

The following configuration better represents the X-31 in the low angle of attack range as would be commanded by its current control system:

Symmetric Canard, δc: 0 deg

Leading Edge Flaps: 0/0 (leading edges clean)

Fig. 25 shows the results of testing this configuration with the 100% vertical tail where the canards are deflected to -20 deg δdc. As the figure shows, the yawing moment produced by differential canard deflection around a symmetric 0 deg is minimal throughout the alpha range. Below 20 deg alpha, the maximum ΔC_n of 0.0075 at 8 deg alpha only half of the 0.015 produced by the same differential around -40 deg symmetric canard deflection.

Fig. 26 shows the results for the 20% tail. The ΔC_n curves in Fig. 26 show the low angle of attack behavior is dominated by a dead band, requiring -30 deg differential canard deflection to generate even 0.01 ΔC_n. This renders the differential canard unusable as a yaw controller at this condition and angle of attack.

It is interesting to note that in the region where the yawing moment pinch point occurred for the 100% tail with the high alpha configuration, for this configuration there exists a control reversal of -0.015 ΔC_n at 34 deg angle of attack which is saturated at -20 deg differential deflection. In the angle of attack range from 24 deg to 36 deg, a positive sideforce increment is being produced along with negative yawing moment increment. This could only be the result of a positive net sideforce acting at a center of pressure behind the center of gravity. The corresponding positive rolling moment leads to the

conclusion that the center of pressure of the net sideforce must be above the center of gravity. Finally, because the removal of the vertical tail did not reduce this phenomenon, it can only be concluded that this sideforce does not act upon the vertical tail, but on the aft fuselage.

The loss of ΔC_n with 0 deg symmetric canard setting was examined in more detail in the 12-Foot Low Speed Tunnel where tests were conducted with -20 deg differential canard deflections for three different symmetric canard settings, holding the leading edges constant at their baseline configuration of 40/32 (40 deg inboard, 32 deg outboard leading edge down). The data of Fig. 27 show that the yawing moment produced consistently decreases as the symmetric canard deflection is increased from -40 deg to 0 deg.

These data show that asymmetric canard deflection could be an extremely effective yaw control device in post-stall flight. This has the immediate application of augmenting the thrust vectoring system used in this range. Unfortunately, in the low angle of attack range where the current control system would command less symmetric canard deflection, the yaw control power generated by differential canard deflection would be severely limited. In order to effectively use differential canard deflection as a yaw control device, it might be possible to redesign the flight control system so that the aircraft trims at low angle of attack with larger trailing edge up canard deflections by deflecting the trailing edge flap surfaces to compensate for the pitching moment offset that this would create. This possibility will be discussed later.

Comparison with previous tests[10,11] shows the strong dependence of differential canard control effectiveness on the specific configuration. Fig. 16 shows the ΔC_n due to differential canard deflection for the two configurations tested in reference 11. Whereas each of these previous tests showed a reduction in ΔC_n due to differential canard with increasing angles of attack, tests of the X-31 showed a strong increase in differential canard effectiveness with increasing angle of attack. Furthermore, while each of the previous tests showed a reduction in the yaw control power of the differential canards when the vertical tail was removed, this study showed that at certain angles of attack, the presence of the vertical tail completely eliminates the ΔC_n due to differential canard deflection. These differences can be attributed to the major differences in the configurations tested. First each of the above references studied three-surface planform geometries with close-coupled canards, while the X-31 is a canard-delta combination with much larger separation between the canard and wing and a smaller ratio of canard to wing surface area. Also, each of the configurations tested in the aforementioned references had twin vertical tails. Because all of these studies have shown a strong dependence of differential canard effectiveness on the presence of the vertical tails, the location of the single, centerline vertical tail on the X-31 can be expected to produce a significant effect.

5. Analysis of Performance Limitations

With the control power of differential canard deflection established, these values can be used to estimate the levels of performance that might be achieved and determine whether yaw, roll, or pitch control will saturate first to become the limiting factor for performing coordinated, wind-axis rolls.

5.1 Coordination of Wind-Axis Rolls

Due to its placement, the vertical tail of the X-31, like that of most aircraft, becomes immersed in the low energy wake of the main wing as the angle of attack increases. This not only cancels out the stabilizing contribution of the vertical tail as shown previously in Fig. 7, but also reduces the effectiveness of the rudder as a yaw control. Fig. 28 shows that the yaw control power of the rudder begins to drop by 30 deg alpha, becoming completely negligible by 55 deg alpha. The importance of the loss of rudder power is compounded by the desire to maneuver about the velocity vector at high angles of attack, so that rolls must be performed about the wind-axis rather than the body-axis. This requires increasing levels of yawing moment in an angle-of-attack range where the available yawing moment is decreasing.

To perform a coordinated ($\dot{\beta} = 0$) wind-axes roll, the approximation can be made

$$r = p\tan(\alpha)$$

and

$$\dot{r} = \dot{p}\tan(\alpha)$$

or, neglecting the cross terms,

$$\frac{N}{Iz} = \frac{L}{Ix}\tan(\alpha),$$

and therefore

$$C_n = C_l \frac{Iz}{Ix}\tan(\alpha).$$

Since the ratio Iz/Ix is typically much greater than 1 (roughly 12 for the X-31), and the $\tan(\alpha)$ is greater than 1 above 45 deg, the amount of yawing moment required to perform a wind-axis roll is far greater than the rolling moment. Since the rudder is ineffective in this range, the X-31 achieves these levels of yaw control through thrust vectoring, and the comparatively small required rolling moments can be generated by the ailerons which remain effective at high angles of attack (see Fig. 29).

If the damping terms are neglected in order to assess only the initial response to a control input, the amount of yaw control deflection that will be required to coordinate a wind-axis roll using a given amount of roll control and vice versa can be estimated. The moments generated by 10, 20, and 30 deg of differential canard were computed. The aileron deflection was solved by iteration to produce a wind-axis roll according to the above equation. The resulting deflections in Fig. 30 show that with the addition of the differential canard for yaw control, the roll performance of the X-31 without thrust vectoring will remain limited by yaw control. Relaxing the constraint that sideslip be zero, it is possible to greatly improve the turning performance. As long as sideslip is not allowed to continually build up, a certain amount of sideslip can be used to increase the C_n which could otherwise be produced. The plots in Figs. 31 and 32 show the effect of

carrying -5 and 5 deg of sideslip on the aileron deflection needed to produce a wind-axes turn. These plots show that much greater amounts of aileron deflection are required when the sideslip is allowed to build up to -5 deg, and generally an aileron reversal is required when sideslip reaches 5 deg.

5.2 Inertial Coupling

Another factor which has often limited high-angle-of-attack rolling performance in the past is the amount of available pitch authority. Although an aircraft may have the control authority required to trim at high angles of attack, the additional demand placed on the longitudinal controls by inertial coupling becomes increasingly significant with increasing angle of attack.[17]

The non-linear equation of motion for pitching moment is:

$$I_Y \dot{q} = M + I_{ZX}(r^2 - p^2) + (I_Z - I_X)rp .$$

If roll rate gets high enough, a very significant contribution to pitching moment will result from the last term, i.e., inertial coupling. It is possible that with the advent of the differential canard as a yaw control, yawing moment may not be the limiting factor in a coordinated wind-axis roll at high angles of attack because the higher roll rates which will now be possible may result in saturation of the nose down pitch controls.

Wind-tunnel tests were conducted to determine the maximum amount of aerodynamic pitching moment that can be generated by the X-31. Fig. 33 shows the loci of these extrema as they vary with angle of attack. Note the control surface delcetions, which vary with angle of attack, are not shown. To evaluate the actual pitching moments

reflected by these coefficients, the dynamic pressure will be needed. The control schedule shown in Fig. 34 results in zero pitching moment with lift and drag coefficients shown in Fig. 35. With an unpowered aircraft (such as the X-31 drop model) C_L and C_D alone determine the glidepath angle as

$$\tan(\gamma) = \frac{C_D}{C_L}$$

which can then be used to determine the dynamic pressure necessary to maintain unaccelerated flight

$$D\sin(\gamma) + L\cos(\gamma) = W.$$

Using the $\tan(\gamma)$ relation to eliminate drag and substituting for L

$$L = C_L \bar{q} S,$$

this becomes

$$\bar{q} = \frac{W\cos(\gamma)}{C_L S}.$$

Again, the 550 lb, 27% scale drop model will be used for the following analysis so that the numbers obtained will reflect the performance expected in drop model flight tests discussed later. The dynamic pressure resulting from the control schedule in Fig. 34 for the 27% X-31 drop model is shown in Fig. 36. With the constraint that $r = p\tan(\alpha)$, Fig. 37 shows the maximum amount of coordinated roll rate which can be sustained before saturating the nose-down pitch controls based on this dynamic pressure estimate. This plot shows that as angle of attack increases, the maximum amount of wind-axes roll rate that can be maintained drops, reaching 50 deg per second at 65 deg angle of attack.

In summary, the initial response to a roll command will remain limited by yaw control power with the advent of differential canard controls. The ailerons retain sufficient roll control authority to coordinate the maximum amount of yawing acceleration which can be generated by the differential canards at up to 80 deg angle of attack. The level of roll rate which can be generated and sustained may prove to be limited by the nose-down pitch authority of the aerodynamic controls as inertial coupling at high rates and high angles of attack becomes significant. In fact, this phenomenon was observed during a drop model flight test as will be shown in the following chapter.

6. Drop Model Tests

In order to verify the results from the static and forced-oscillation wind-tunnel data, drop model flight tests were conducted.

The radio-controlled drop model test technique was originally developed to study post-stall aerodynamics and spin-entry. Since its inception, the technique has been broadened to include a wide range of low-speed flight dynamics. Drop model tests are conducted at the Wallops Flight Facility where a specially modified UH-1 helicopter carries the dynamically scaled model to an altitude between 6,000 and 12,000 ft. The model is then released and remotely flown through a predetermined flight plan from a ground station. As illustrated in Figs. 38[18] and 39,[19] flight data is transmitted down from the instruments on the model to the flight control computer on the ground, and an out-of-cockpit view is transmitted down to the pilot from a camera onboard the model. The pilot's commands along with downlinked state feedbacks are interpreted by the flight control computer according to the flight control laws, and the control surface actuator commands are radioed back up to the model.

As the model approaches the ground, the flight is ended when an onboard parachute is deployed on command from the ground station. The model is then retrieved from the water and returned to be reused for the next flight.

The drop model flights for this study were made with the 27% dynamically scaled X-31 model. Dynamic scaling means that a drop model flight from 12,000 ft to sea level simulates a full scale altitude in the range from 35,000 to 26,000 ft. 25 previous flights

have already been conducted with this model, so the two flights which will be used for this research will be referred to as flights 26 and 27. All data shown herein are in drop model scale.

6.1 Drop Model Flight 26: 100% Vertical Tail

During drop model flight 26, coordinated wind-axis rolls at 50 and 60 deg angle of attack were executed with the differential canards as the only active yaw control and the symmetric canards still active for pitch control. Fig. 40 shows the time history of right and left turns which were initiated at 50 deg angle of attack. At 51 seconds into the flight, the pilot applied and held full right roll stick, and the control system responded with full differential canard deflection (-20 deg). The differential canard remained saturated at maximum deflection for approximately one second before sufficient yaw rate developed for the control system to begin reducing differential deflection. The yaw rate overshot the command, reaching almost 90 deg per second within three seconds of the initial control input, and the control system began to correct this by applying about 5 deg of positive differential canard. By 56 seconds, the pilot reversed the stick to stop the roll and received the full 20 deg of canard deflection for one and a half seconds. The differential canard deflection arrested the right yaw and developed a left yaw of -30 deg per second before the pilot released the stick, and the aircraft was allowed to return to level flight. At 58 seconds into the flight, the pilot applied full left stick, and with only brief saturation of the differential canard, the aircraft reached a yaw rate which stabilized around -70 deg per second.

Fig. 41 shows time histories during this maneuver focusing on the yaw axis. From the traces of differential canard and aerodynamic yawing moment coefficient, the actual control power of the differential canard can be observed. During the initial -20 deg deflection of the differential canards at 51 seconds, the yawing moment appeared slow to develop, but by 52 seconds when the deflection had stabilized, the aerodynamic yawing moment, which is assumed to be predominantly due to differential canard, had risen to about 0.03. For -20 deg of differential canard deflection, this represents a control power very similar to that which was seen in the static wind-tunnel tests (see Fig. 17). Between 56 and 57 seconds, 20 deg of differential canard deflection were used to arrest the turn, and while again there appears to have been a lag of about 0.5 second before the aerodynamic forces could completely develop, the yawing moment can be seen to have peaked beyond -0.06. Referring again to Fig. 17, this appears consistent with the levels observed in the static wind-tunnel tests for an angle of attack which had drifted up to around 55 deg. Finally, the maneuver was ended at 63 seconds with -20 deg of differential canard deflection to arrest the left turn, and a corresponding aerodynamic yawing moment of 0.05 can be observed. This is slightly higher than the levels seen in the wind-tunnel.

The traces of yaw rate and sideslip in Fig. 41 show an oscillating body axis rolling behavior, or wing rock, throughout this maneuver. However, the artificial roll damping was able to contain the amplitude of the oscillation so that the sideslip angle never built up past +/-7 deg. This behavior was known to exist for the X-31 from previous studies,[19]

and therefore the differential canard deflection does not appear to have been the driving force behind it.

During this maneuver, the angle of attack drifted away from the initial 50 deg, reaching over 62 deg for a brief period, and Fig. 40 shows that this occurred without any input from the pilot. The time histories in Fig. 42 focus on the pitching behavior during this maneuver. The traces of symmetric canard and flap deflection show that the control system was fighting the pitch up. The differential canard deflection was very small around the time of this pitch up, so it is unlikely that this resulted from the pitching moment due to differential canard (see Fig. 17). Rather, the pitch up can be attributed to the inertial coupling induced by such a high coordinated roll rate. As shown previously in Fig. 37, a loss of pitch control authority was expected at 50 deg angle of attack for body axis roll rates above 70 deg per second, a boundary which was very nearly crossed during this maneuver. The trace of pitching moment due to aerodynamics compared with the pitching moment due to inertial coupling shown in Fig. 42 shows that the pitch axis paths of the control system were very effective at containing the inertial coupling except for the brief period of yaw rate overshoot.

Fig. 43 shows that by 71 seconds into flight 26, the pilot had increased the angle of attack to 60 deg. At this point, the pilot applied full right roll stick and held it, allowing the aircraft to stabilize at 40 deg per second yaw rate. At 76 seconds, the pilot reversed the stick to arrest the motion.

Fig. 44 shows the time histories for the yaw axis during this maneuver. The trace of the aerodynamic yawing moment shows that at 72 seconds, a C_n of 0.04 was being produced. This is rather lower than would have been expected from the wind-tunnel data shown in Fig. 17 for 60 deg angle of attack except that only -12 deg of differential canard deflection were actually realized during this time. The full 20 deg of differential canard were used to arrest the turn at 76 seconds, and the aerodynamic yawing moment of -0.06 is very similar to what the wind-tunnel tests predicted for an angle of attack of roughly 57 deg.

Fig. 45 shows a summary of the yawing moments due to 20 deg of differential canard deflection observed at different angles of attack during drop model flight 26 as compared to wind tunnel data for the same configuration. For the points tested, there is good correlation between drop model flight and wind-tunnel data which validates the results of the wind-tunnel testing.

6.2 Drop Model Flight 27: 20% Vertical Tail

For flight number 27 of the 27% scale X-31 drop model, the vertical tail was removed leaving only the lowest 20%, and the differential canards were used as the only yaw control available. Between the instability of the tailless X-31 (see Fig. 7) and reduction of differential canard control power at low angles of attack (see Fig. 23), it was expected that the model would become increasingly difficult to control as the angle of attack was reduced. Because of this, the flight plan called for the test to begin by

stabilizing at the maximum angle of attack for trim. Then, the pilot slowly reduced the angle of attack, expecting a departure as the instability overcame the available control power. Fig. 46 shows that such a departure had not yet occurred as the model reached 30 deg angle of attack, so at 52 seconds into the flight, the pilot applied full left roll stick and held it for two seconds. The aircraft immediately responded with an uncoordinated, nearly body-axis roll to the left at almost 100 deg per second which allowed the sideslip angle to build up to -20 deg. As the pilot held the control input, the model maintained a severe roll oscillation and pitched up to 50 deg angle of attack where the pilot released the stick and the model was allowed to stabilize.

The trace of aerodynamic yawing moment during this maneuver in Fig. 47 shows that up to the point of the control input, the differential canards were able to contain the sideslip to within a few deg. Specifically, this figure shows the differential canard yawing moment control power to be as high as -0.0013 per deg which compares reasonably well with the wind-tunnel data presented in Fig. 23 for the tailless X-31 at 30 deg angle of attack. When the control input was applied, however, the yawing moment was immediately dominated by the effect of sideslip, and from 52 to 54 seconds, the trace of C_n in Fig. 47 mirrors the trace of sideslip very closely. After 54 seconds, the angle of attack had increased to 50 deg, and the pilot released the controls. At this point, the yawing moment began to follow the differential canard deflection more closely, showing a differential canard control power of -0.0025 per deg at 50 deg angle of attack.

Unexpectedly, this departure was characterized by a pitch-up which allowed the aircraft to restabilize. Fig. 48 shows time histories for this maneuver that focus on the

pitching behavior. Unlike the pitch-up which was witnessed in flight 26 during coordinated wind-axis rolls, inertial coupling was not the driving factor during this departure. Fig. 48 shows that the pitching motion began by 53 seconds into the flight, where inertial coupling creates no appreciable contribution to pitching moment. Instead, this pitch-up can be attributed to aerodynamic effects. The pitching moment due to differential canard deflection during this time can account for over half of the total pitching moment observed (see Fig. 23), and the remainder may be due to other aerodynamic effects such as pitching moment due to sideslip.

With the aircraft stable again, the angle of attack was again reduced to as low as 22 deg. At 64 seconds, as shown in Fig. 49, the pilot again applied full left stick and held it for one and a half seconds. As before, the model responded with a body-axis roll to the left which developed into a high amplitude oscillation. This time, the pilot reversed the stick, giving full right roll input at 65.5 seconds, and held it for almost three seconds. This caused a brief disruption of the roll oscillation after which the aircraft resumed body axis rolling.

The yawing moment trace in Fig. 50 shows very little yaw control power at this angle of attack with 10 deg of differential canard being sustained, however both yaw rate and sideslip were contained up to the point of the control input. At that point, the total C_n was again dominated by the sideslip effect.

The pitching character of this departure (as shown in Fig. 51) was similar to that seen at 30 deg angle of attack. The aerodynamic pitching moment at the beginning of the

maneuver caused the aircraft to pitch up to 40 deg angle of attack before the pilot's control reversal allowed the angle of attack to drop briefly before increasing again.

During both drop model flight tests, the differential canards generated moments very similar to those predicted from wind-tunnel data, and coordinated, wind-axis rolls at 50° and 60° angle of attack were performed for the first time with the unpowered drop model. At 50° alpha, the roll rates developed high enough to be limited by the pitch authority needed to offset the inertial coupling effect demonstrated earlier. The flight control scheme used for the tailless drop model test (which will be described in detail later) was able to maintain steady flight with 20% vertical tail at angles of attack approaching 20°, and departures which ensued from extreme control inputs proved to be mild and easily recoverable.

7. Validation of Flight Simulation

Since only two drop model flights were available to study these controls, the X-31 drop model flight simulator was relied on to develop and evaluate control methods and feedback systems. The effects of vertical tail removal and differential canard deflection were modeled based on the wind-tunnel data. The drop model simulator combines accurate six-degree-of-freedom nonlinear modeling of the aerodynamic results from wind-tunnel and drop-model testing of the X-31 along with duplication of the drop model flight control laws. This simulator is used as part of the drop model program to develop and practice flight profiles for drop model tests.

7.1 Reproduction of Drop Model Flight 26: 100% Vertical Tail

In an attempt to interpret the accuracy of the simulation in predicting flight performance, the conditions of drop model flight 26 were duplicated in the simulation, and similar control inputs were made manually. Fig. 52 shows the time history of full right and left stick inputs in the simulator at 50 deg angle of attack. Comparing this to the actual flight results of Fig. 40 shows reasonably good reproduction of results with certain notable differences. First, the yaw rate responded slightly faster in the simulation, although it did not peak as high as the actual flight test, and the subsequent pitch-up resulting from inertial coupling did not occur. Later, when the stick was reversed, the results matched the drop model flight very closely.

The pitching moment traces in Fig. 53 show that in the simulation, the longitudinal control surfaces lagged the inertial coupling moment slightly, while the significantly lower rolling and yawing moments kept the pitching moment due to inertial coupling within limits that the aerodynamic controls could maintain.

Of greater significance are the yawing moment traces in Fig. 54. The response of yawing moment to the differential canard deflection closely matched that which was seen in flight 26 (see Fig. 41). The failure of the simulation to duplicate the yaw rate overshoot seen in drop model flight 26 does not appear to have been due to any lack of control power in the differential canard model. As the yaw rate to the left more closely matched flight than to the right, it seems plausible that a slight difference may exist between the flow asymmetries of the actual drop model and those of the simulation. Furthermore asymmetric vortex formation is known to be strongly influenced by initial conditions, and additional drop model flights with which to attempt multiple entry conditions were not available to examine this possibility.

The roll command at 60 deg angle of attack was also reproduced in the simulator with good results as shown in Fig. 55. The traces of differential canard and resulting yaw rate show excellent correlation to those of flight 26 shown in Fig. 43, although the oscillatory roll rate which had developed by this point in the drop model flight was not duplicated for the simulation. The yawing moment seen in the drop model flight (Fig. 44) shows that the yawing moment due to differential canard may actually be higher than was modeled in the simulation for 60 deg angle of attack (Fig. 56).

7.2 Reproduction of Drop Model Flight 27: 20% Vertical Tail

The tailless configuration of drop model flight 27 was also reproduced in the simulation. A full left roll stick input was performed at an angle of attack of 30 deg with resulting time histories shown in Figs. 57-59 which are similar to the traces recorded from the drop model flight in Figs. 46-48. As in actual drop model flight, the simulation showed that an uncoordinated roll rate resulted in a build-up of sideslip and then developed into a high-amplitude roll rate oscillation. As in the drop model test, a pitch-up developed which peaked above 50 deg angle of attack before the motion was allowed to stabilize when the stick was released.

These time histories show that the drop model simulation as it has been modified to include the effect of reduced vertical tail and differential canard deflection is at least reasonably good at producing results similar to what would be seen in an actual drop model flight test. Furthermore, where discrepancies exist in control power or stability between the drop model and the simulation, the simulation seems to err on the conservative side. Therefore actual flight would be expected to perform at least no worse and perhaps better than the simulation. With confidence based on this comparison, the extrapolation will be made that the simulation will be an accurate model for the tailless X-31 with differential canards so that the control laws can be modified in the hope that in the following chapter controlled flight can be demonstrated at lower angles of attack.

8. Stability Augmentation

An extremely simplified version of the flight control system used on the 27% X-31 drop model is shown in Fig. 60 where the variables in these diagrams are defined in Tables 4-7. In this simplified diagram, all flight control options which were not used during the course of this research have been omitted, and in some cases, multiple in-line gains have been combined into a single block. The two switches which remain in this simplified control system are SWrud which activates the rudder if set to 1 and SWdcd which activates the differential canard deflection if set to 1. For brevity, the conditioning which has been applied to the downlink parameters (such as alpha, beta, etc.) as well as that which has taken place on the pilots inputs is not shown. Certain values (such as qbar and mic) represent calculations based on the downlink data which are also omitted. The gains in these diagrams were modified for different situations, and the particular combinations which apply to each case are detailed in Tables 5-7.

8.1 Stabilization of Linear System Poles

The unstable open loop poles for the 27% X-31 drop model in gliding flight at 20 deg angle of attack developed previously are shown in Fig. 61 along with the zeros associated with a yaw rate to rudder feedback loop. The open loop response to an aileron impulse shown in Fig. 62 illustrates the divergent oscillation indicated by the unstable complex pair of poles. The flight control system as it was implemented on the X-31 drop model during flight 26 used roll rate to aileron feedback with 0.052 gain, sideslip to

rudder feedback with -0.03 gain, and yaw rate feedback to rudder with 0.156 gain to stabilize the system under these conditions. Applying these gains to the decoupled, linearized equations of motion results in the following closed loop poles:

$$-0.0636 \pm 1.1683i,$$

-0.4762, and

-0.0055

as shown in Fig. 63, again along with the zeros associated with the yaw rate to rudder feedback loop. As shown in Fig. 64, the response to an aileron impulse remains oscillatory, although the response is now lightly damped rather than divergent.

The effect of removing the vertical tail on the open loop poles is shown in Fig. 65 where the open loop poles are shown. Since the rudder has been removed along with the vertical tail, the zeros shown in this plot are those representing yaw rate feedback to the differential canard. As is evident in the open loop poles, the removal of the vertical tail reduced the natural frequency of the oscillatory mode at the same time as the damping ratio was further destabilized. The open loop response to an aileron impulse shown in Fig. 66 illustrates this behavior. Feedback gains to stabilize this system were developed iteratively using a successive loop closure technique. By closing sideslip to aileron and differential canard along with roll rate to aileron and yaw rate to differential canard feedback loops, it was seen that the X-31 with 20% vertical tail could be stabilized at 20 deg angle of attack. The gains developed with this linear model were refined in the non-linear simulation to better optimize the results. Closing the feedback loops with the final gains of 0.2 for roll rate to aileron, 0.5 for sideslip to aileron, 5.0 for yaw rate to

differential canard, and -4.0 for sideslip to differential canard produced the following augmented poles for the linear system:

$$-0.2788 \pm 0.8232i,$$

-0.7062, and

-0.0693

which are shown in Fig. 67. As shown by the plot of the closed loop response to an aileron impulse in Fig. 68, this combination of feedback gains increased the natural frequency of the dominant oscillatory mode and resulted in a favorable damping ratio.

8.2 Modification to Longitudinal Control Laws

Unfortunately, as previously mentioned, the reduction of symmetric canard deflection at lower angles of attack will degrade the yawing moment available from the differential canard deflection. Therefore the longitudinal portion of the flight control system was modified slightly to cause the aircraft to trim with a greater negative canard deflection. The longitudinal control law block diagram in Fig. 60a shows that a constant offset "dfoff" is subtracted from the symmetric trailing edge flap command. By varying this offset, it is possible to alter the combination of symmetric canard and trailing edge flap deflections for trim. Figs. 69 and 70 show the symmetric canard and flap deflections observed in the non-linear simulation when trimmed over a range of angle of attack as a function of the longitudinal control law parameter "dfoff." To maximize the control effectiveness of the differential canard, a "dfoff" setting of 25 was used in subsequent simulation tests.

8.3 Evaluation in Nonlinear Simulation

Certain assumptions were made in order to develop the decoupled, linearized equations of motion used for the linear stability analysis. For example, it was assumed that all of the aerodynamic coefficients obtained from the wind-tunnel studies would truly be linear within the range of the perturbations used to develop the derivatives. Even if that could be guaranteed, it should be noted that the linear analysis is only valid within the range of those perturbations. Once an excursion is made beyond those levels, nonlinearities which are known to exist will make conclusions based on the linear simulations invalid. Furthermore, unlike the linear equations, the actual control surfaces have deflection and rate limits beyond which additional control power is simply not available, and this further limits the range of perturbations over which the linear analysis is accurate. For these reasons, the six-degree-of-freedom, nonlinear simulation which included actuator models was used to verify and refine the gains obtained from the linear analysis.

The final gain schedules developed from the nonlinear simulation are shown in Tables 5 and 7, and Figs. 71-73 show time histories from the simulation with these gains at 30 deg, 25 deg, and 20 deg angle of attack. These figures show that these feedback gains were able to contain sideslip excursions to within 3 deg; however, the turning performance remained very slow. The maximum yaw rate which was demonstrated in these simulations while maintaining stability was only 3 deg per second. These time histories show the strong correlation between sideslip and lateral stick input. With this

being the case, extreme roll stick deflections (like those tested on the drop model flights) result in sideslip levels which saturate the differential canard control power, and an unstable divergence ensues. Below 20 deg angle of attack, even these extremely high gains proved insufficient to maintain lateral-directional stability, and severe yaw oscillations developed into directional departures in all cases tested. Therefore, for the remainder of this study, only angles of attack of 20 deg or greater will be considered.

8.4 Landing Analysis

It is questionable whether a survivable landing of the tailless X-31 configuration can be performed at 20 deg angles of attack. Therefore, some landing performance estimates will be shown for this flight condition. The unpowered glideslope, as shown previously, is governed by the equation:

$$\tan(\gamma) = \frac{C_D}{C_L},$$

and the dynamic pressure for unaccelerated flight was shown to be:

$$\bar{q} = \frac{W\cos(\gamma)}{C_L S}.$$

With the increase in the control law parameter "dfoff" necessary to maintain yaw control power on the differential canards, the unpowered simulation was observed to trim at 20 deg angle of attack with $C_L = 0.764$ and $C_D = 0.191$ for a glideslope of γ=14 deg. Applying these coefficients to the full-scale aircraft on approach, assuming standard sea level density, this equates to a dynamic pressure of 68.3 psf (full scale) for a velocity of 240 ft/sec and a sink rate of 58.0 ft/sec. This glideslope is considerably steeper than

anything normally performed by this type of aircraft on approach, but a flare analysis will be conducted to determine the possibilty of such an unorthodox maneuver.

Assuming a pitch-up to 30 deg angle of attack to flare for touchdown, the unaccelerated flight constraint can be temporarily relieved resulting in the following equations for the rate of change of total velocity, $\dot{V}_T$, and sink rate, $\dot{V}_D$,

$$\dot{V}_T = g\sin(\gamma) - \frac{\rho S V_T^2 C_D}{2m} \text{ and}$$

$$\dot{V}_D = g - \frac{\rho S V_T^2 \left[C_L \cos(\gamma) + C_D \sin(\gamma)\right]}{2m}.$$

Starting with the above conditions, $C_L = 1.12$, and $C_D = 0.50$ at 30 deg angle of attack, Fig. 74 shows the resulting velocities for the full-scale aircraft as a function of time. This figure shows that if the pilot has timed his flare perfectly, the minimum descent rate he could possibly achieve with this scenario is 27.3 ft/sec with a touchdown airspeed of 195 ft/sec.

With power on, the trim flight conditions are more complicated:

$$W = F_T \sin(\alpha - \gamma) + D\sin(\gamma) + L\cos(\gamma), \text{ and}$$

$$D\cos(\gamma) = L\sin(\gamma) + F_T \cos(\alpha - \gamma).$$

Solving the second equation for F_T and substituting:

$$W = D\left[\sin(\gamma) + \cos(\gamma)\tan(\alpha - \gamma)\right] + L\left[\cos(\gamma) + \sin(\gamma)\tan(\alpha - \gamma)\right], \text{ or}$$

$$W = \bar{q}S\left\{C_D\left[\sin(\gamma) + \cos(\gamma)\tan(\alpha - \gamma)\right] + C_L\left[\cos(\gamma) + \sin(\gamma)\tan(\alpha - \gamma)\right]\right\}$$

for a dynamic pressure of:

$$\bar{q} = \frac{W}{S\left\{C_D\left[\sin(\gamma)+\cos(\gamma)\tan(\alpha-\gamma)\right]+C_L\left[\cos(\gamma)+\sin(\gamma)\tan(\alpha-\gamma)\right]\right\}}$$

For trimmed flight of the full-scale X-31 with a glideslope of γ=4 deg, this results in a dynamic pressure of 63.6 psf or an approach velocity of 231 ft/sec and a sink rate of 16.1 ft/sec.

Assuming the steepest safe landing can be performed with a glideslope of up to γ=4 deg with an airspeed of 170 kts and no flare results in a maximum sink rate of 20.0 ft/sec. With this criteria, it has been shown that a safe landing can be achieved with a powered approach at 20 deg angle of attack. However, in an engine out condition the minimum touchdown sink rate exceeds these limits by at least one third.

9. Conclusions

The purpose of this report was to investigate the possibility of using differential deflection of the canard surfaces on the X-31 to supplement the available yaw control authority. Furthermore, the possibility of using the yaw control power of the differential canard to control the X-31 with a reduced vertical tail was examined.

The height of the vertical tail on the X-31 has a linear relationship with directional static stability only at 0 degrees angle of attack where removal of the vertical tail reduced static directional stability from 0.002 to -0.004 per degree. Between 20 and 30 degrees angle of attack, the portion of the vertical tail from 20% up to and including 60% actually exhibited a destabilizing effect. Above 50 degrees angle of attack, no part of the vertical tail made any significant contribution to the static stability of the aircraft.

Differential deflection of the canard surfaces was shown to produce significant levels of yawing moment on the X-31 configuration, particularly at angles of attack above 40 degrees. Although thrust vectoring provides superior levels of yawing moment below 40 degrees angle of attack, the addition of differential canard deflection could effectively provide augmentation or redundancy in yaw controls for this configuration throughout the angle-of-attack range. In fact, it was shown that the combination of both rudder and differential canard deflections may provide yaw control power with levels similar to those available through thrust vectoring over the entire angle-of-attack range from 0 deg to 80 deg. If used in conjunction with the existing thrust vectoring on the X-31, differential canard may be able to double the available yawing moment at high angles of attack.

Alternately, differential canard could be combined with thrust vectoring or rudder deflections to generate direct sideforce, and each of these benefits could be achieved without any physical modifications to the airframe.

It was determined that with the addition of differential canard as a yaw controller, the lateral control power is high enough that the initial response to a coordinated wind-axis roll command would remain limited by yaw control authority. However, it was shown that the maximum wind-axis roll rates which can be sustained will be limited by the pitch authority required to compensate for inertial coupling in some cases.

Drop model flight tests correlated with the yaw control power of the differential canards evidenced in the wind-tunnel tests. During drop model flights, coordinated, wind-axis rolls were performed at 50 deg angle of attack with wind-axis roll rates up to 100 deg/sec (27% model scale), and as predicted, the inertial coupling reached the limit of the pitch control authority. The behavior of the tailless X-31 was also investigated in a drop model flight. During that flight, it was demonstrated that differential canard was able to maintain level flight. However, with the flight control laws implemented for that flight, controllability was not demonstrated and departures characterized by body-axis rolling and a pitch up were observed.

Simulation studies were conducted which correlated with the drop model flights to validate the six-degree-of-freedom, nonlinear simulation of the X-31 drop model. Control laws based on the decoupled, linear equations were then developed and tested in the non-linear simulation. While the removal of the vertical tail greatly increased the available yawing moment around the stall point, the reduction in differential canard

control power for this configuration at lower angles of attack was shown to be the limiting factor for controlled flight without the use of thrust vectoring on the tailless X-31. Even so, controlled flight was demonstrated in the simulator at angles of attack as low as 20 degrees, and it was shown that a safe landing can be achieved without the use of thrust vectoring as long as the engine is still running.

10. Recommendations for Further Study

Differential canard deflection may be useful as either a yawing moment or direct sideforce generator on future aircraft designs. However, due to the variation in results obtained on different configurations, there is obviously a need for more thorough testing of the effect of each feature of a configuration on differential canard effectiveness.

A detailed pressure survey over the canards and along the fuselage around the location of the canards could be performed to determine exactly where along the fuselage the pressure differential generated by the canards acts. This information might lead to canard designs and placements to optimize the yawing moment due to differential deflection.

A pressure survey at the location of the vertical tail surface for both single and twin tailed configurations might create a better understanding of the influence of differential canards on the vertical tails and rudders.

References

1. Lennox, D.; Rees, A.; ed.: Jane's Air-Launched Weapons. Jane's Information Group, 1990.
2. Nguyen, L. T.; and Gilbert, W. P.: Impact of Emerging Technologies on Future Combat Aircraft Agility. AIAA-90-1304, May 1990.
3. Costes, P.: Investigation of Thrust Vectoring and Post-Stall Capability in Air Combat. AIAA-88-4160-CP. 1988.
4. Cobleigh, B. R.: High-Angle-of-Attack Yawing Moment Asymmetry of the X-31 Aircraft from Flight Test. NASA CR 186030. Sept. 1994.
5. Greer, H. D.: Summary of Directional Divergence Characteristics of Several High Performance Aircraft Configurations. NASA TN D-6993. Nov. 1972.
6. La Froth, R. E.: Thrust Vectoring to Eliminate the Vertical Stabilizer. M. S. Thesis, Air Force Institute of Technology. Dec. 1979.
7. Lok, J. J.: Stealth-Modified F-16s in Service. Jane's Defence Weekly, vol. 13, no. 4. Jan. 27, 1990.
8. Hahne, D. E.: Wind-Tunnel Investigation of Three Potential Forebody Vortex Control Devices. NASA TM 4681. Sept. 1995.
9. Hynes, S.: The X-31 Quasi-Tailless Flight Experiment. Oral Presentation to the AGILE Research Group. Jan. 1995.
10. Agnew, J. W.; and Hess, J. R.: Benefits of Aerodynamic Interaction to the Three Surface Configuration. AIAA-79-1830. Aug. 1979.

11. Croom, M. A.; Grafton, S. B.; and Nguyen, L. T.: High Angle-of-Attack Characteristics of Three-Surface Fighter Aircraft. AIAA-82-0245, Jan. 1982.

12. Etkin, B.: Dynamics of Atmospheric Flight. 1972.

13. Weissman, R.: Status and Design Criteria for Predicting Departure Characteristics and Spin Susceptibility. AIAA-74-791, Aug. 1974.

14. Georg, Hans-Ulrich: Enhanced Fighter Maneuverability Description and Preliminary Results of the Full-Scale EFM Thrust Vectoring Ground Tests. Aug. 1987.

15. Tamrat, B. F.; and Antani, D. L.: Static Test Results of an Externally Mounted Thrust Vectoring Vane Concept. AIAA-88-3221. July 1988.

16. Plaetschke, E.; and Weib, S.: Identification of Thrust Vector Effectiveness from X-31A Flight Test Data. Z. Flugwiss. Weltraumforsch. 17. 1993.

17. Nguyen, L. T.; et al: Simulator Study of Stall/Post-Stall Characteristics of a Fighter Airplane with Relaxed Longitudinal Static Stability. NASA TP 1538. Dec. 1979.

18. Croom, M. A.; et al: Dynamic Model Testing of the X-31 Configuration for High-Angle-of-Attack Flight Dynamics Research. AIAA 93-3674 CP. Aug. 1993.

19. Villeta, J. R.: Lateral-Directional Static and Dynamic Stability Analysis at High Angles of Attack for the X-31 Configuration. M. S. Thesis, George Washington University. Aug. 1992.

Table 1: Basic Characteristics of the X-31 as Tested for Static Models

	Full Scale	27%	19%	13.3%
Center of Gravity:				
FS (inches)	269.2	72.7	51.0	35.8
BL (inches)	0.0	0.0	0.0	0.0
WL (inches)	-2.0	-0.54	-0.38	-0.267
Wing:				
Span (ft)	22.83	6.16	4.34	3.04
Mean Aerodynamic Chord (ft)	12.35	3.33	2.35	1.65
Reference Area (sq.ft)	226.30	16.5	8.17	4.02
Vertical Tail:				
Height (ft)	6.81	1.84	1.29	0.908
Reference Area (sq.ft)	37.55	2.74	1.35	0.668
Fuselage:				
Length (ft)	43.33	11.7	8.23	5.78
Canard:				
Span (ft)	8.64	2.33	1.64	1.15
Reference Area, Total (sq.ft)	23.6	1.72	0.852	0.420

Table 2: Basic Characteristics of the X-31 as Tested for Dynamic Vehicles

	(Full Scale)	(27% Drop Model)
Weight (lb)	14500	550
Center of Gravity:		
FS (inches)	269.2	72.2
BL (inches)	0.0	0.0
WL (inches)	-2.0	-0.54
Moments of Inertia:		
Ix (slug sq.ft)	3090	9.16
Iy (slug sq.ft)	34300	122
Iz (slug sq.ft)	35200	126
Ixz (slug sq.ft)	-145	-0.39
Wing:		
Span (ft)	22.83	6.16
Mean Aerodynamic Chord (ft)	12.35	3.33
Reference Area (sq.ft)	226.30	16.5
Aspect Ratio	2.30	2.3
Sweep, Inboard (deg)	57	57
Sweep, Outboard (deg)	45	45
Vertical Tail:		
Height (ft)	6.81	1.84
Reference Area (sq.ft)	37.55	2.74
Aspect Ratio	1.24	1.24
Sweep (deg)	50	50
Aerodynamic Center:		
FS (inches)	422	114
WL (inches)	70	18.9
Volume Coefficient	0.0925	0.0925
Fuselage:		
Length (ft)	43.33	11.7
Canard:		
Span (ft)	8.64	2.33
Reference Area, Total (sq.ft)	23.6	1.72
Aspect Ratio	3.18	3.18
Sweep (deg)	45	45
Aerodynamic Center:		
FS (inches)	77	20.8
WL (inches)	0.00	0.00
Post-Exit Thrust Vectoring Vanes:		
Center of Pressure:		
FS (inches)	480	130

Table 3: Dynamic Scale Factors

Dimensional Quantity	Scale Factor (Scaled/Full Scale)
Angle	1
Angular Rate	$\frac{1}{\sqrt{N}}$
Density (of the air)	σ
Length	N
Moment of Inertia	$\frac{N^5}{\sigma}$
Time	$\sqrt{N}$
Velocity	$\sqrt{N}$
Weight	$\frac{N^3}{\sigma}$

Table 4: Definition of Control Law Parameters

(see Fig. 60)

Table 4.a: Inputs

aoafb	Angle of attack, corrected and filtered, in degrees
aoalu	Angle of attack, limited between 0 and 80 degrees
betcor	Sideslip angle, corrected and filtered, in degrees
mic	Pitching moment due to inertial coupling, calculated from psel and rsel
psel	Roll rate, corrected and filtered, in degrees per second
pstkt	Pilot pitch stick plus trim
pys	Pilot yaw stick (rudder pedal)
qbar	Dynamic pressure, calculated in pounds per square foot
qsel	Pitch rate, corrected and filtered, in degrees per second
rsel	Yaw rate, corrected and filtered, in degrees per second
rsprt	Pilot roll stick plus trim

Table 4.b: Uplink Commands

LCANARD	Left (port) canard command, in degrees
LFLAP	Left (port) trailing edge flap command, in degrees
RCANARD	Right (starboard) canard command, in degrees
RFLAP	Right (starboard) trailing edge flap command, in degrees
RUDDER	Rudder command, in degrees

Table 4.c: Intermediate Parameters

dacom	Differential trailing edge (aileron) deflection command, in degrees
dccom	Symmetric canard deflection command, in degrees
dcdcom	Differential canard deflection command, in degrees
dfcom	Symmetric trailing edge (flap) deflection command, in degrees
drcom	Rudder deflection command, in degrees
pcl	Roll stick cross command to directional path

Table 5: Control Law Functions and Gains Scheduled with Angle of Attack

(see Fig. 60)

Table 5.a: Constant Gains

alpha	faoaaoa	sqdicaoa	sstkaoa	spcomaoa
0	-1.4	1.5	35	6
10	3.5	1.5	34	15
20	6.6	1.5	33	15
25	11.4	1.5	32.5	15
30	18	1.75	32	15
35	23.2	2.25	31.5	10
40	30	2.25	31	7
45	37	2.25	30.5	5
50	46	2.25	30	3
60	54	3	29	2
70	58	3	28	2
80	58	3	28	2

Table 5.b Gains Used on Drop Model Flight 26

Drop 26					
alpha	spaaoa	sbaaoa	ssriaoa	srraoa	sbraoa
0	0.05	0	-0.55	0.052	0
10	0.05	0	1.05	0.104	0
20	0.052	0	1.74	0.156	-0.03
25	0.065	0	2.11	0.208	-0.045
30	0.1	0	2.29	0.26	-0.06
35	0.39	0	2.43	0.65	-0.12
40	0.52	0	2.36	1.04	-0.18
45	0.364	0	5.83	0.728	-0.5
50	0.208	0	16.8	0.416	-1
60	0.104	0	10.1	0.364	-1
70	0.104	0	7	0.39	-1
80	0.104	0	7	0.39	-1

Table 5.c: Gains Used on Drop Model Flight 27

Drop 27					
alpha	spaaoa	sbaaoa	ssriaoa	srraoa	sbraoa
0	0.05	1	-0.55	0.052	10
10	0.05	1	1.05	0.104	10
20	0.052	0.5	1.74	0.156	6.2
25	0.065	0	2.11	0.208	4.9
30	0.1	-2	2.29	0.26	3
35	0.39	-2.8	2.43	0.65	2.5
40	0.52	0.25	2.36	1.04	2.5
45	0.364	0.5	5.83	0.728	2.5
50	0.208	1	16.8	0.416	2.5
60	0.104	1	10.1	0.364	2.5
70	0.104	1	7	0.39	2.5
80	0.104	1	7	0.39	2.5

Table 5.d: Final Gains Developed for Tailless Simulation

Tailless Simulation					
alpha	spaaoa	sbaaoa	ssriaoa	srraoa	sbraoa
0	0.2	0.5	4	5	-4
10	0.2	0.5	4	5	-4
20	0.2	0.5	4	5	-4
25	0.5	0.5	4	5	-4
30	0.5	0.5	4	5	-2
35	0.39	0.2	3	2	-0.5
40	0.52	0	2.36	1.04	-0.18
45	0.364	0	5.83	0.728	-0.5
50	0.208	0	16.8	0.416	-1
60	0.104	0	10.1	0.364	-1
70	0.104	0	7	0.39	-1
80	0.104	0	7	0.39	-1

Table 6: Control Law Gains Scheduled with Dynamic Pressure

(see Fig. 60)

Table 6.a: Schedule 1

qbar	saoaqbar	sqqbar	sqdicqbar
50	1	1.5	0.02
100	0.5	1	0.01
250	0.25	0.5	0.004
1000	0	0	0.001

Table 6.b: Schedule 2

qbar	spcomqbar	spaqbar
0	1	1
30	1	1
45	1	1
60	0.7	0.5
100	0.3	0.1
1000	0.1	0.1

Table 7: Other Control Law Gains and Limits

(see Fig. 60)

Table 7.a: Constant Gains and Limits

aoaauth	100
qauth	10
qdicauth	10
dcscale	1.5
dfscale	1
pstkauth	100
rstkauth	100
paauth	30
baauth	20
pedauth	30
sriauth	30
gdcd	1
rrauth	30
brauth	10
aillim	30
flaplim	30
rudlim	30
dcdlim	20

Table 7.b: Gains Changed for Tailless Simulation

	Drop Model	Tailless Simulation
dfoff	15	25

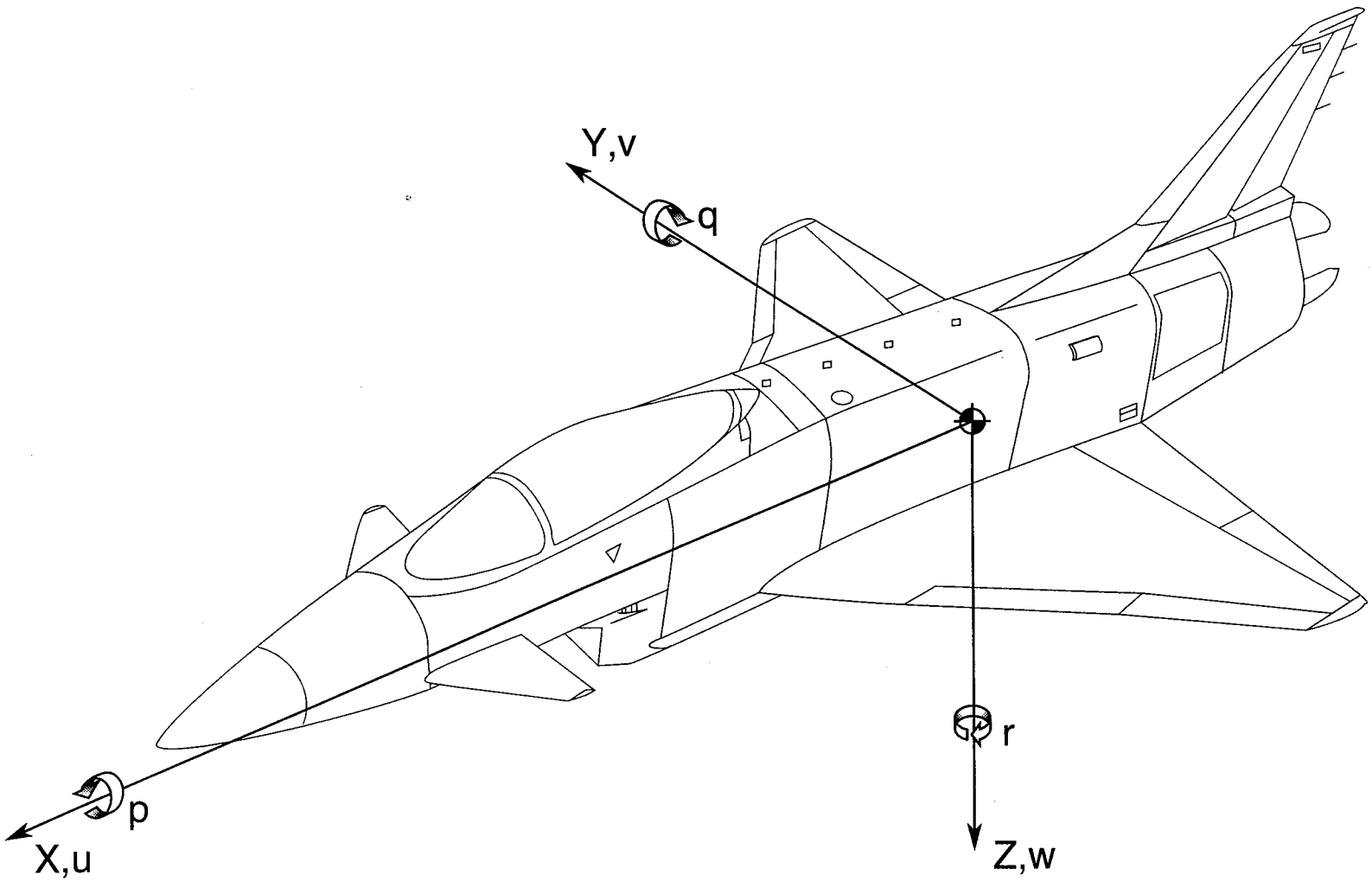

Fig. 1 Wind and Angular Velocity Conventions

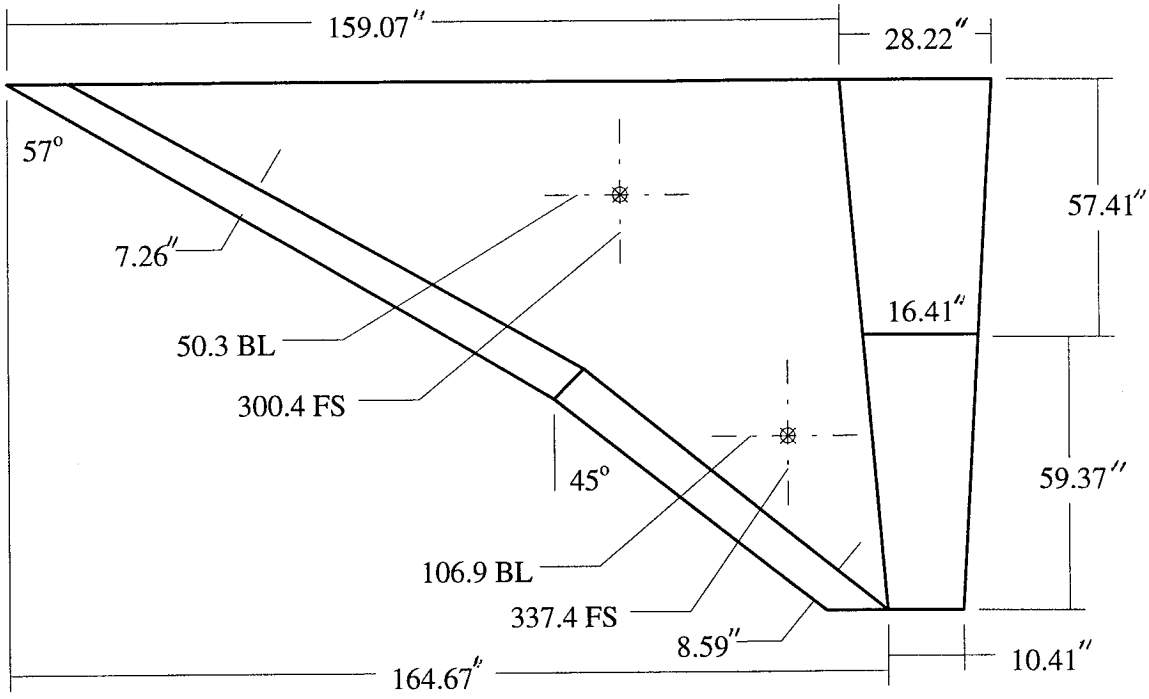

Fig. 2 Wing Geometry

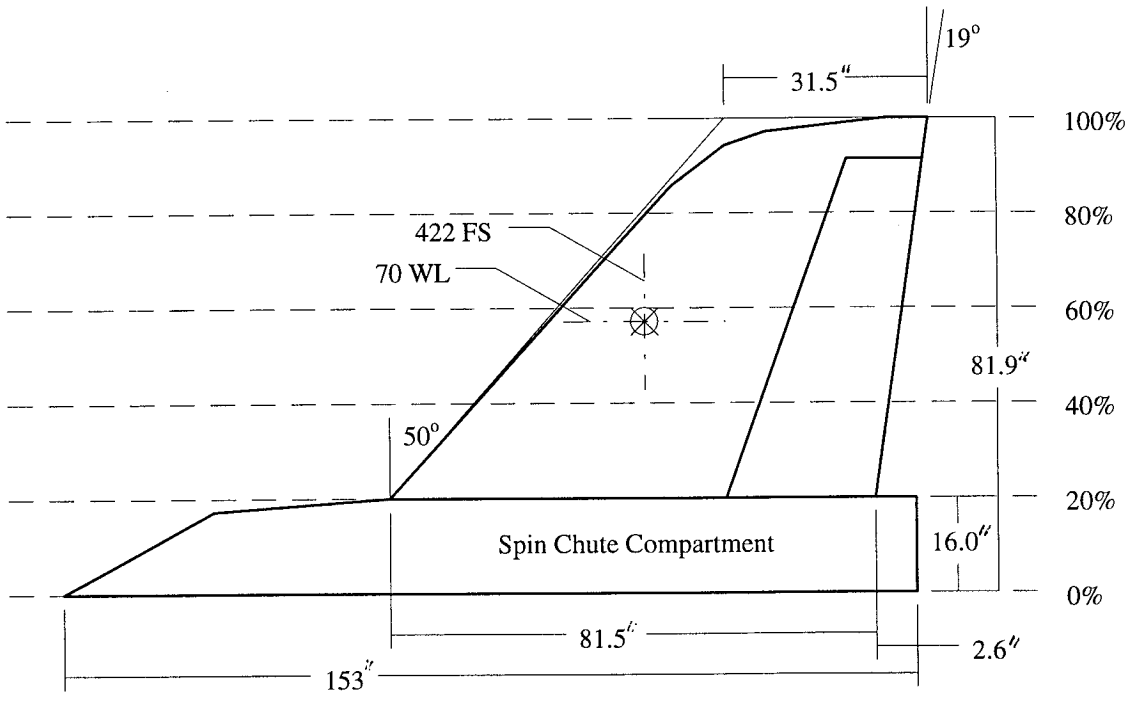

Fig. 3 Vertical Tail Geometry

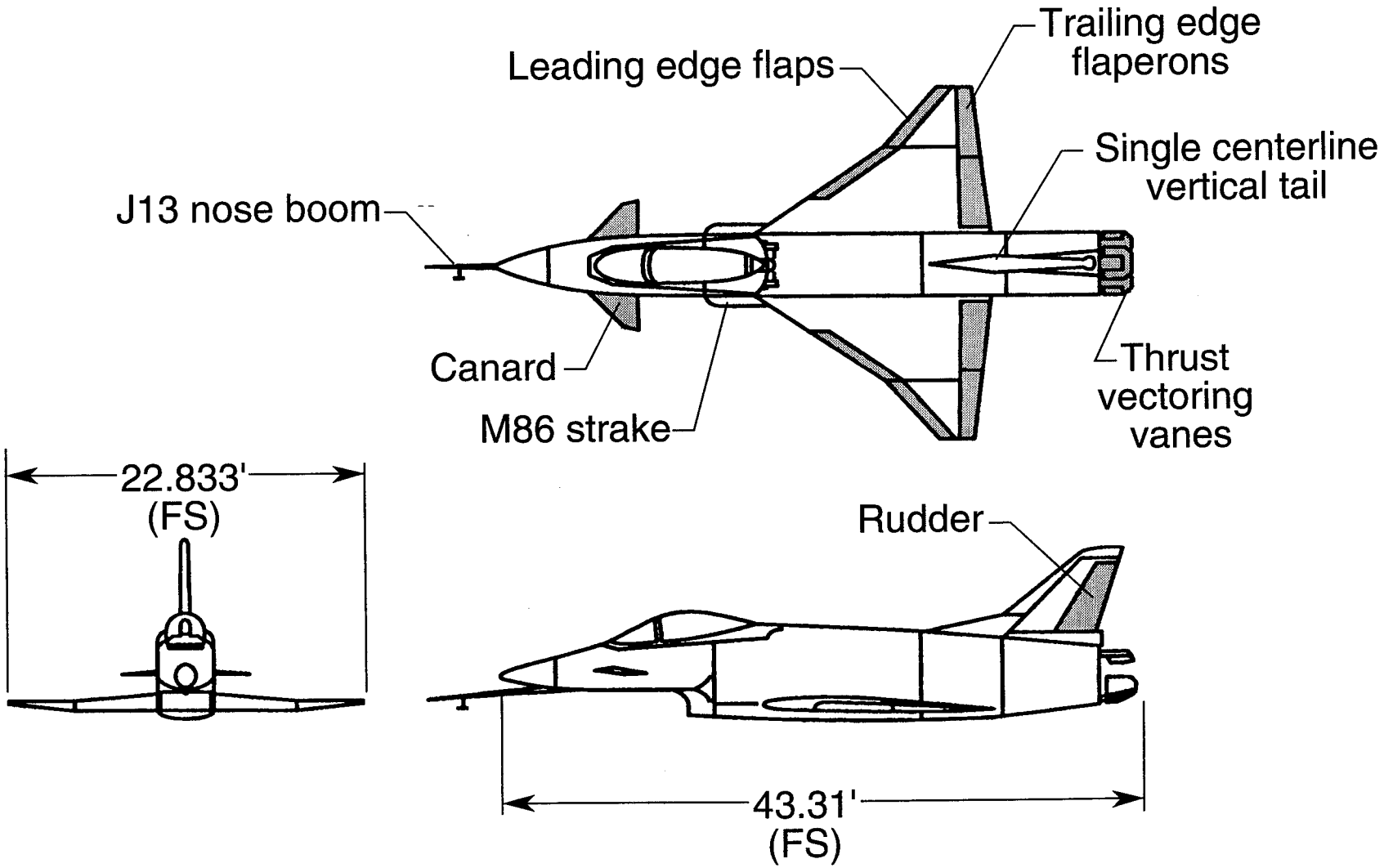

Fig. 4 Three-View of the X-31

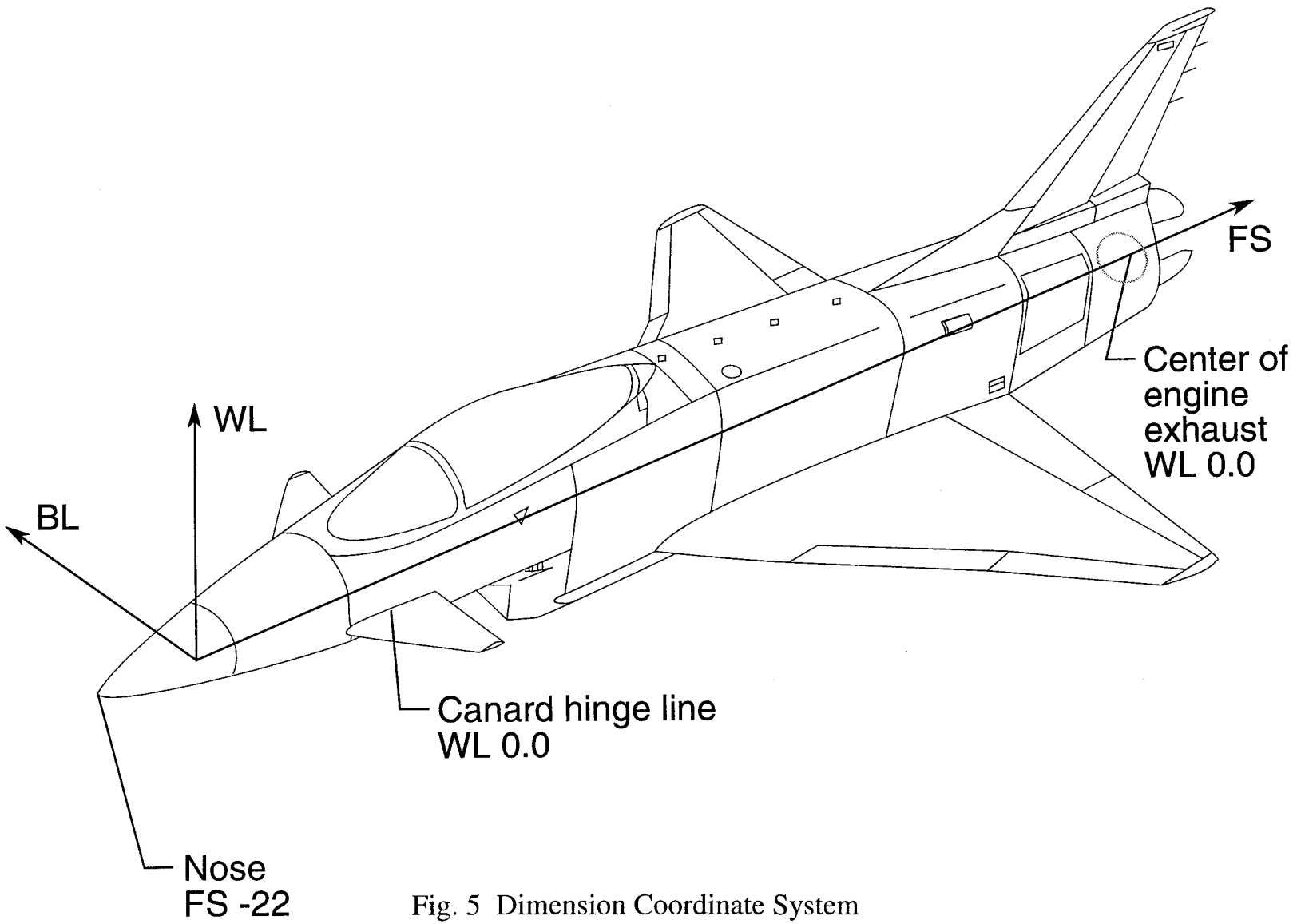

Fig. 5 Dimension Coordinate System

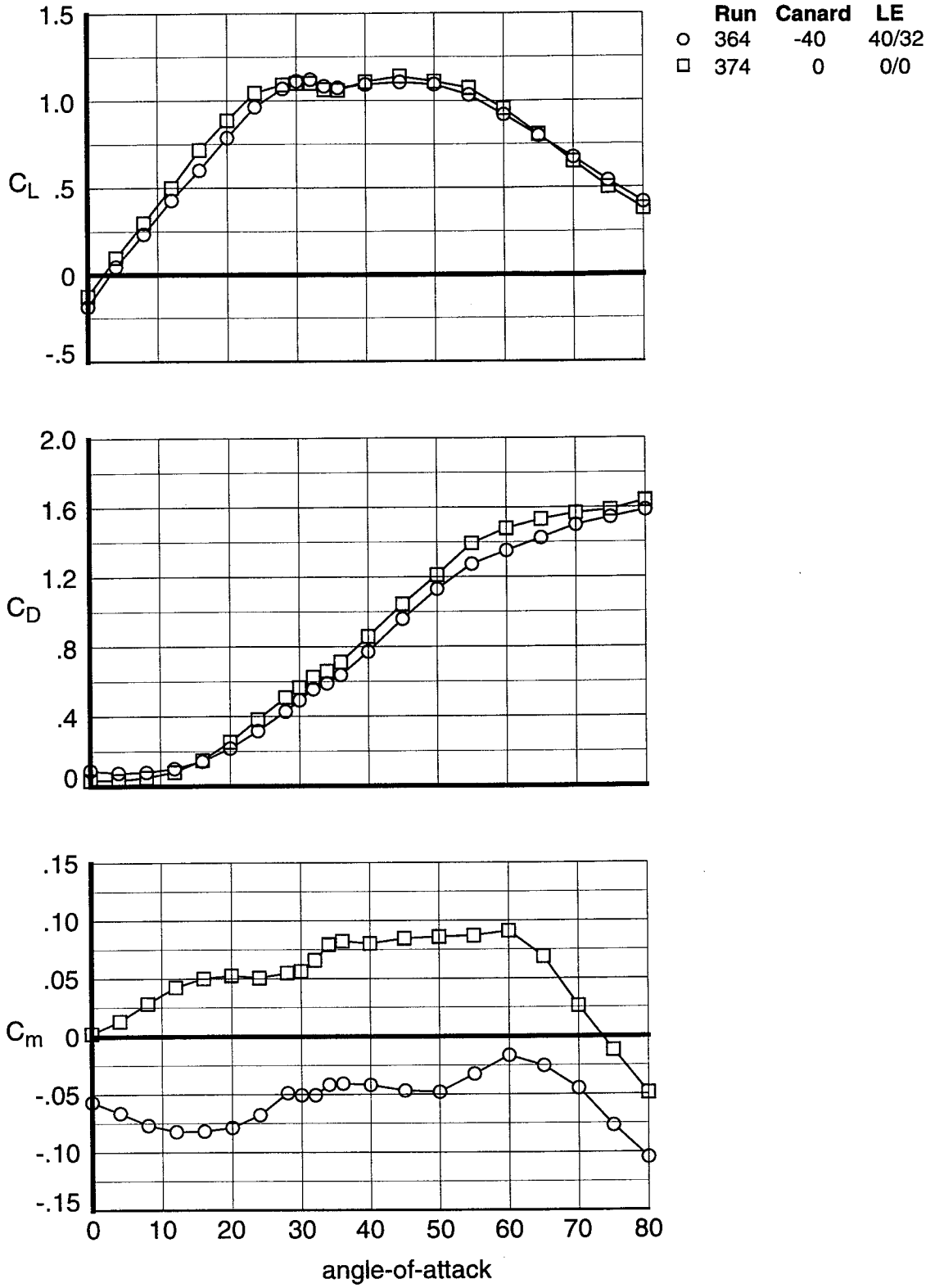

Fig. 6 Basic Aerodynamic Characteristics of the X-31

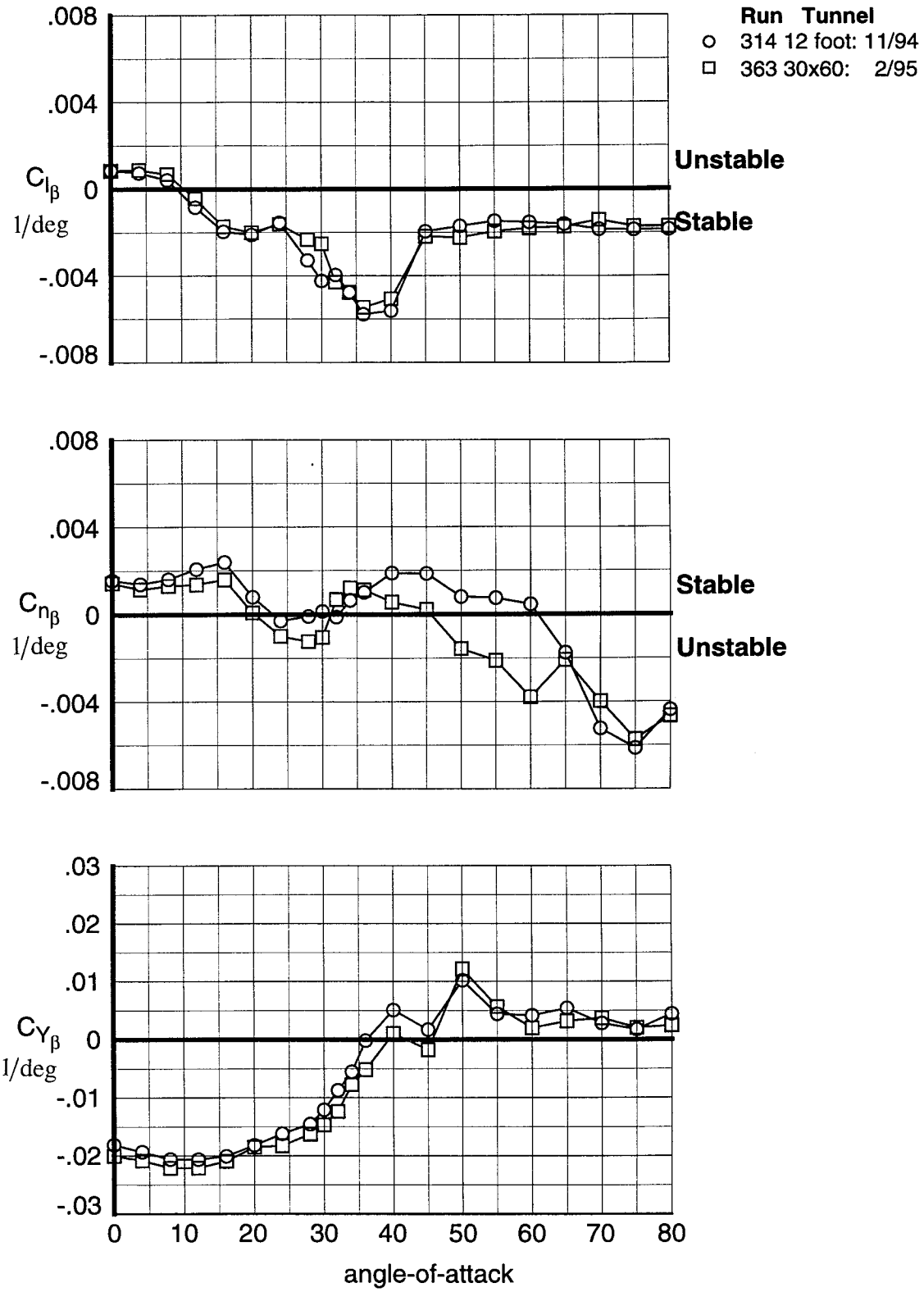

Fig. 7 Variation of Lateral-Directional Stability Between Facilities

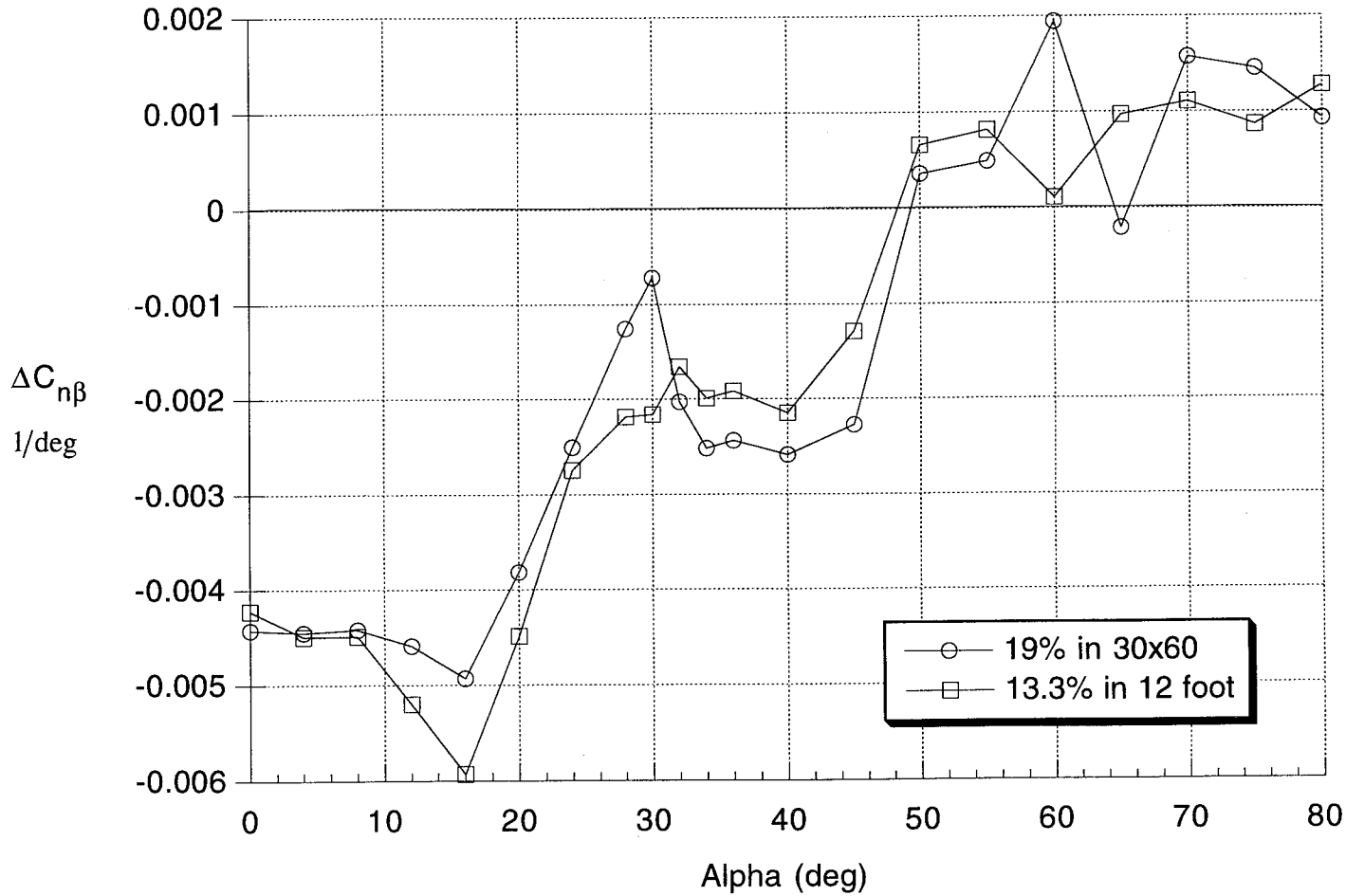

Fig. 8 Effect of Vertical Tail Reduction on $C_{n\beta}$

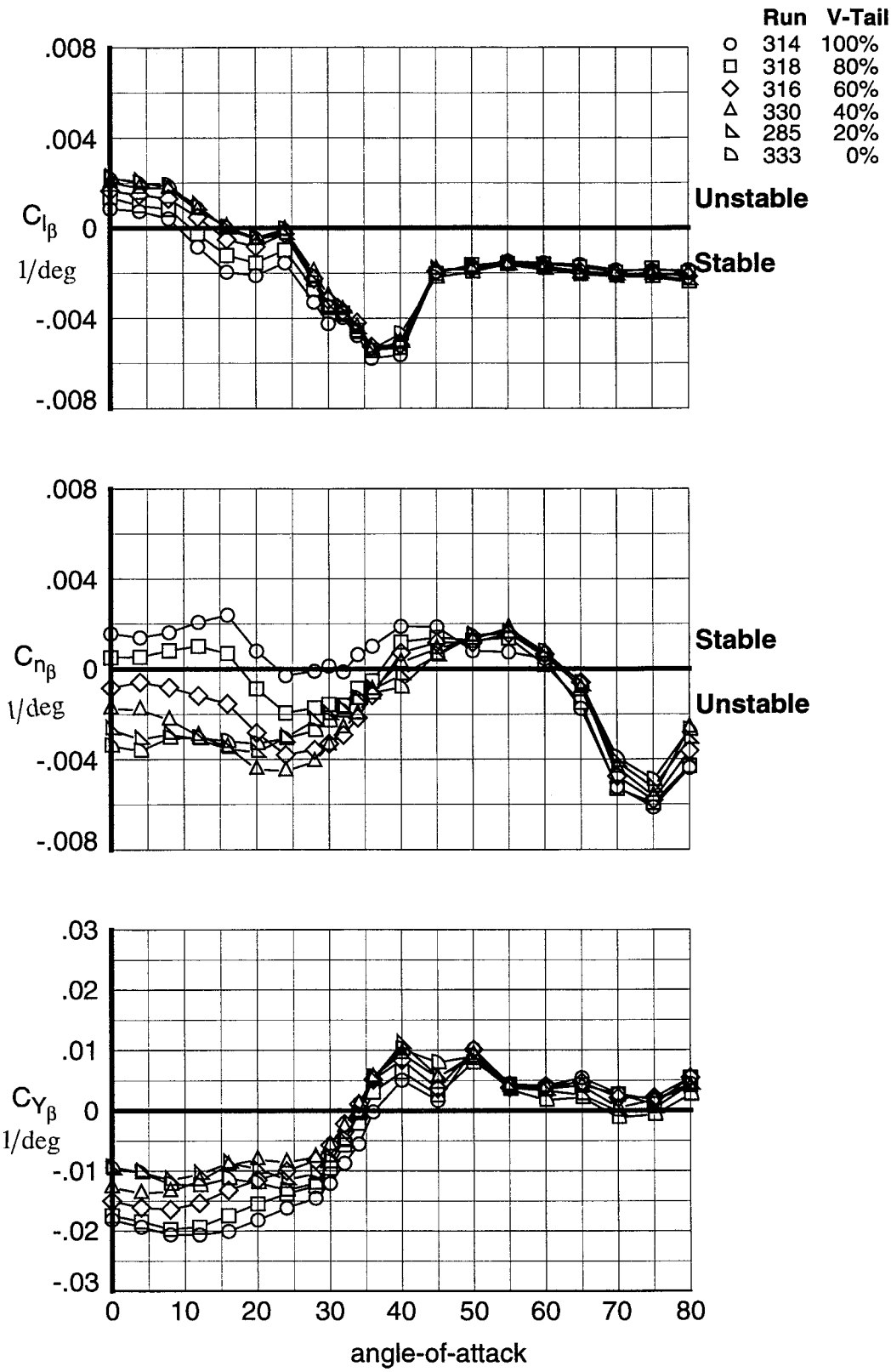

Fig. 9 Effect of Vertical Tail Reduction on Static Lateral-Directional Stability for 13.3% Model in 12-Foot Low Speed Wind-Tunnel

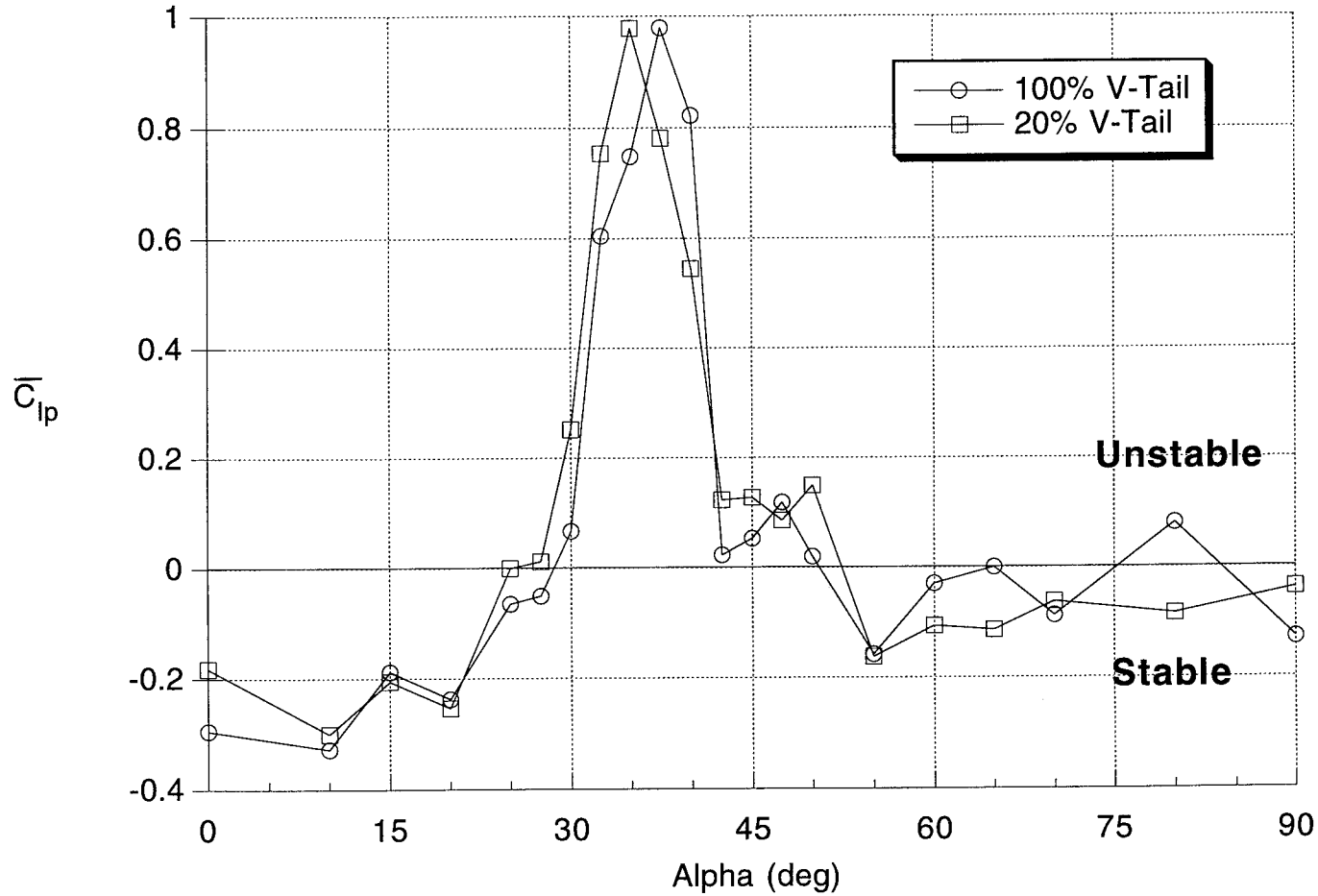

Fig. 10 Vertical Tail Effect on Roll Damping

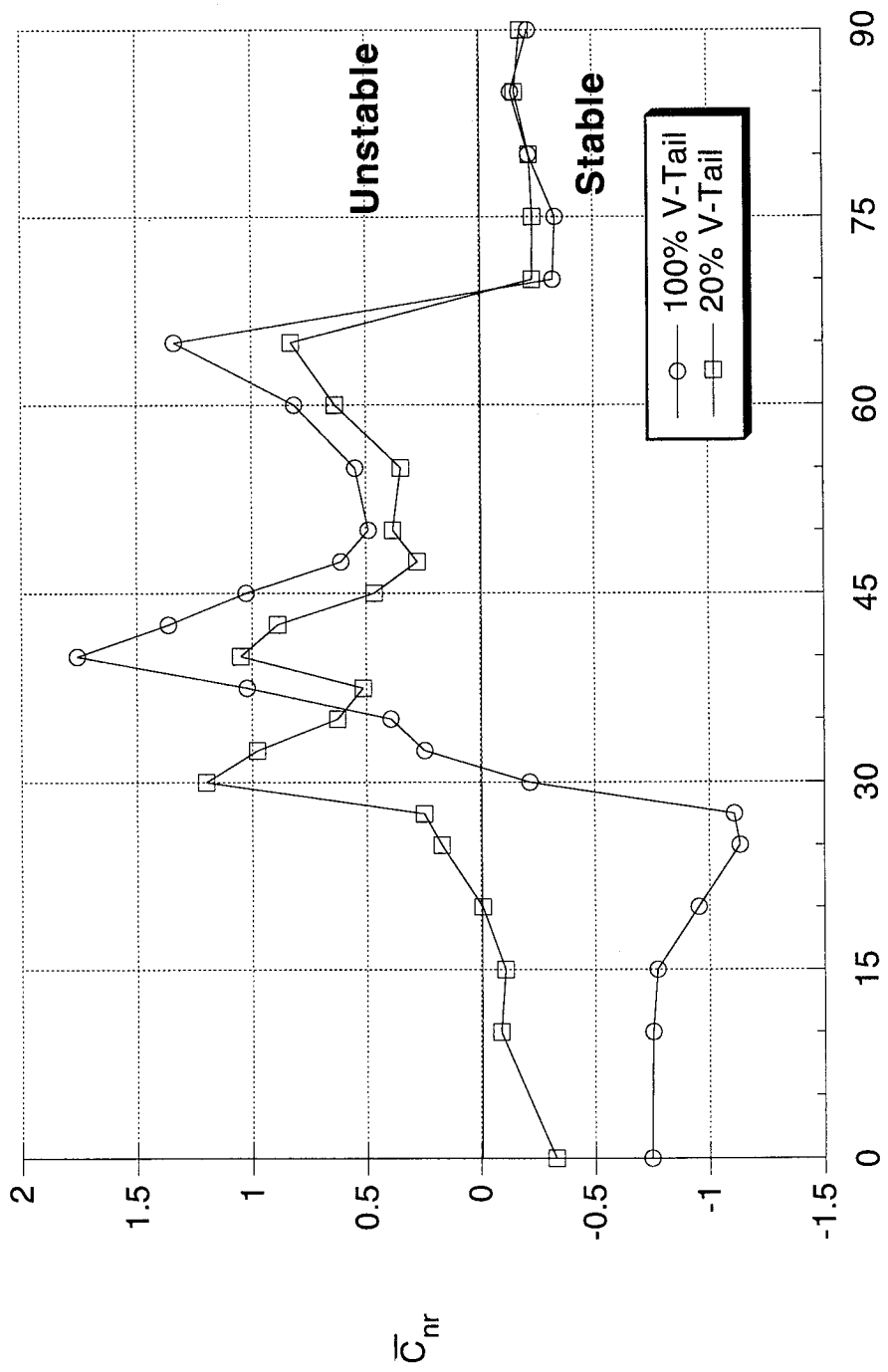

Fig. 11 Vertical Tail Effect on Yaw Damping

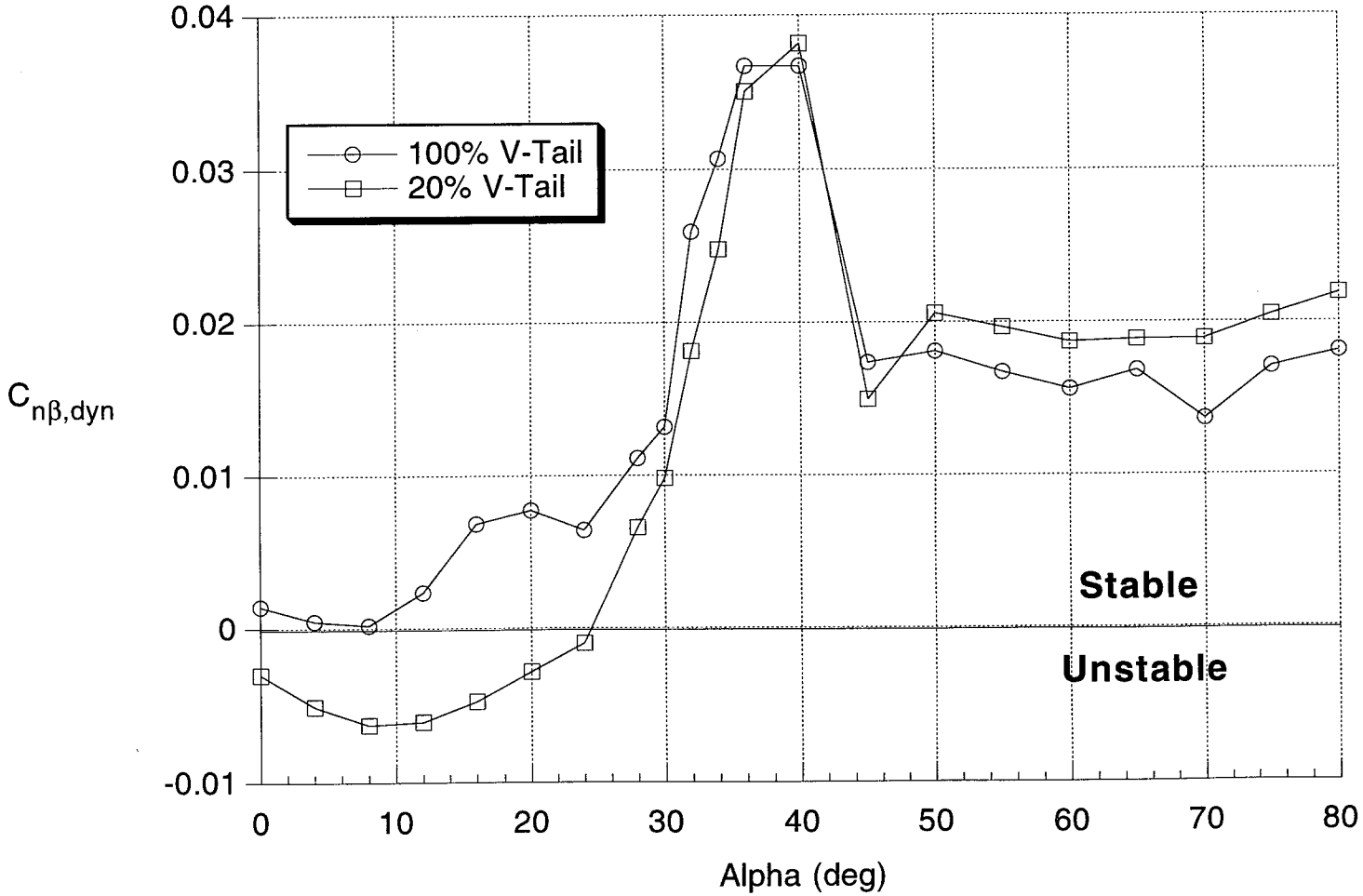

Fig. 12 Vertical Tail Effect on Directional Divergence Parameter

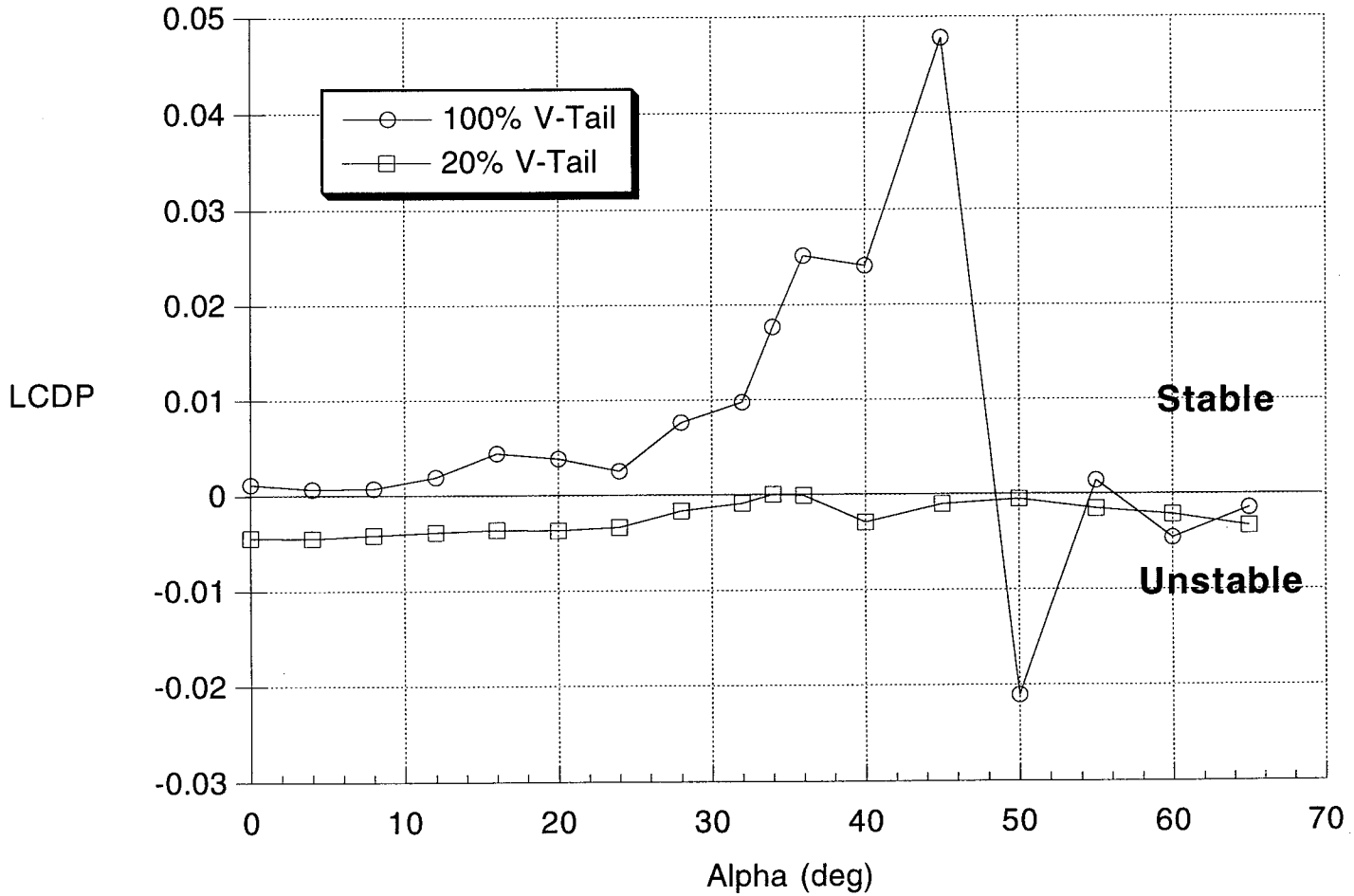

Fig. 13 Vertical Tail Effect on Lateral Control Divergence Parameter

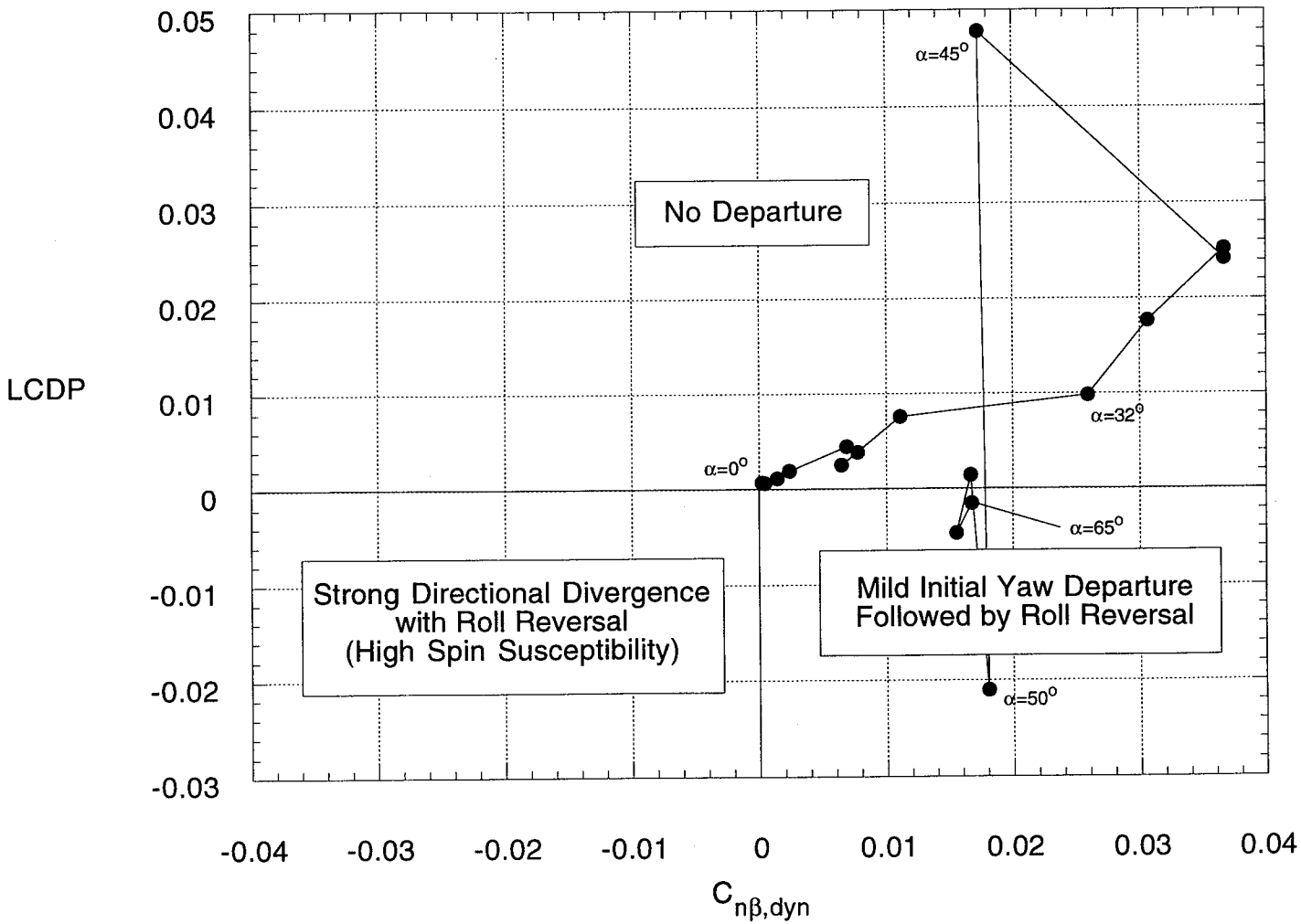

Fig. 14 Departure Criteria for 20% Vertical Tail

C-2

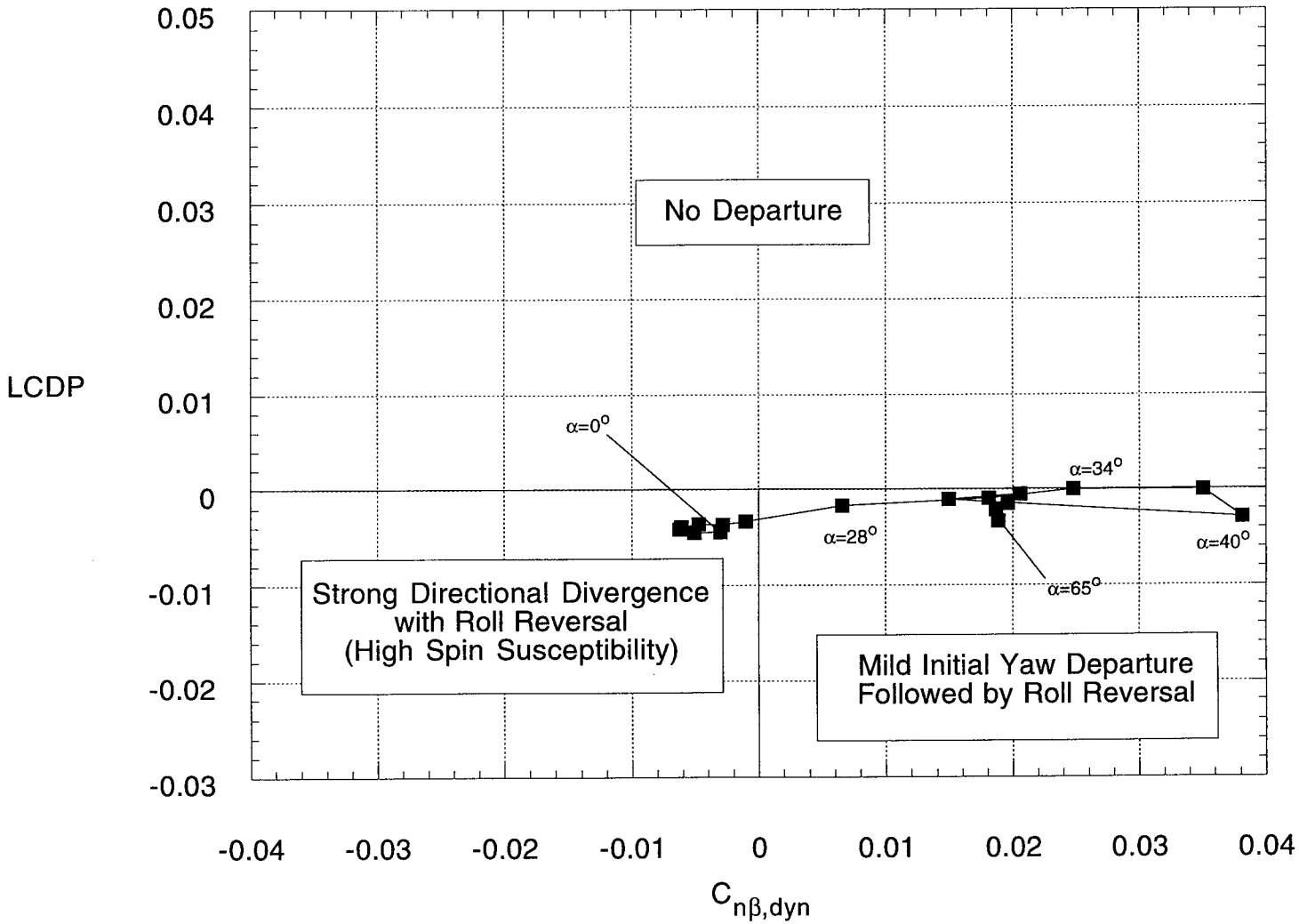

Fig. 15 Departure Criteria for 20% Vertical Tail

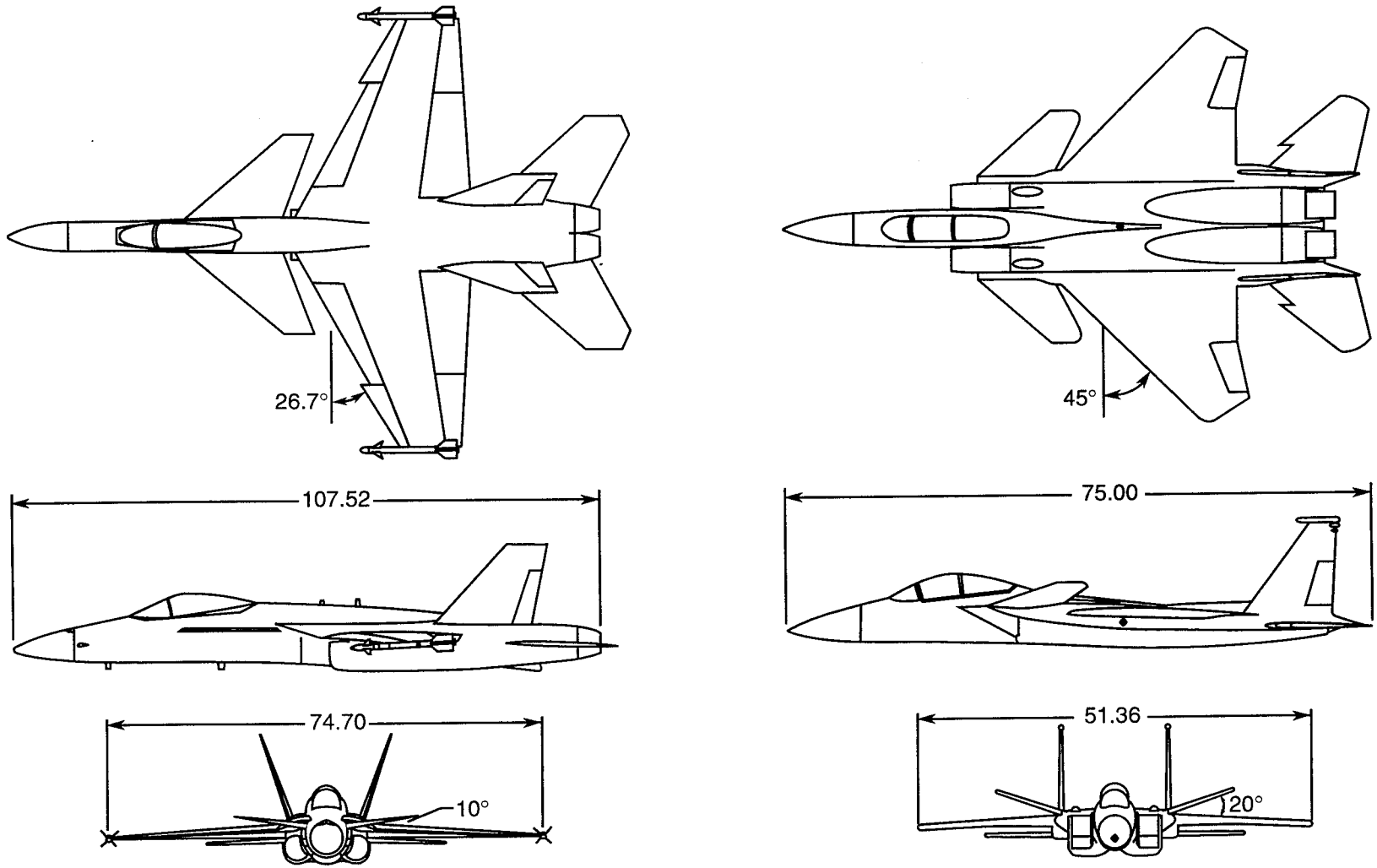

Fig. 16 Directional Control Power of Differential Canard from a Previous Study

a. Configurations Studied

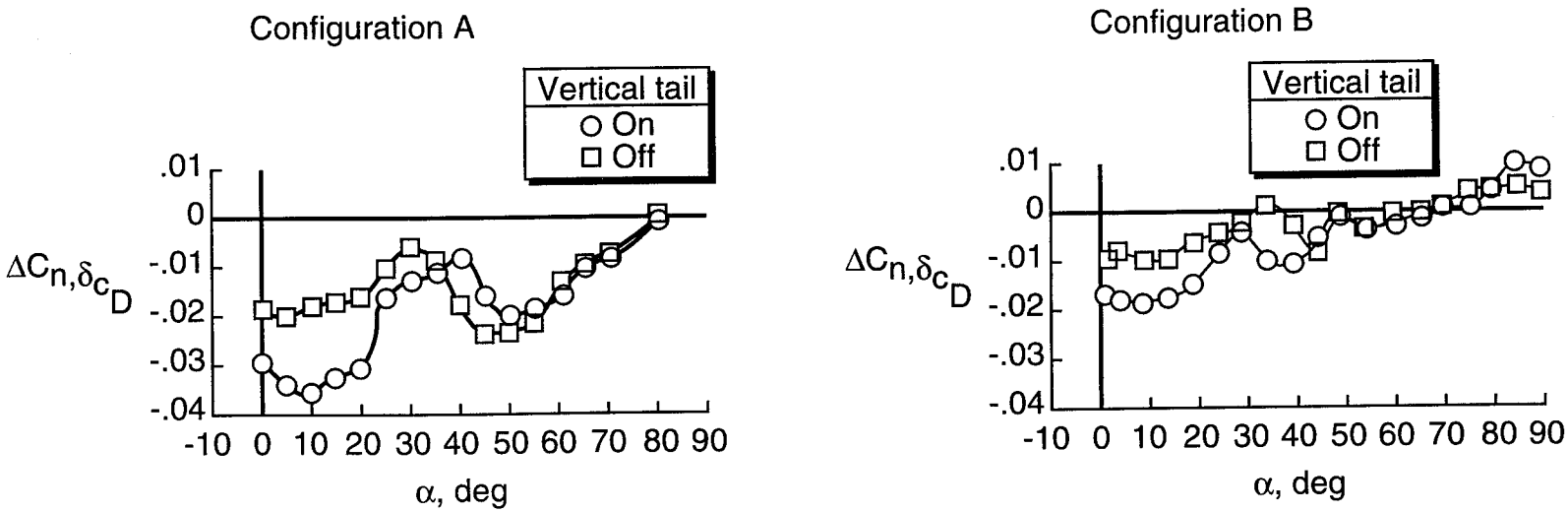

Fig. 16 Directional Control Power of Differential Canard from a

Previous Study

b. Directional Control Power

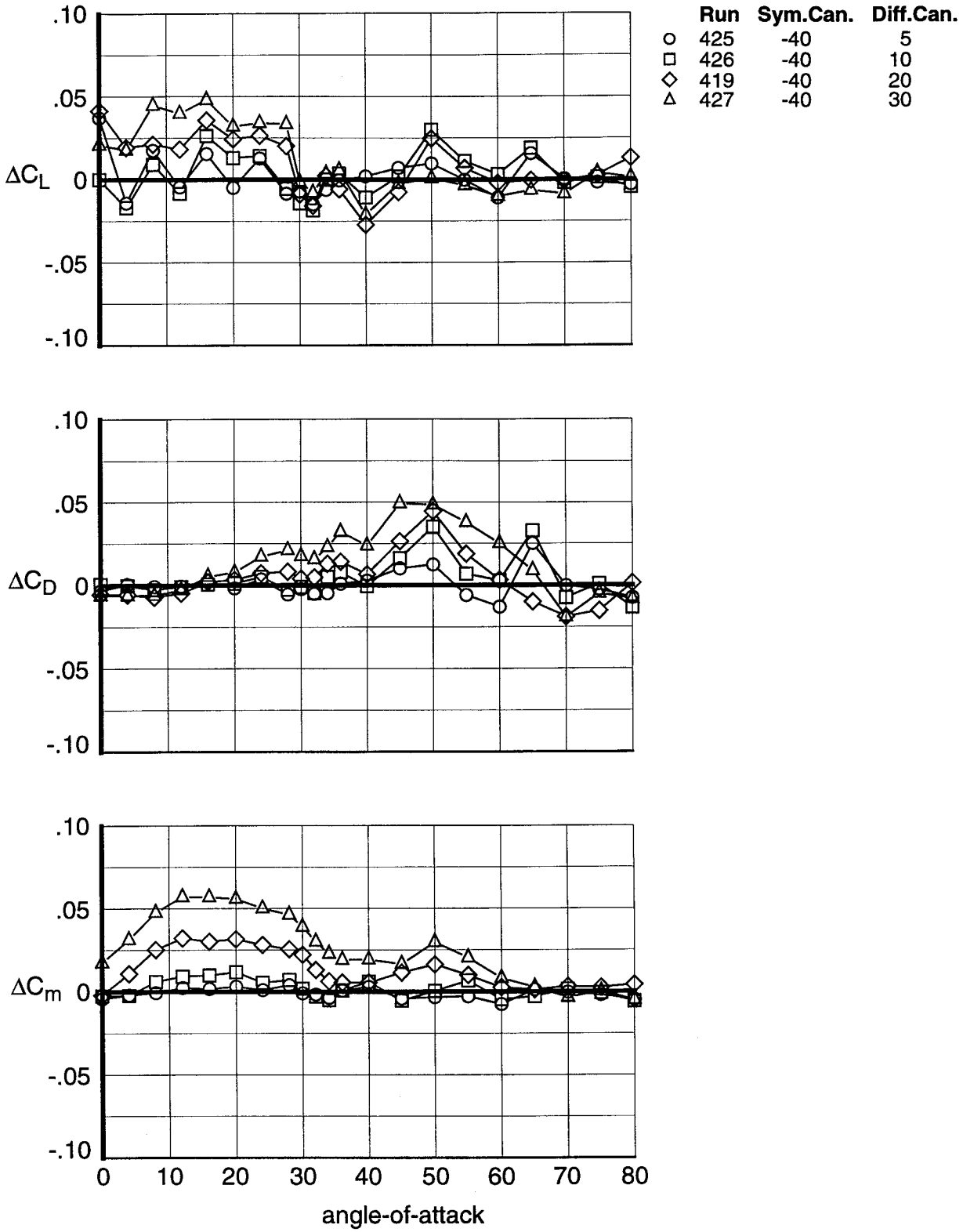

Fig. 17 Effect of Differential Canard Deflection with 100% Vertical Tail for 19% Model in 30- by 60-Foot Tunnel

a. Longitudinal

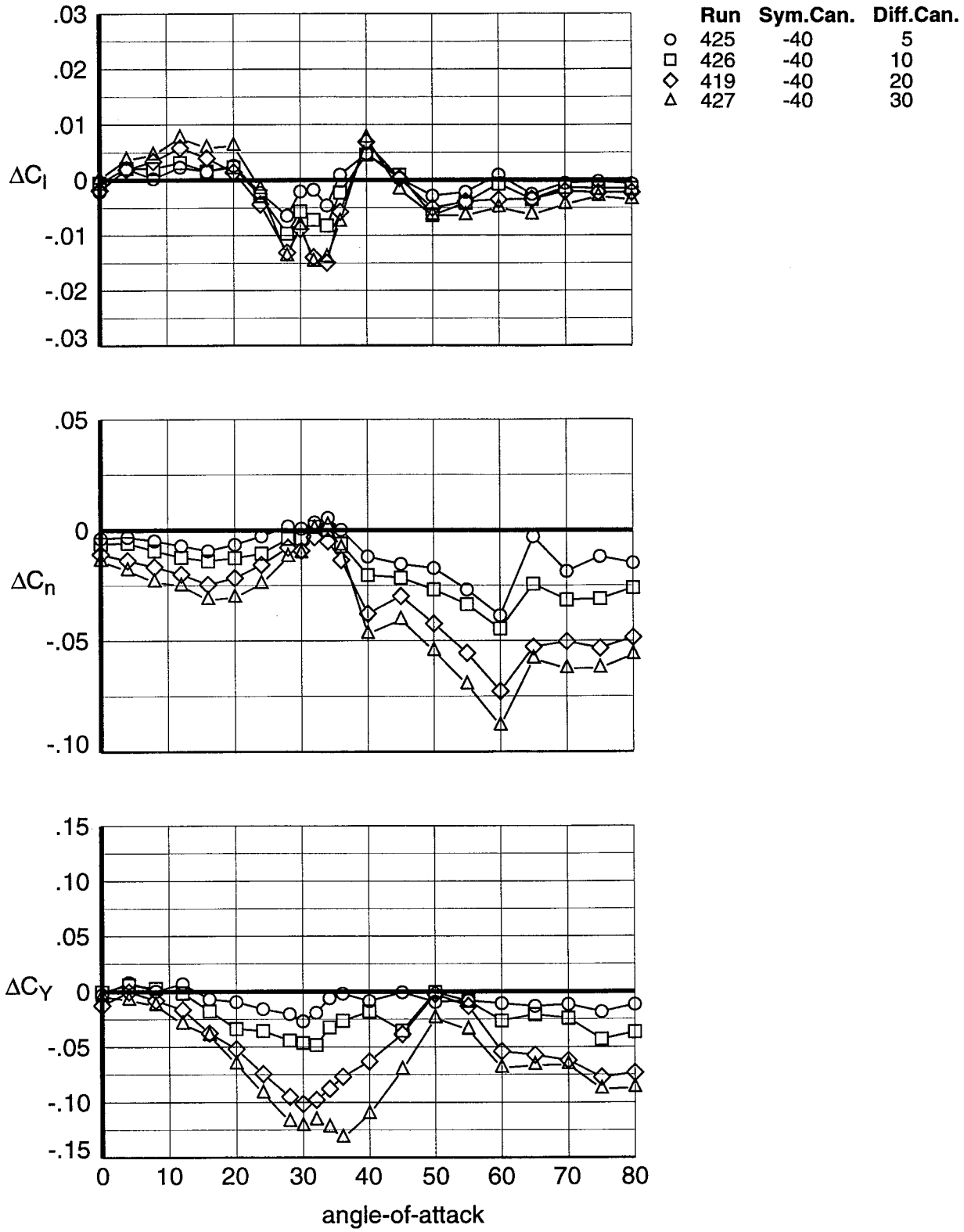

Fig. 17 Effect of Differential Canard Deflection with 100% Vertical Tail for 19% Model in 30- by 60-Foot Tunnel

b. Lateral-Directional

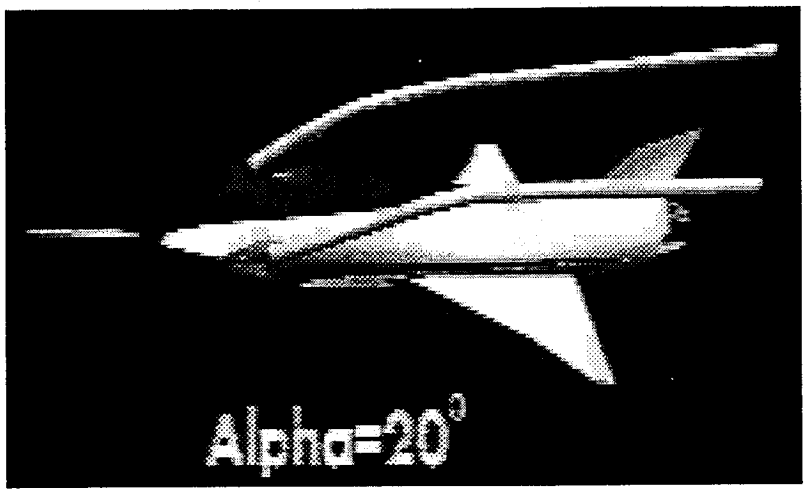

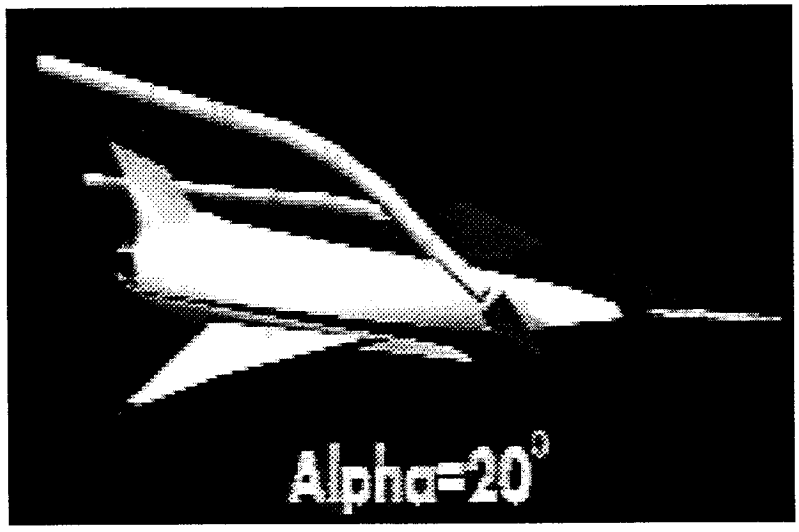

Fig. 18 Visualization of Canard Vorticies with 100% Vertical Tail at $\alpha = 20°$

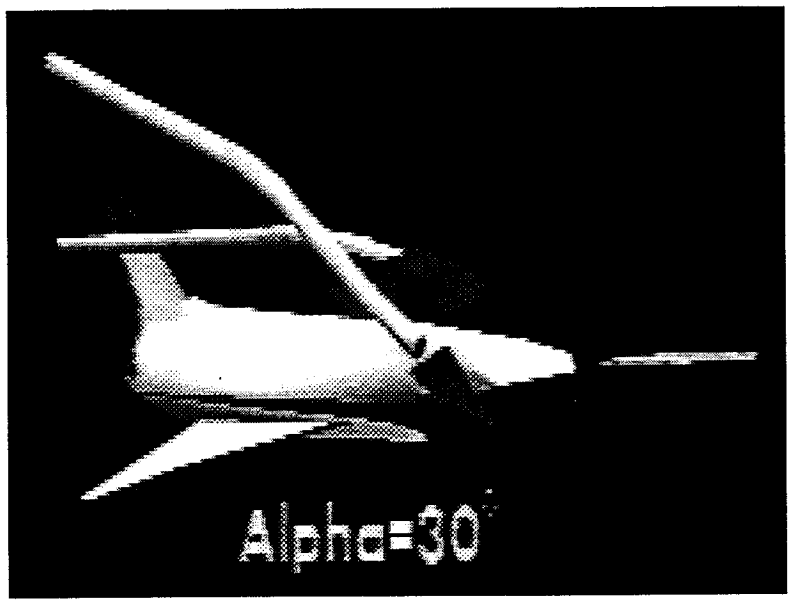

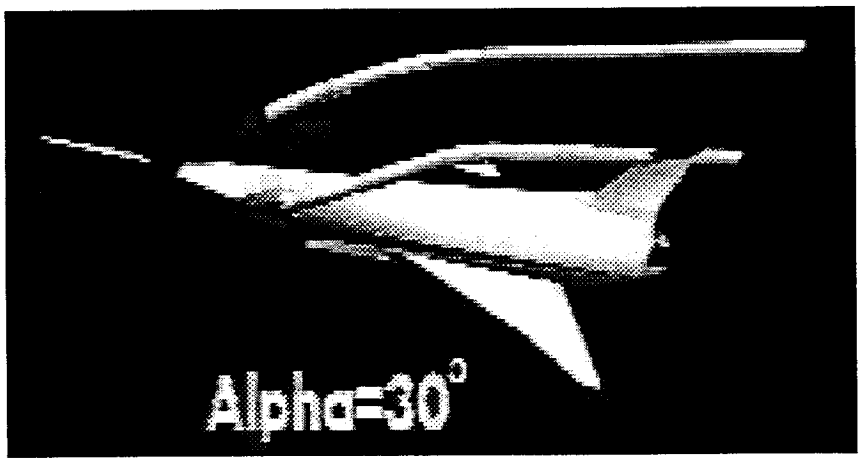

Fig. 19 Visualization of Canard Vorticies with 100% Vertical Tail at $\alpha = 30°$

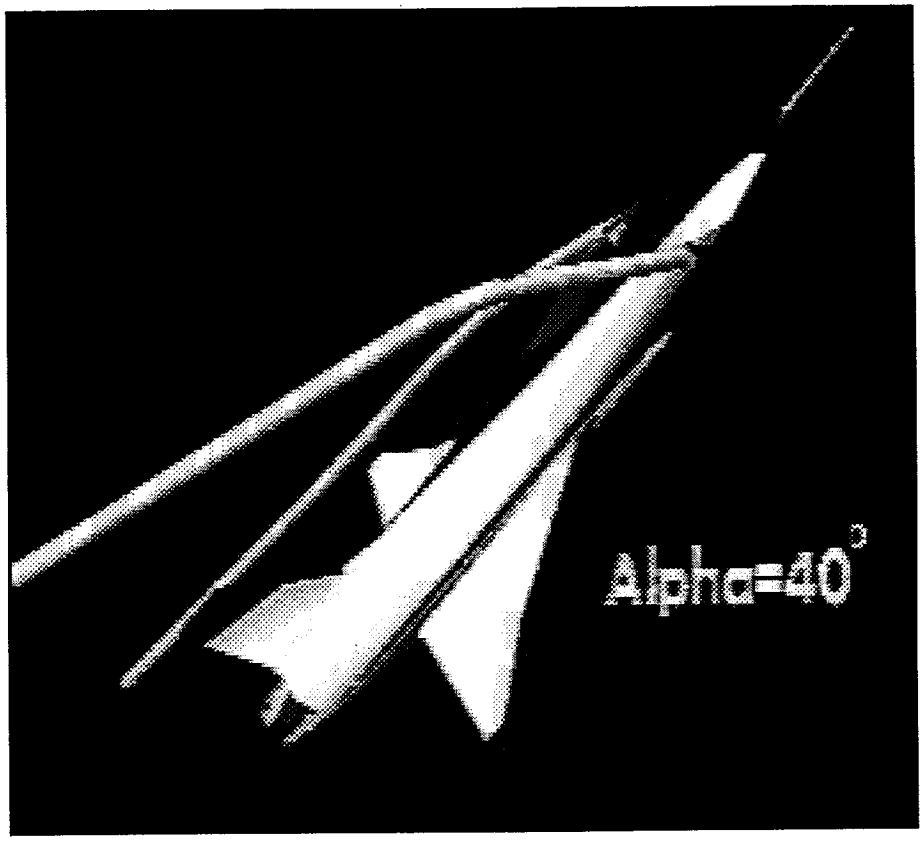

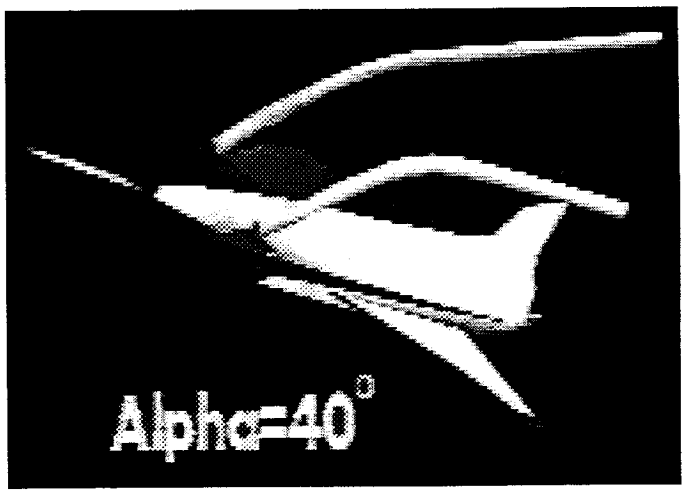

Fig. 20 Visualization of Canard Vorticies with 100% Vertical Tail at $\alpha = 40°$

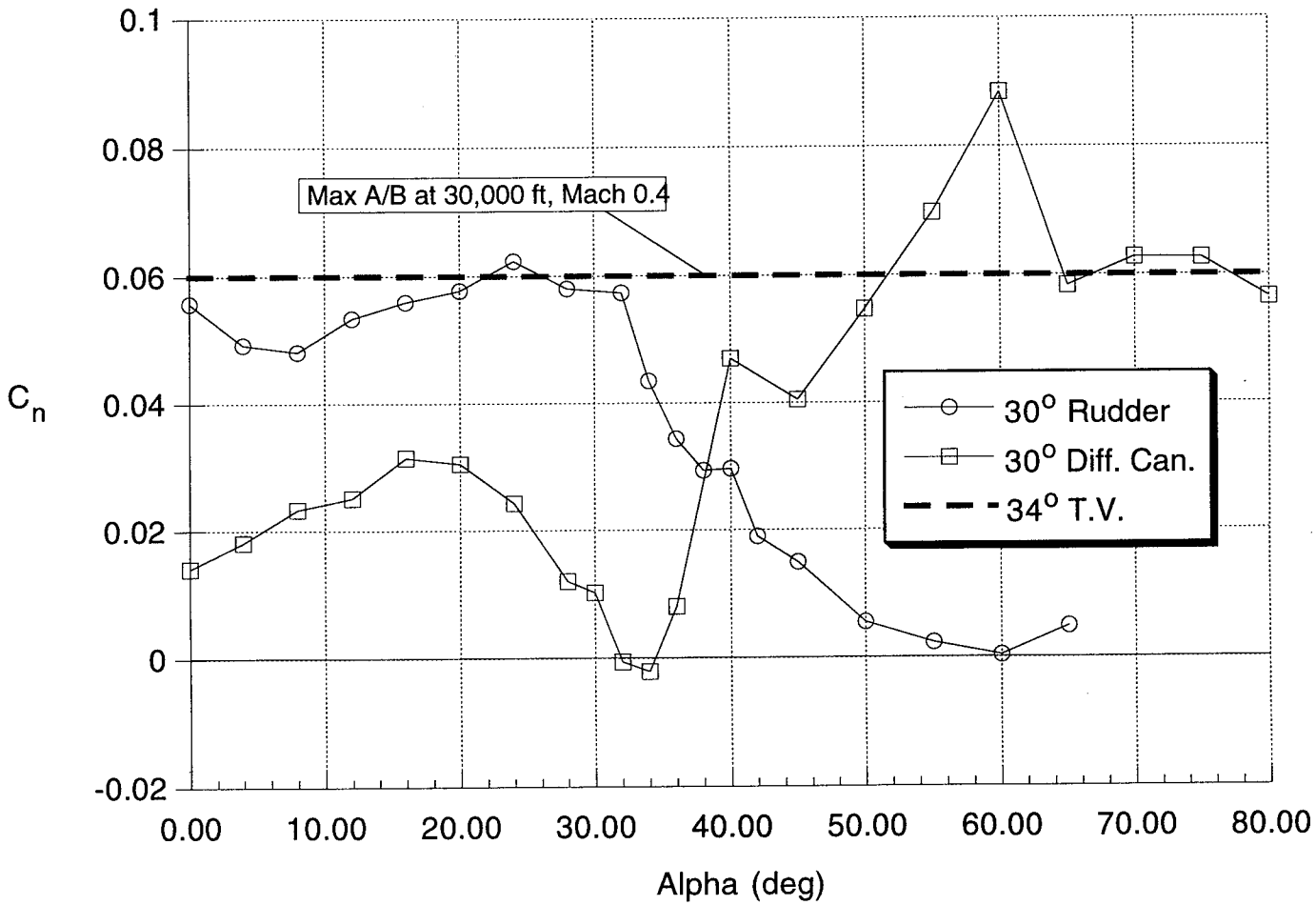

Fig. 21 Directional Control Power Comparison

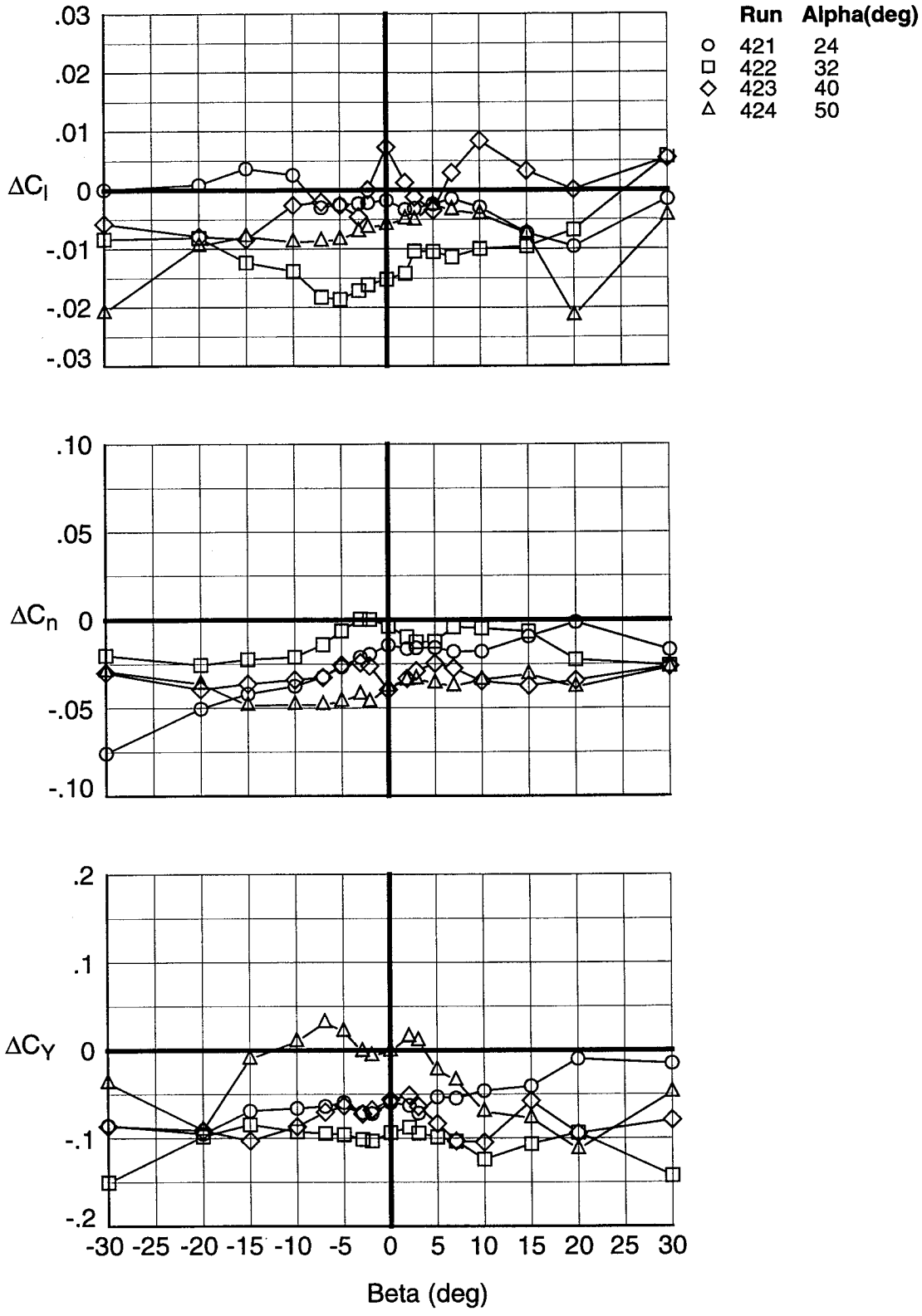

Fig. 22 Effectiveness of 20° Differential Canard at Sideslip for 19% Model in 30- by 60-Foot Tunnel

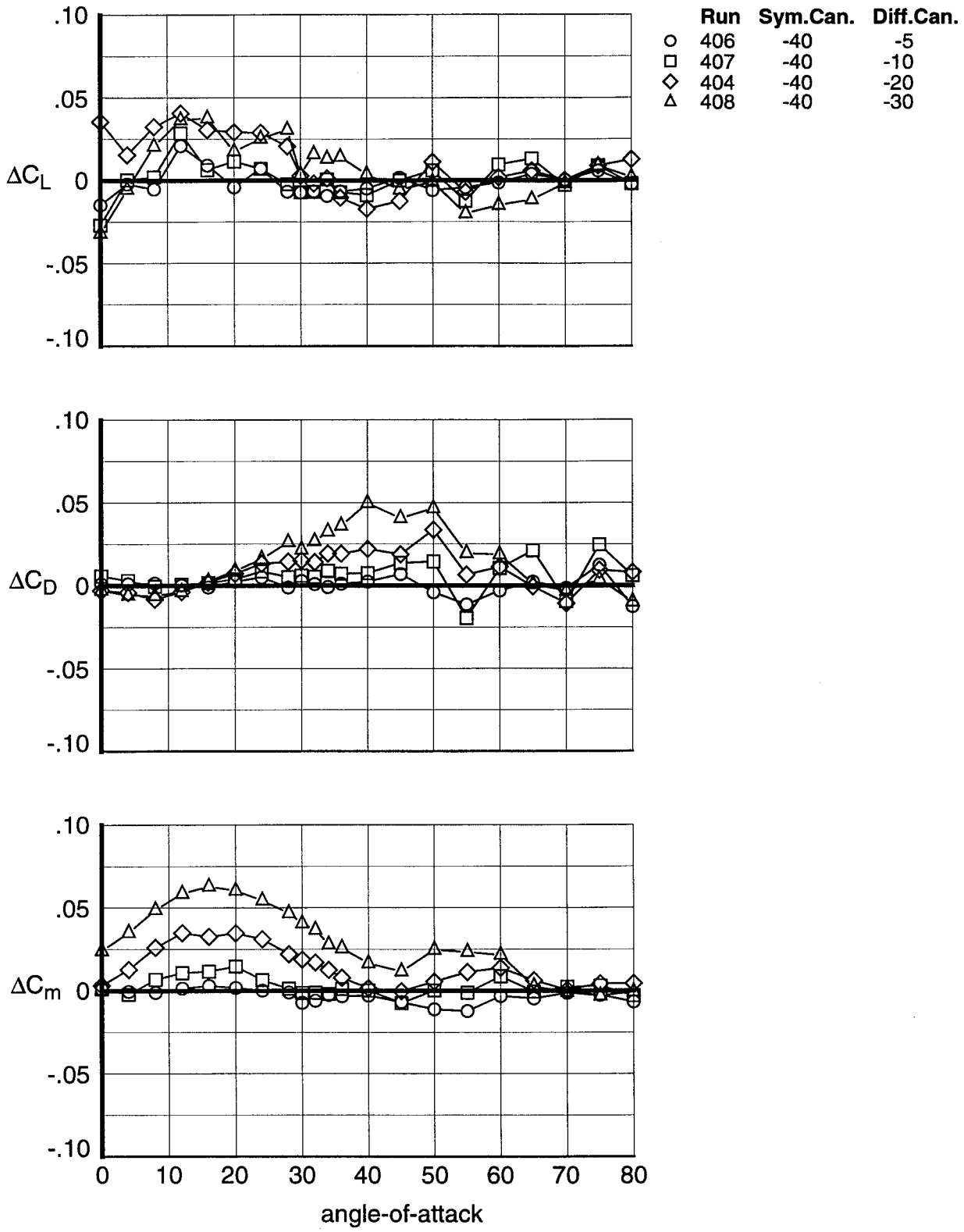

Fig. 23 Effect of Differential Canard Deflection with 20% Vertical Tail for 19% Model in 30- by 60-Foot Tunnel

a. Longitudinal

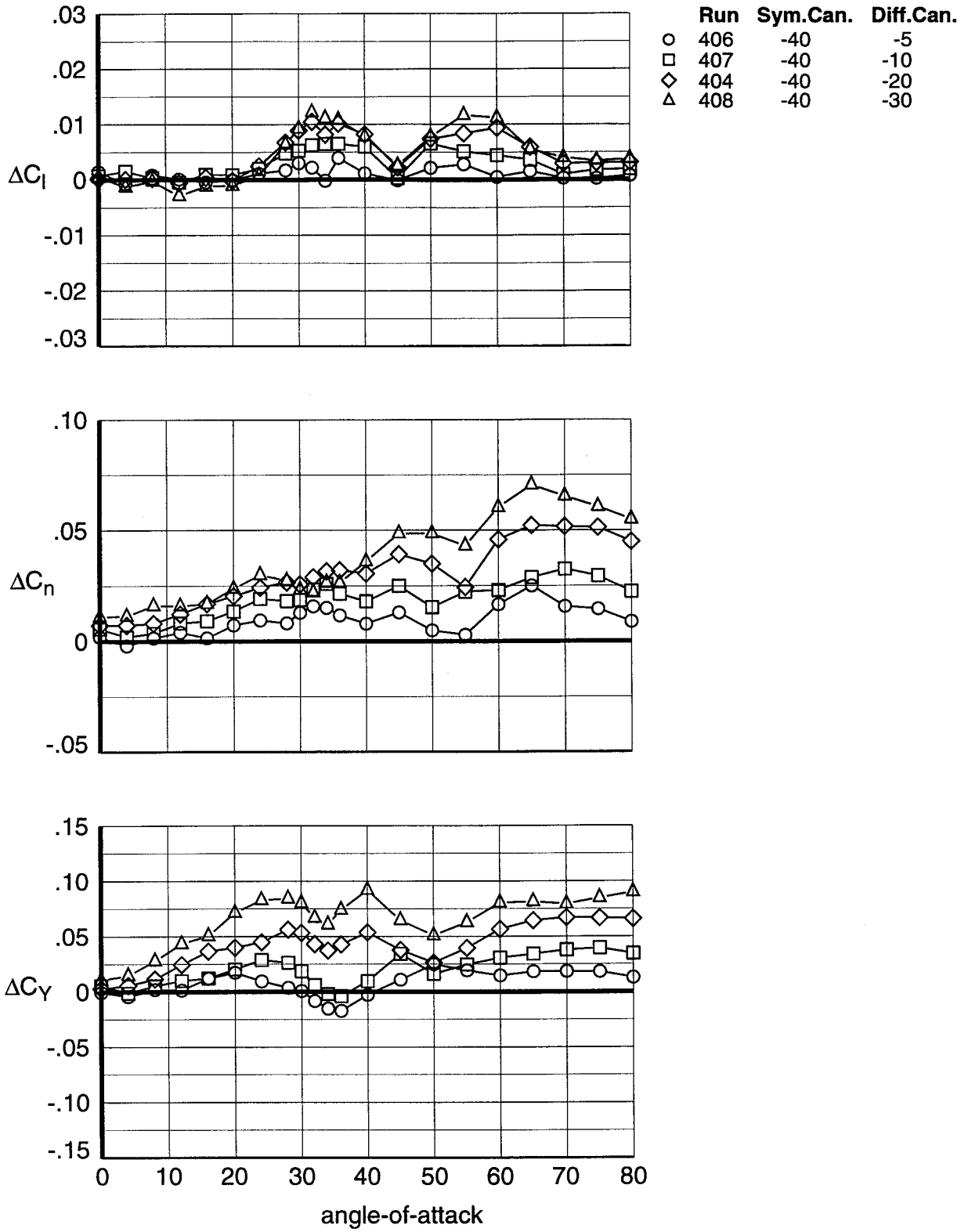

Fig. 23 Effect of Differential Canard Deflection with 20% Vertical Tail for 19% Model in 30- by 60-Foot Tunnel

b. Lateral-Directional

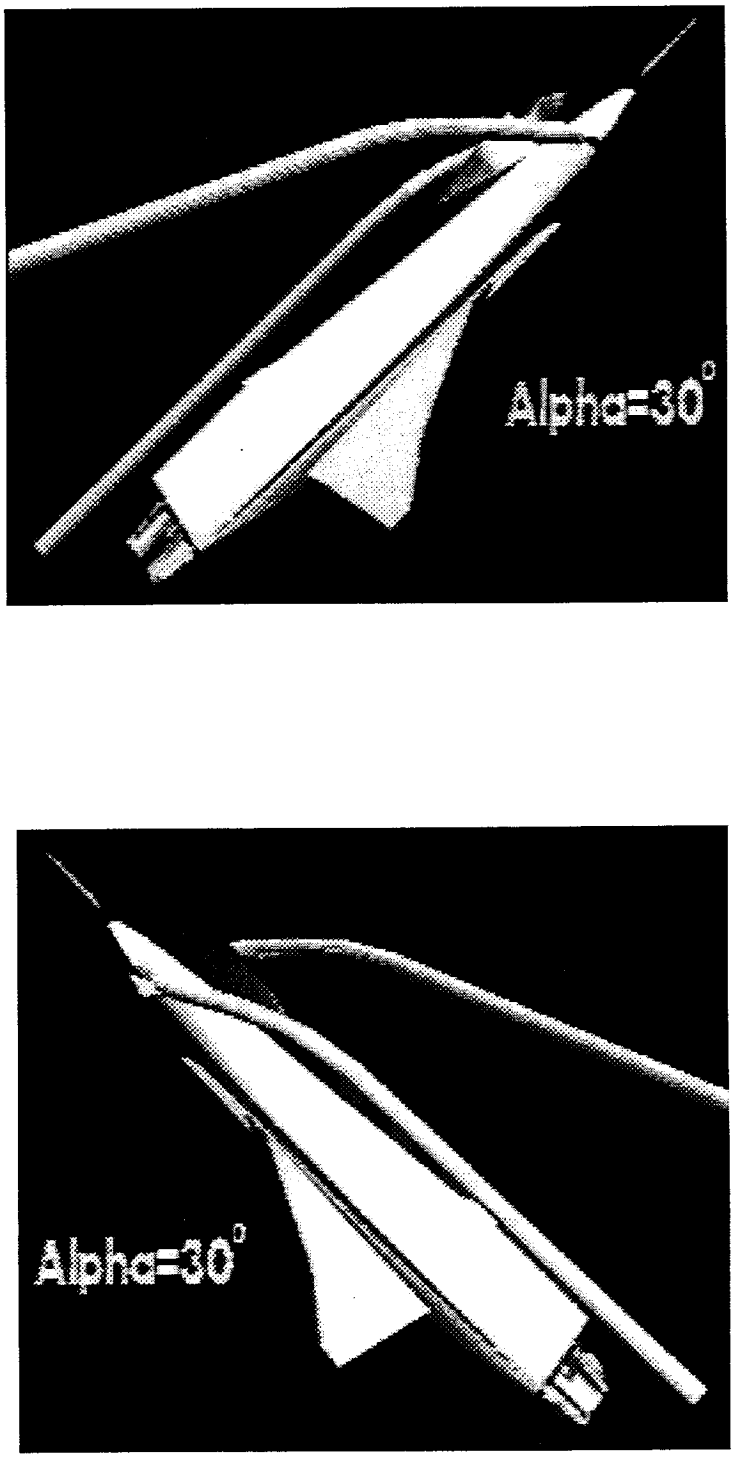

Fig. 24 Visualization of Canard Vorticies with 20% Vertical Tail at $\alpha = 30°$

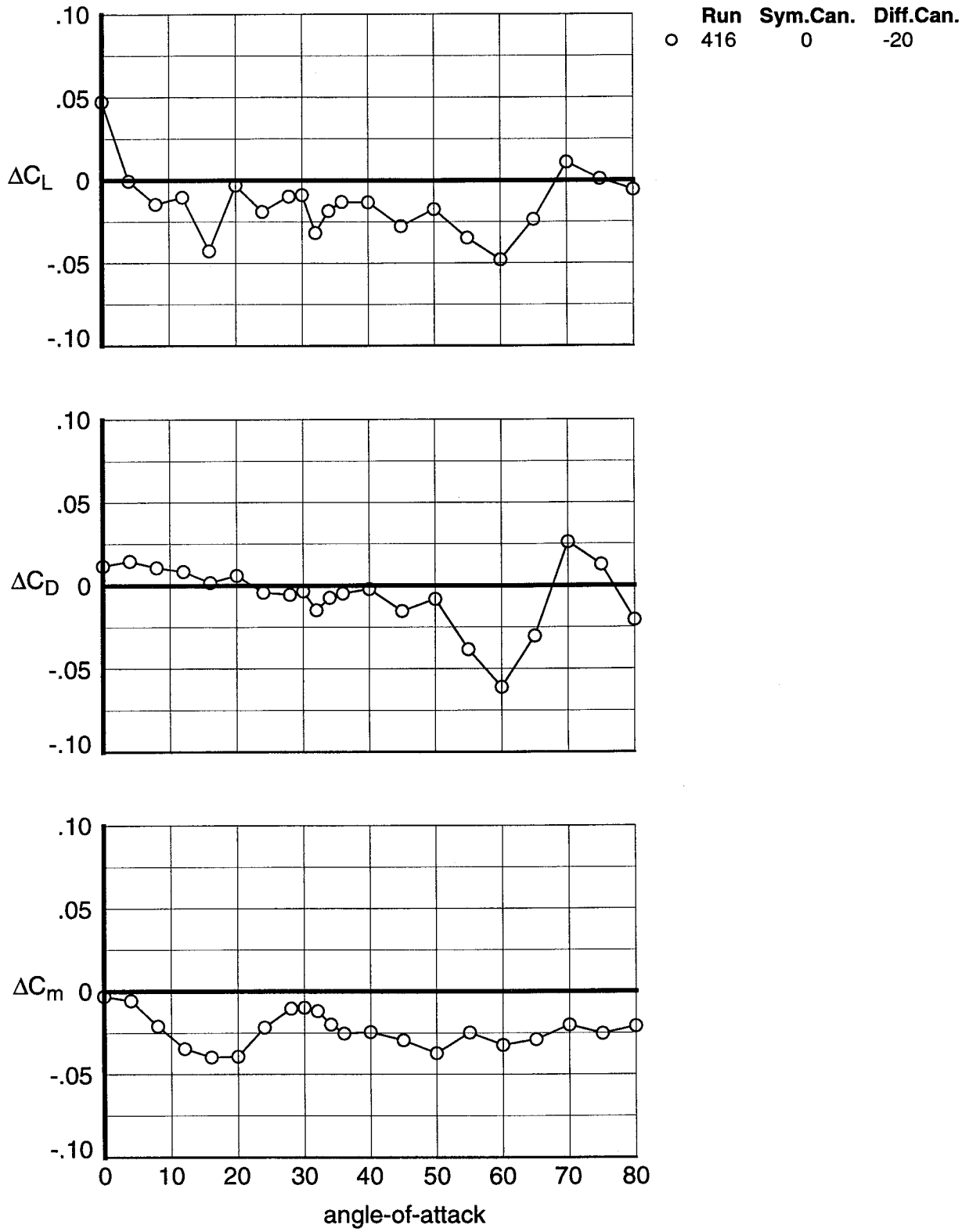

Fig. 25 Effect of Differential Canard Deflection with 100% Vertical Tail for 19% Model in 30- by 60-Foot Tunnel

a. Longitudinal

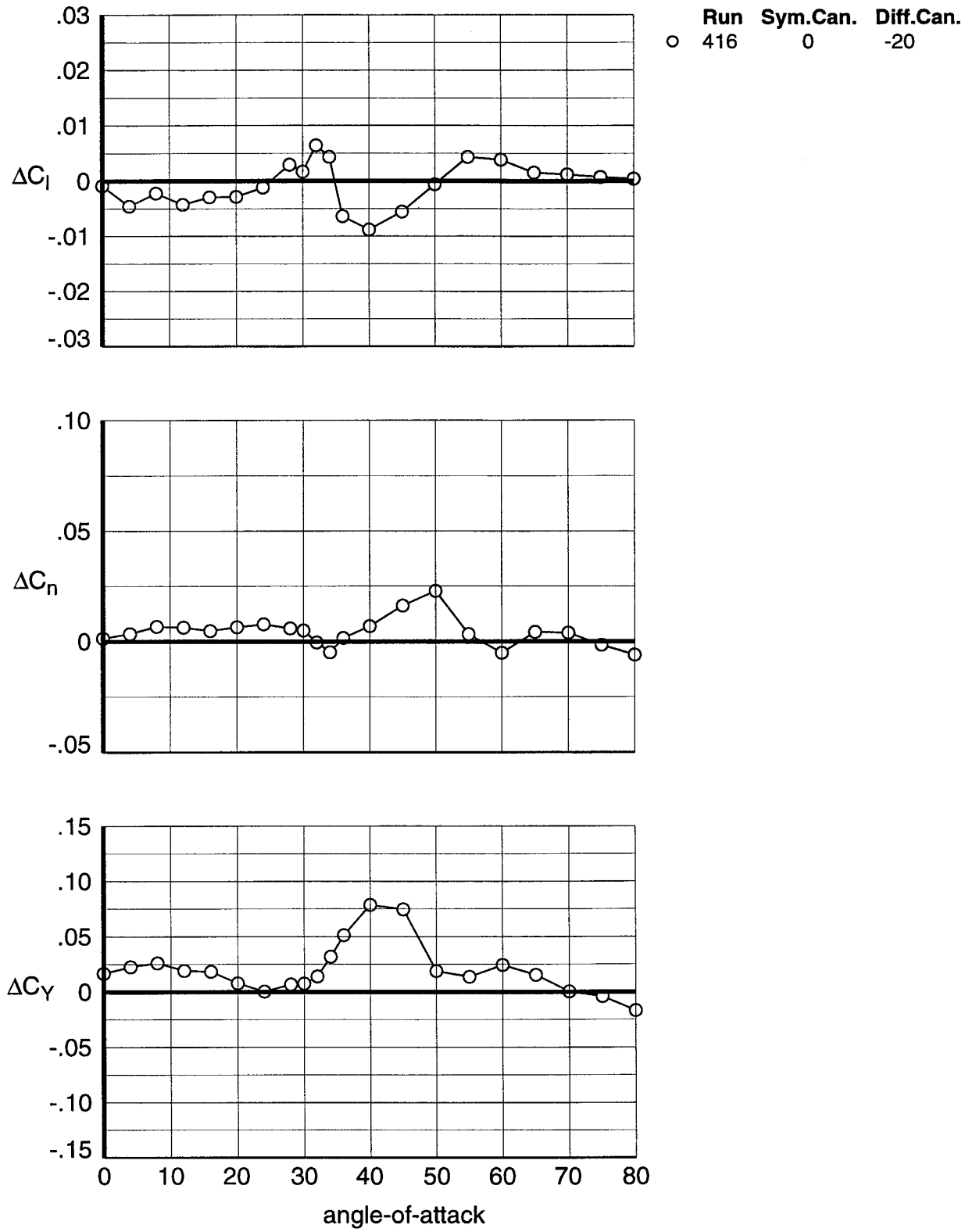

Fig. 25 Effect of Differential Canard Deflection with 100% Vertical Tail for 19% Model in 30- by 60-Foot Tunnel

b. Lateral-Directional

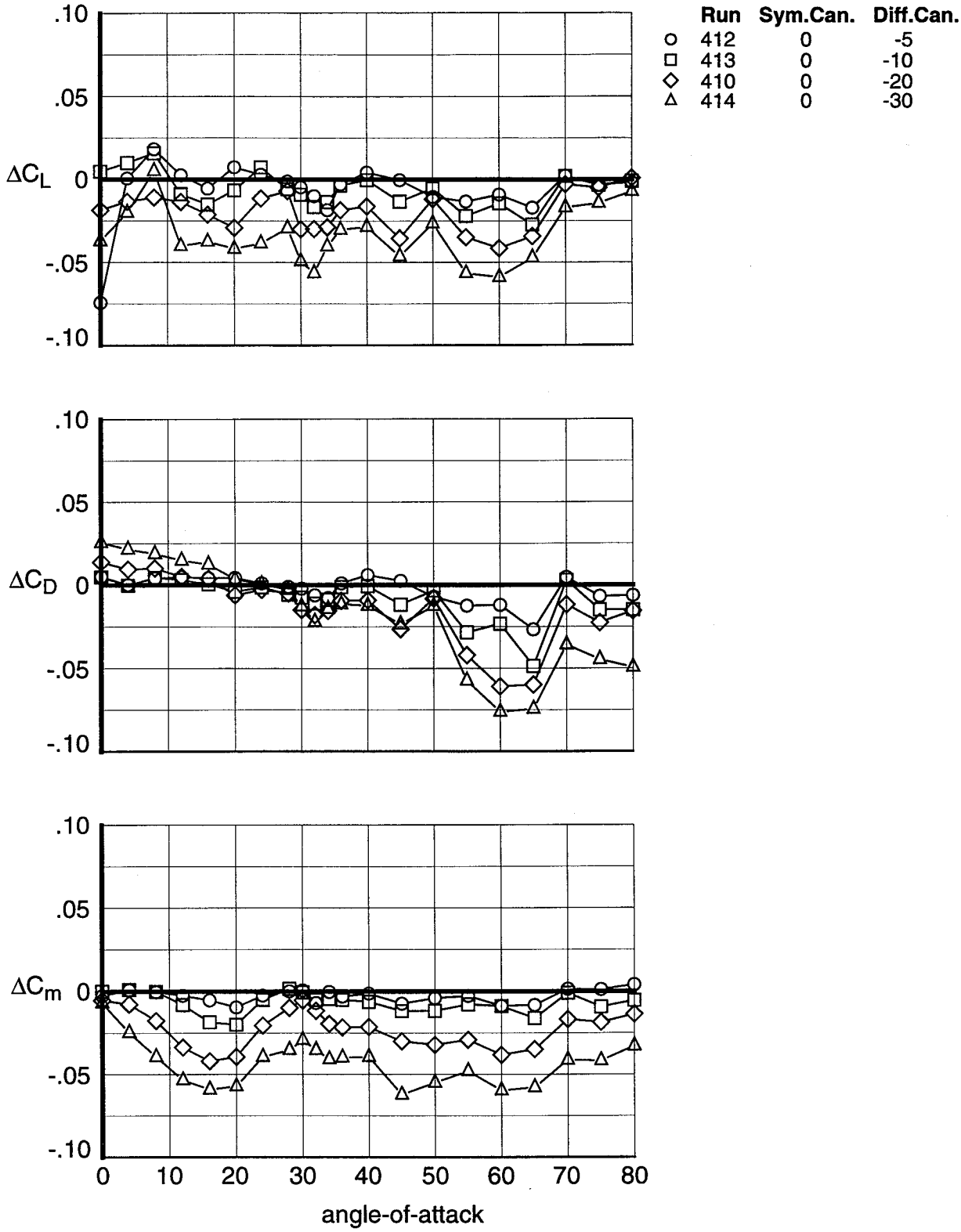

Fig. 26 Effect of Differential Canard Deflection with 20% Vertical Tail for 19% Model in 30- by 60-Foot Tunnel

a. Longitudinal

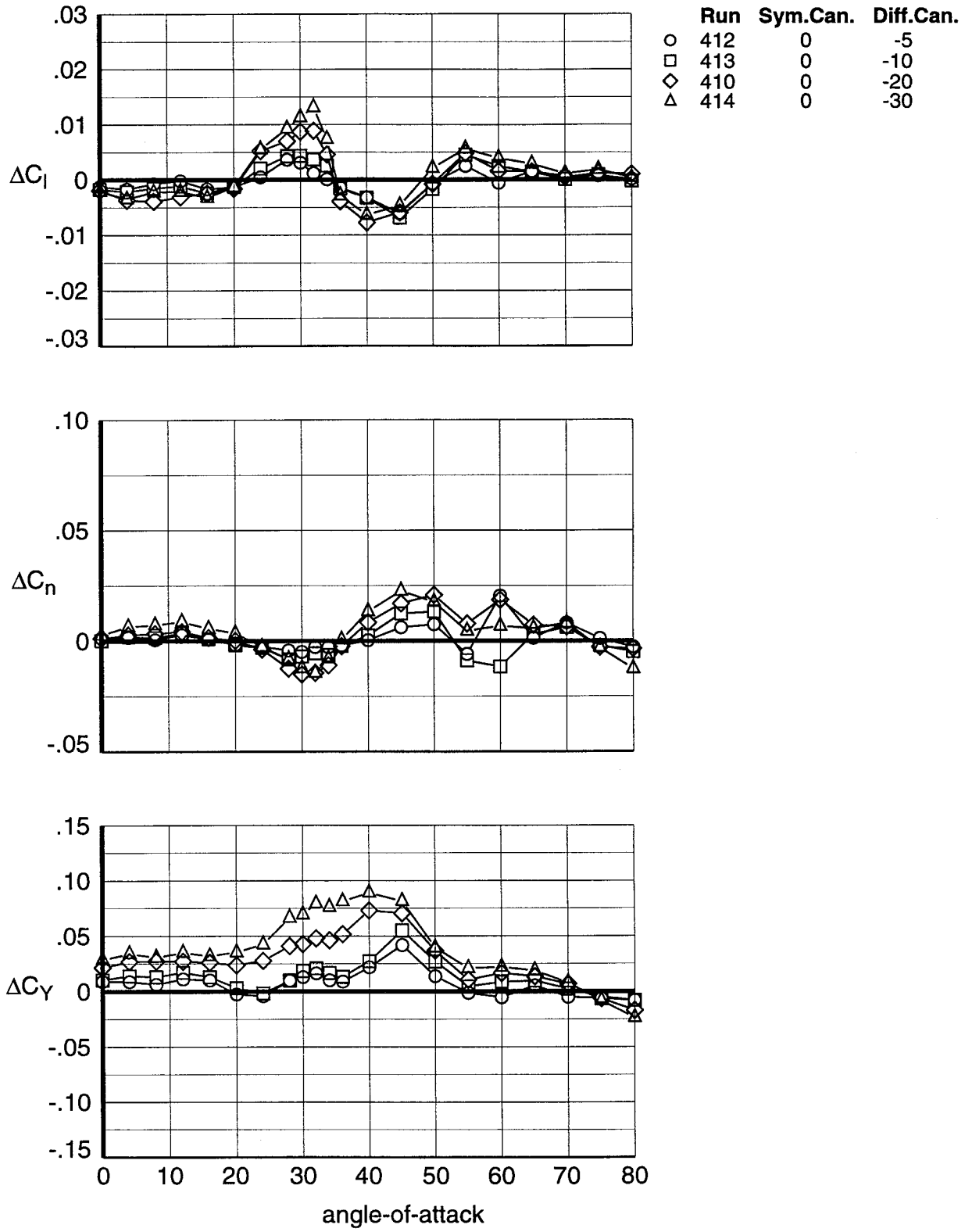

Fig. 26 Effect of Differential Canard Deflection with 20% Vertical Tail for 19% Model in 30- by 60-Foot Tunnel

b. Lateral-Directional

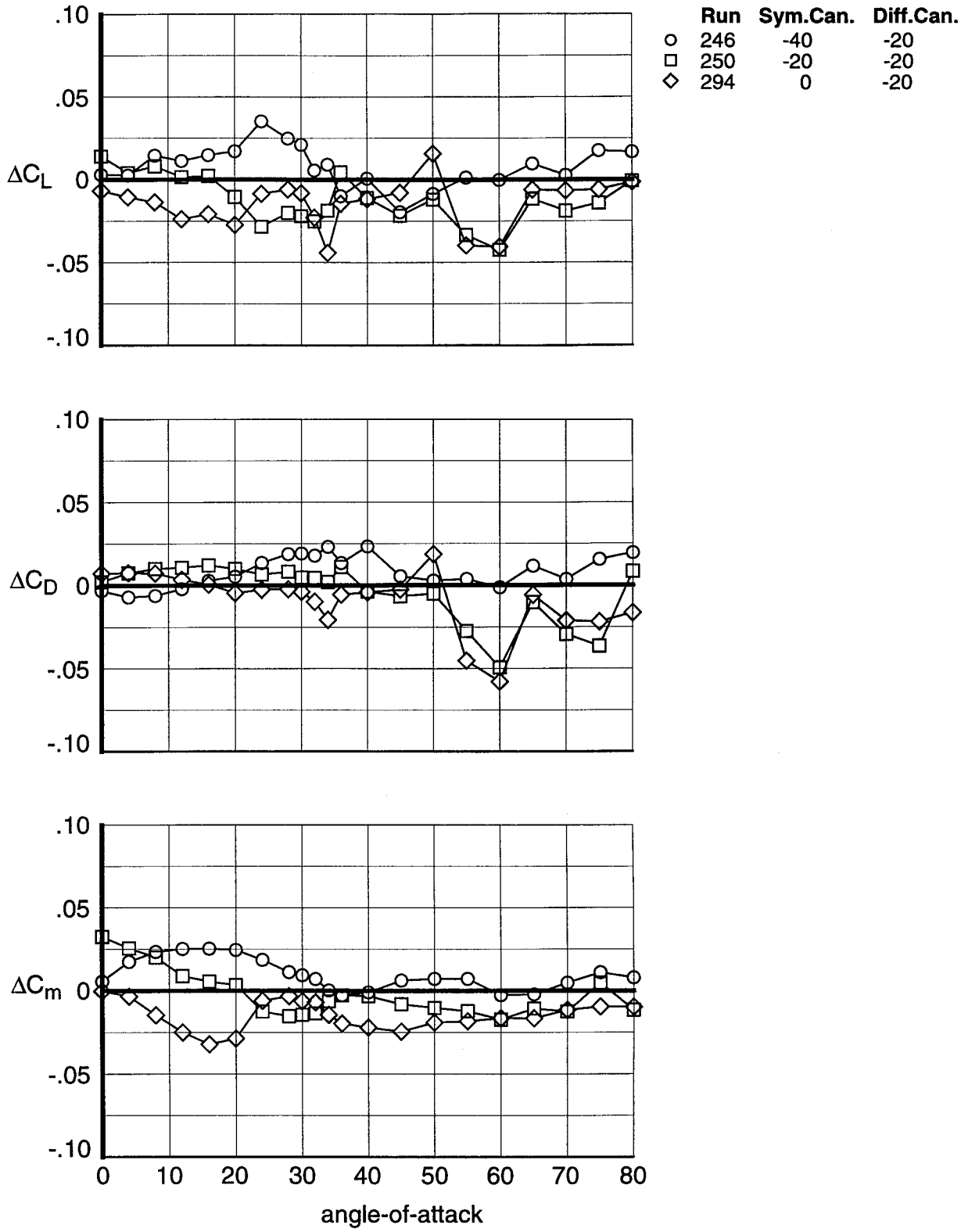

Fig. 27 Effect of Symmetric Canard on Differential Canard Control Power for 13.3% Model in 12-Foot Low Speed Tunnel

a. Longitudinal

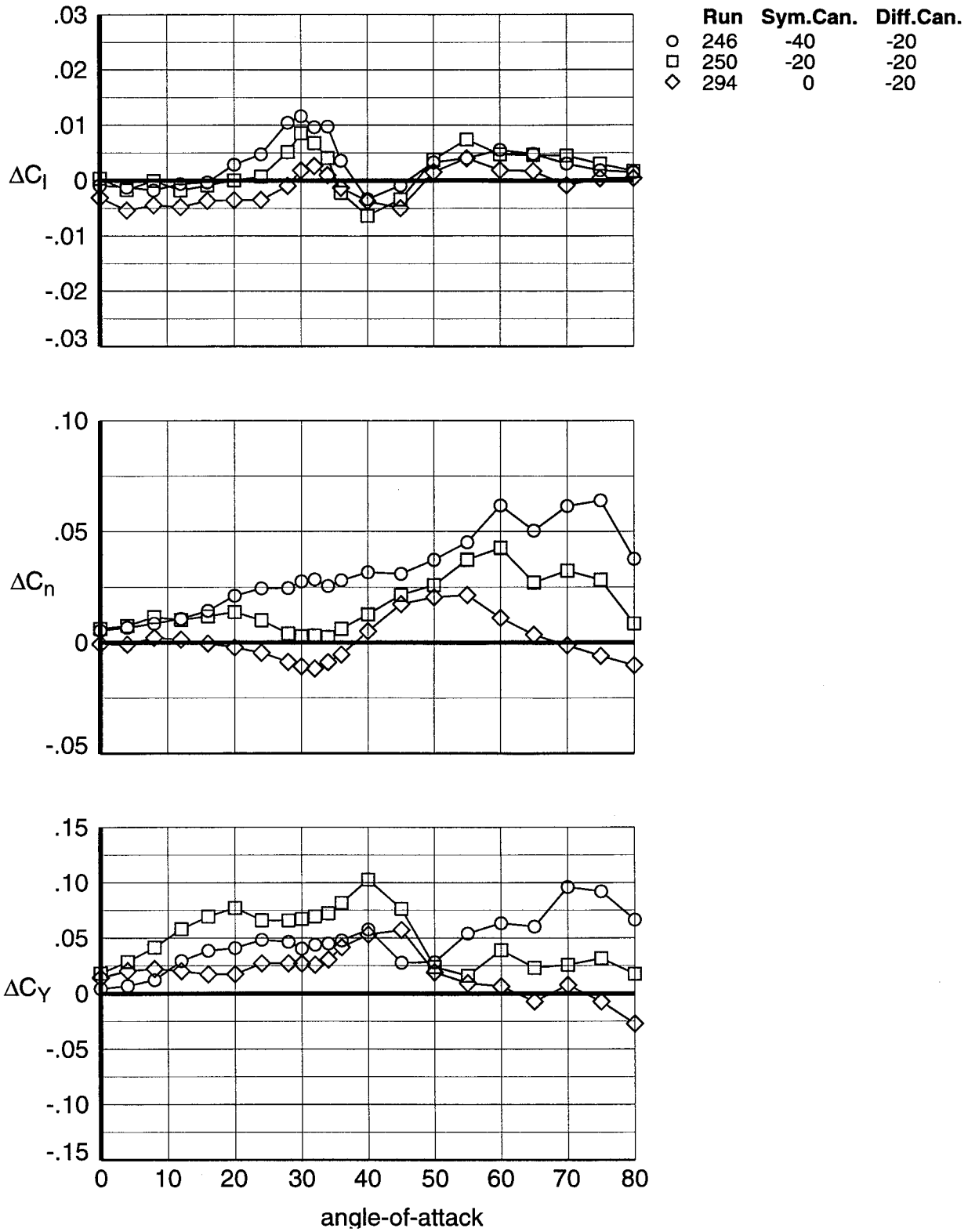

Fig. 27 Effect of Symmetric Canard on Differential Canard Control Power for 13.3% Model in 12-Foot Low Speed Tunnel

b. Lateral-Directional

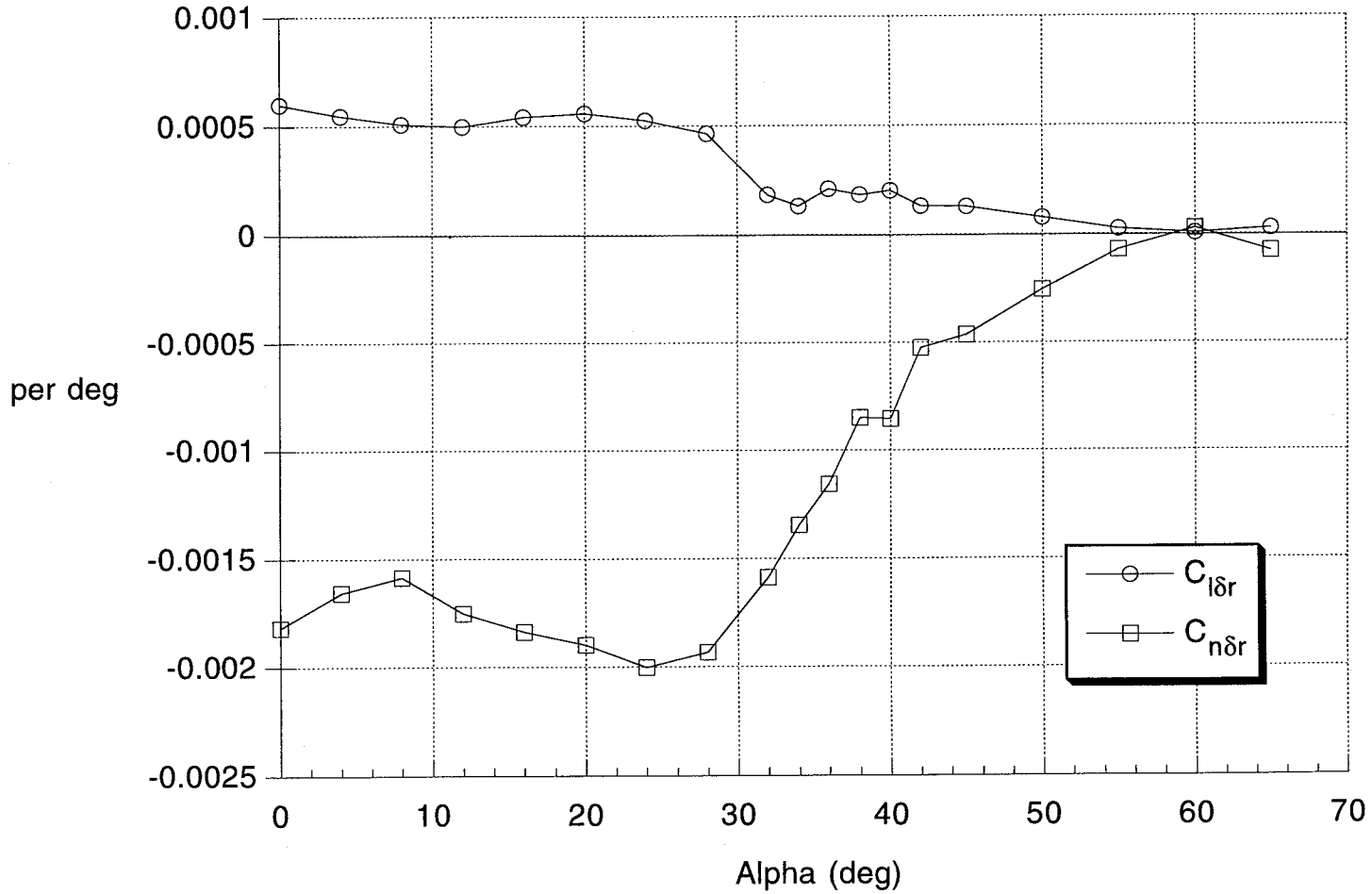

Fig. 28 Rudder Control Power for 19% Model in 30- by 60-Foot Tunnel

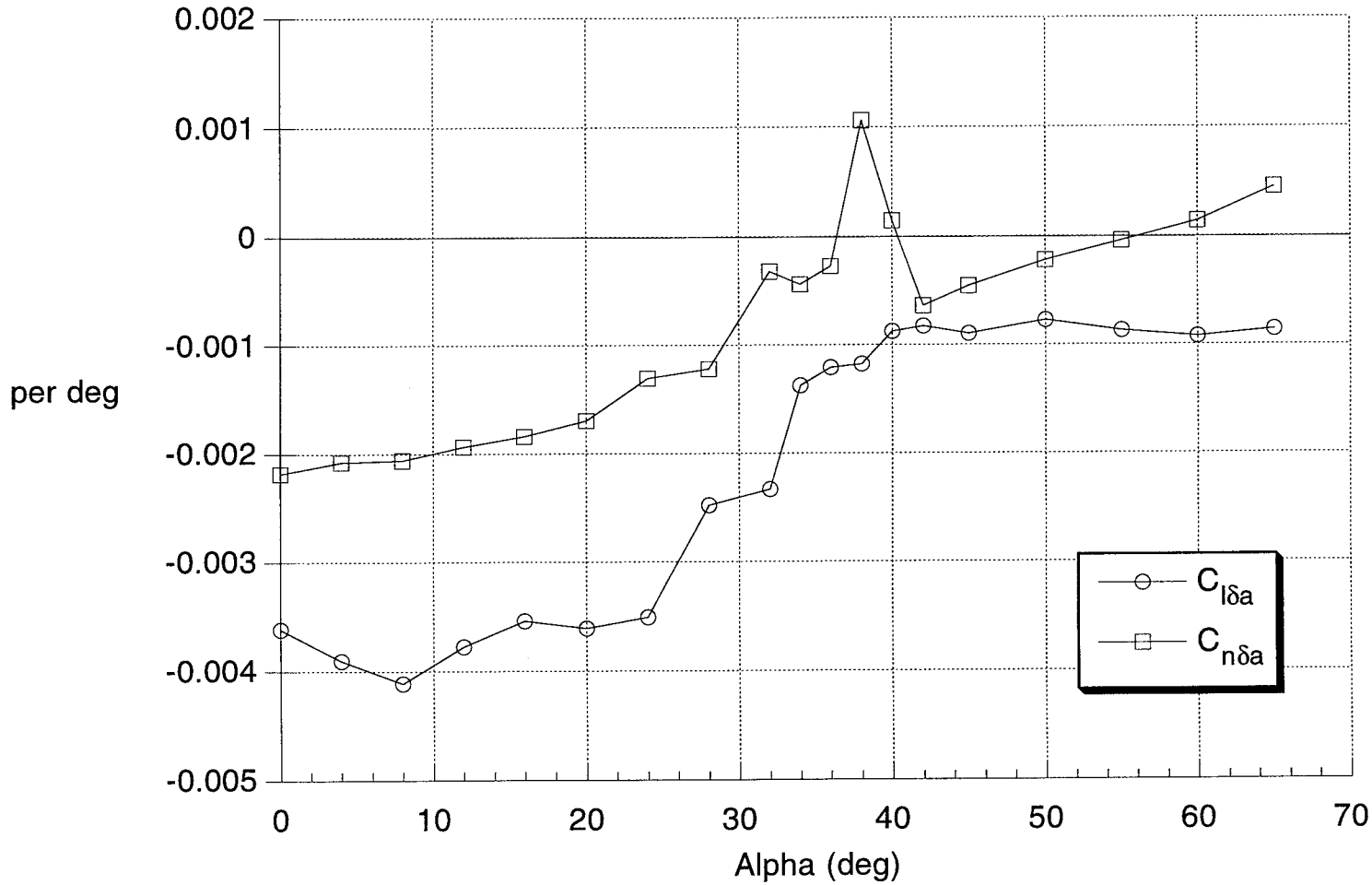

Fig. 29 Aileron Control Power for 19% Model in 30- by 60-Foot Tunnel

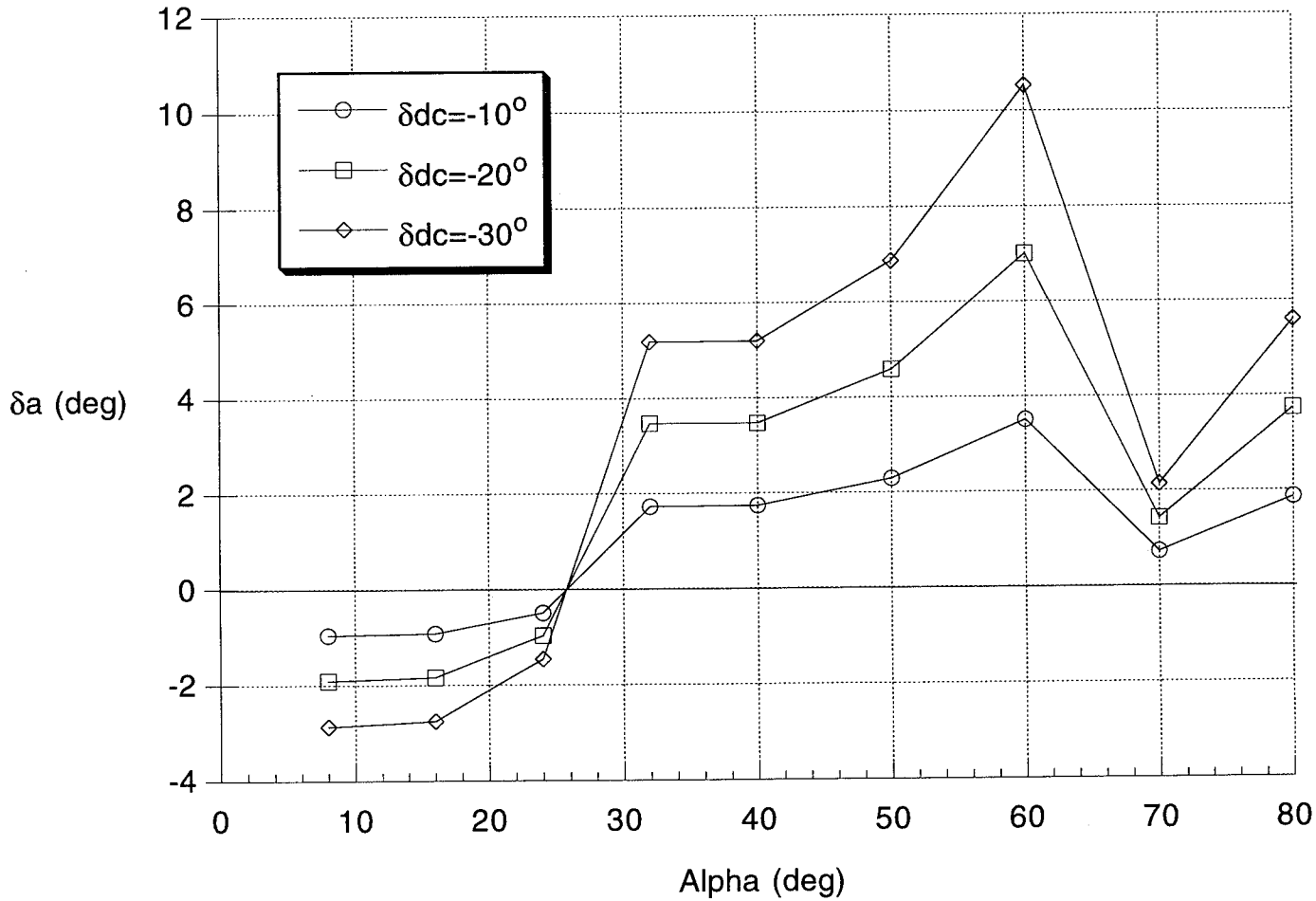

Fig. 30 Aileron Deflection to Coordinate Wind-Axis Roll with Differential Canard at 0° Sideslip

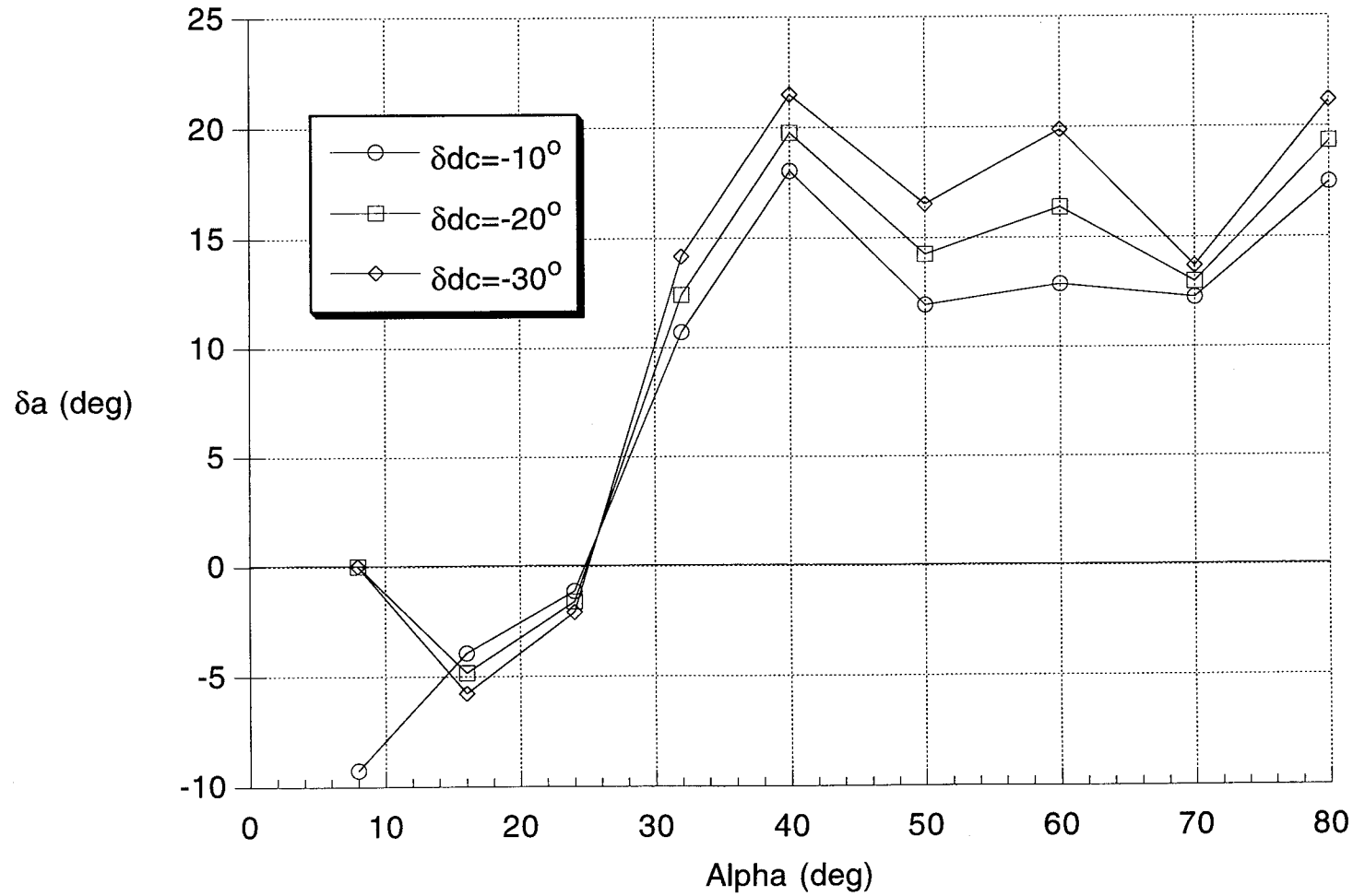

Fig. 31 Aileron Deflection to Coordinate Wind-Axis Roll with Differential Canard at -5° Sideslip

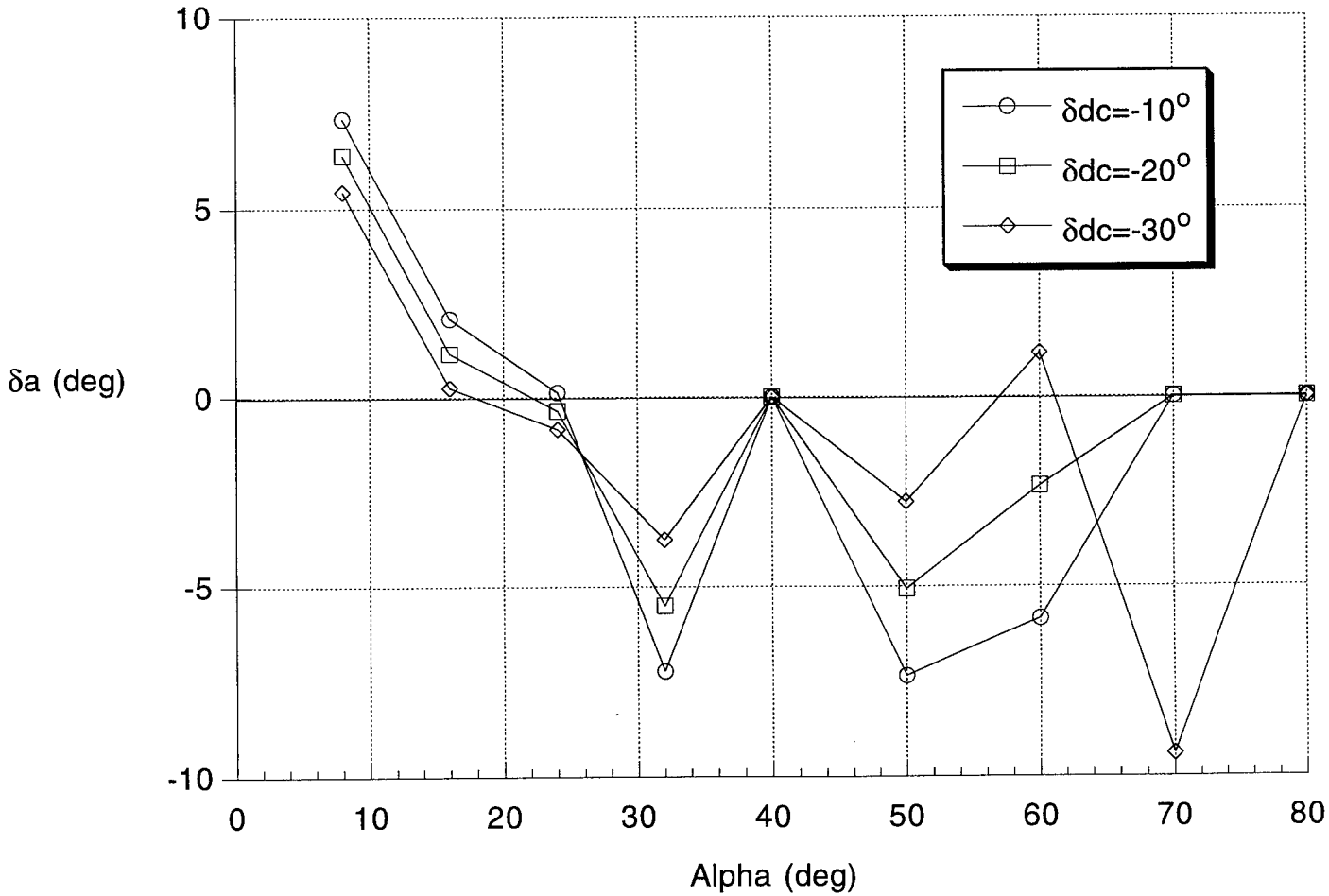

Fig. 32 Aileron Deflection to Coordinate Wind-Axis Roll with Differential Canard at 5° Sideslip

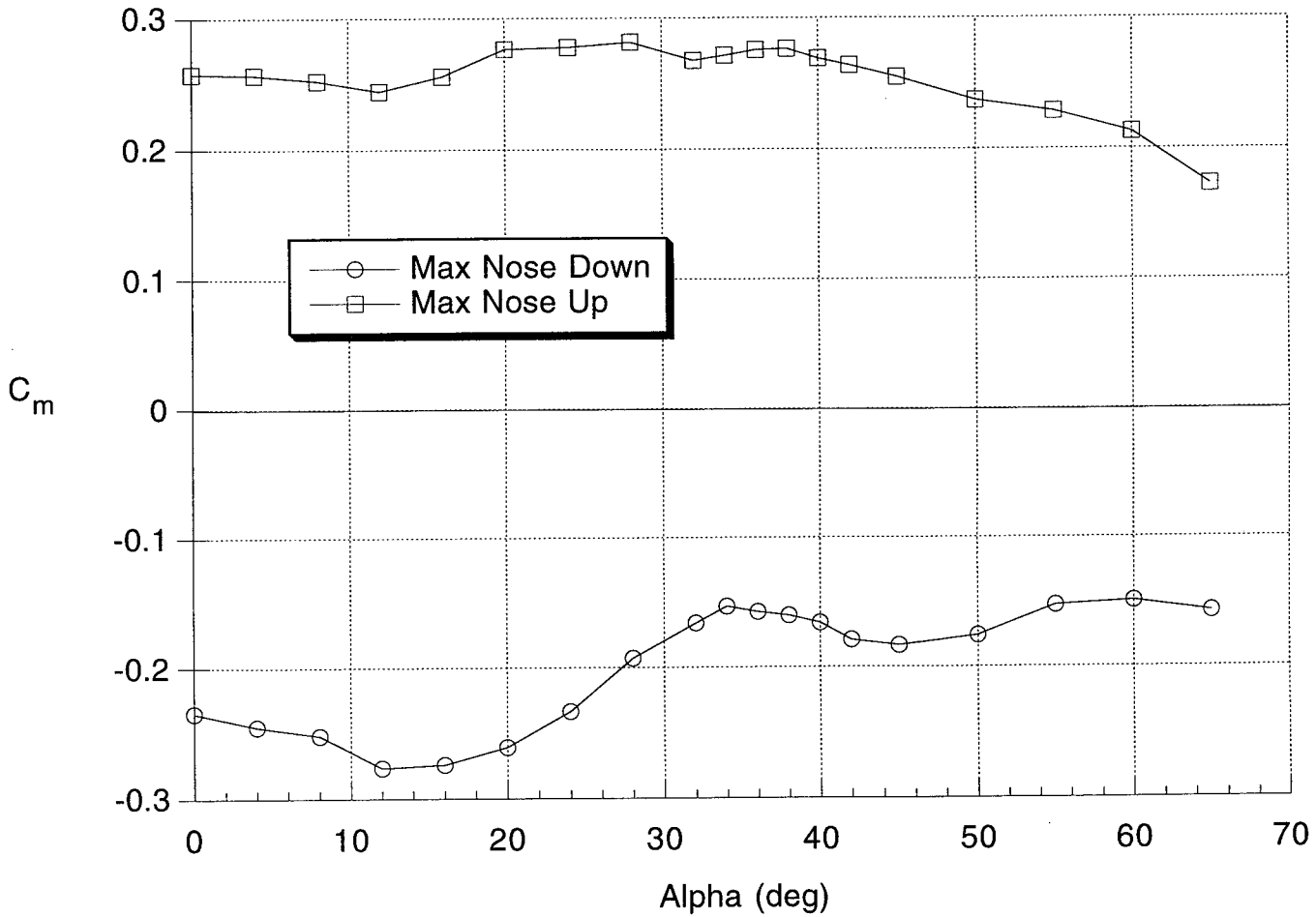

Fig. 33 Maximum Available Aerodynamic Pitching Moment for 19% Model in 30- by 60-Foot Tunnel

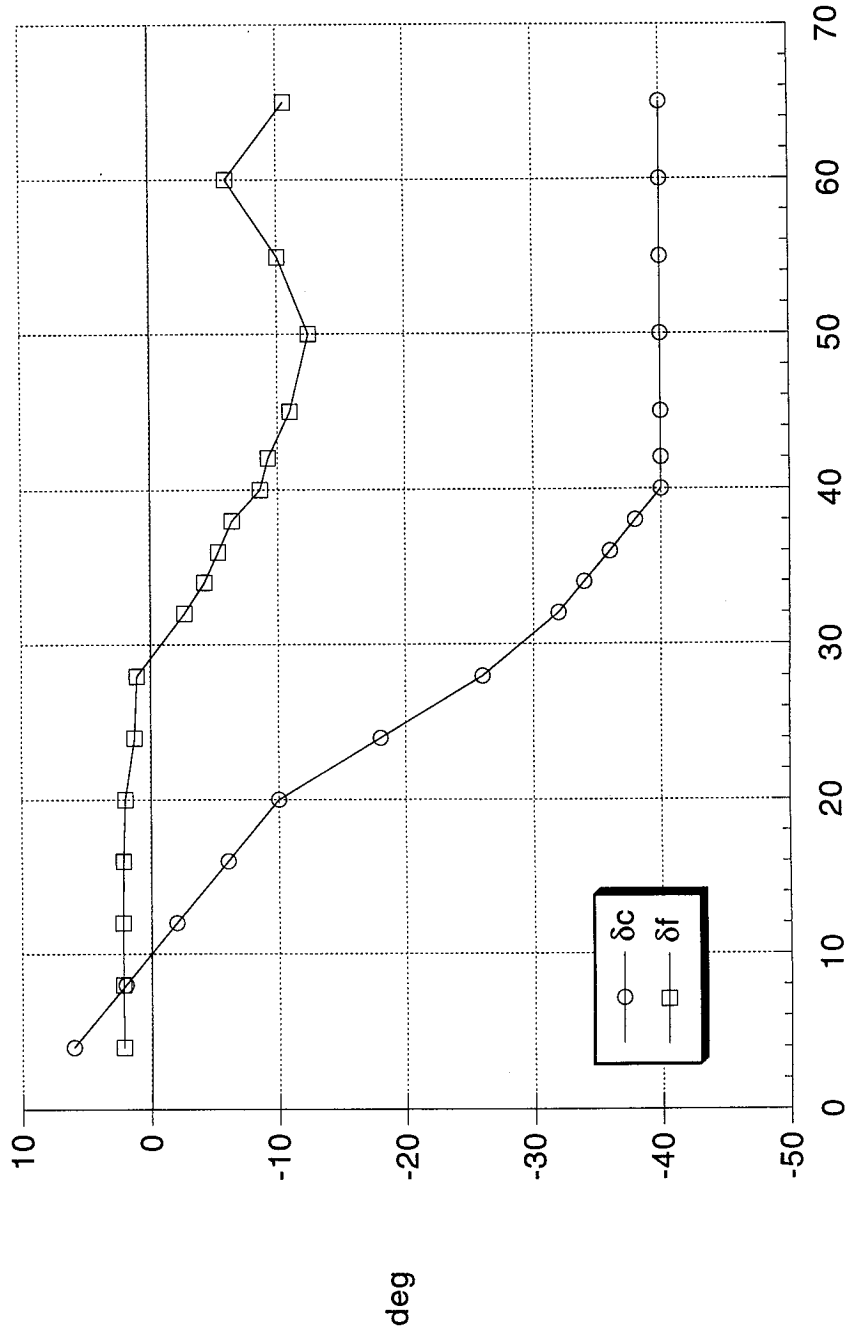

Fig. 34 Control Deflections Used to Trim Model

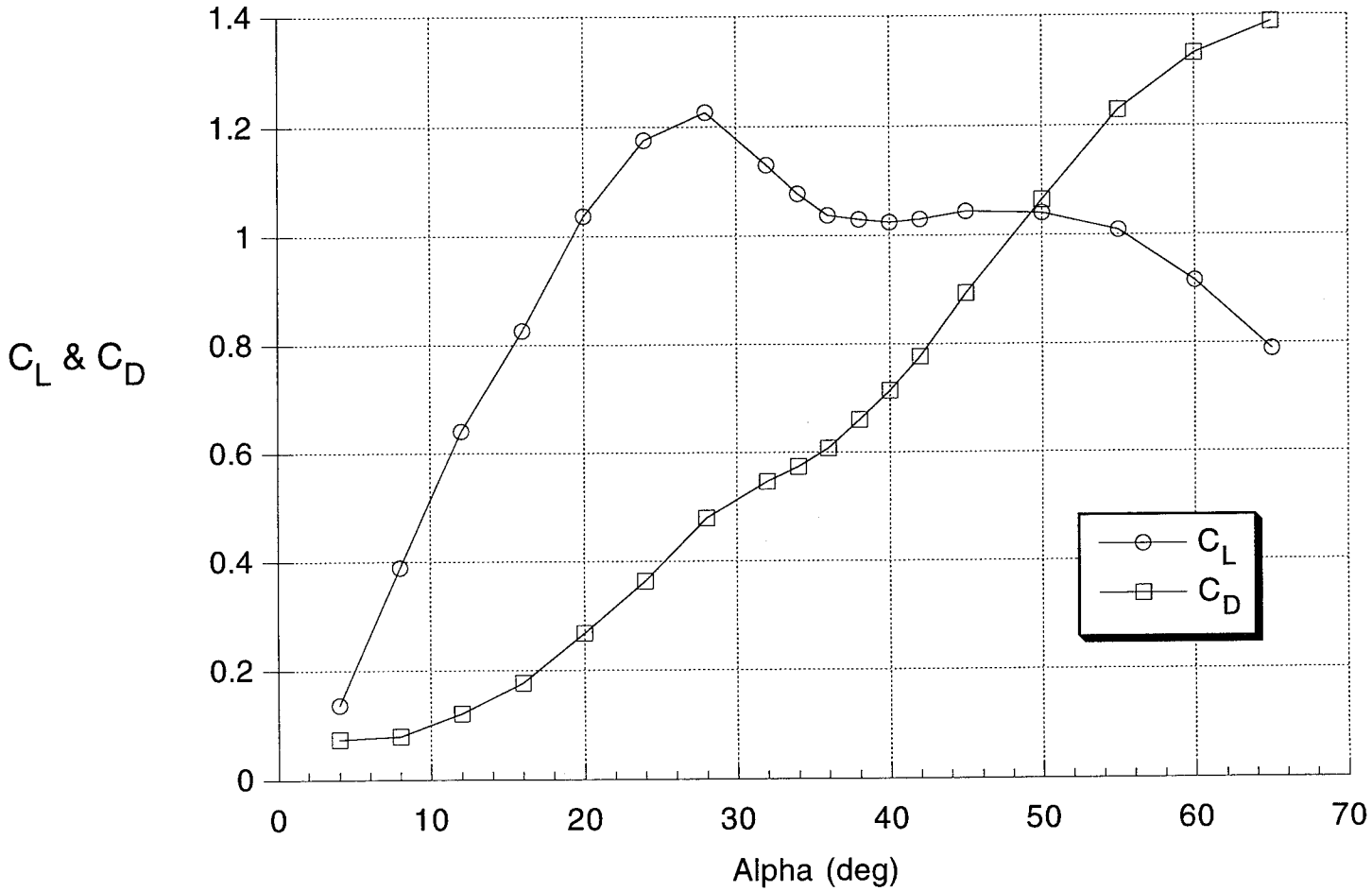

Fig. 35 Trim Lift and Drag Estimates

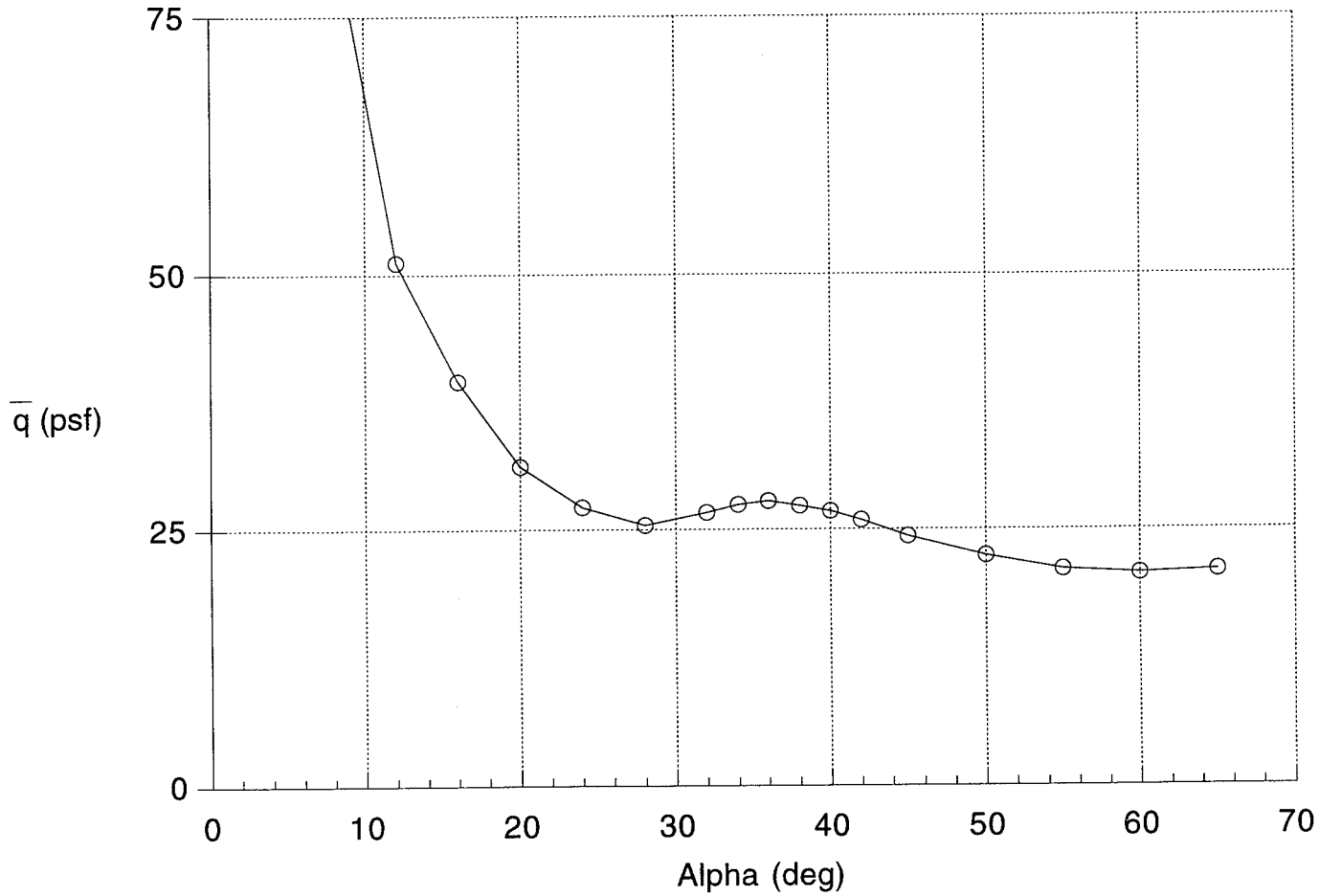

Fig. 36 Dynamic Pressure to Trim 550 lb Drop Model

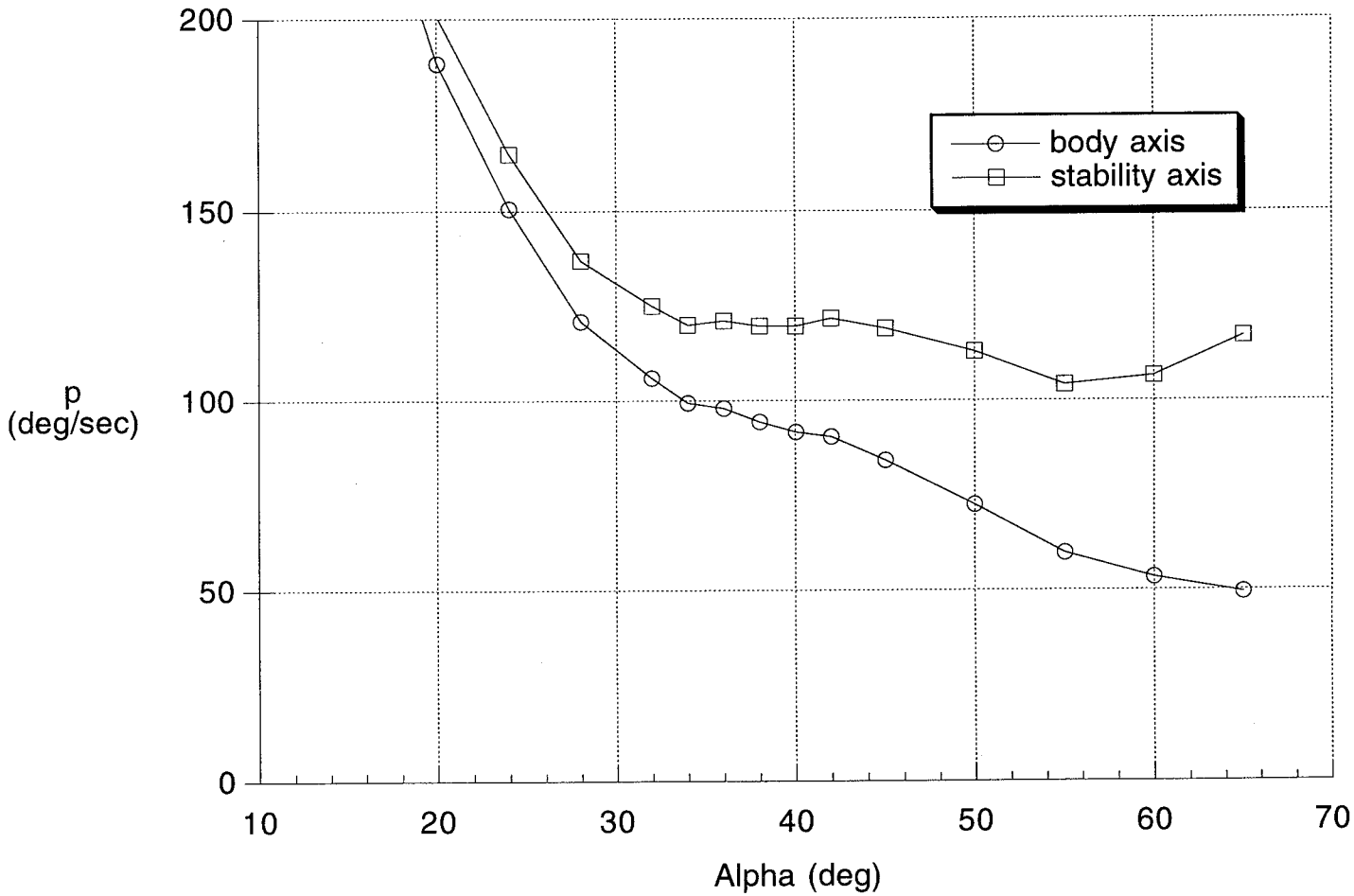

Fig. 37 Maximum Roll Rate Before Inertial Coupling

Saturates Pitch Controls

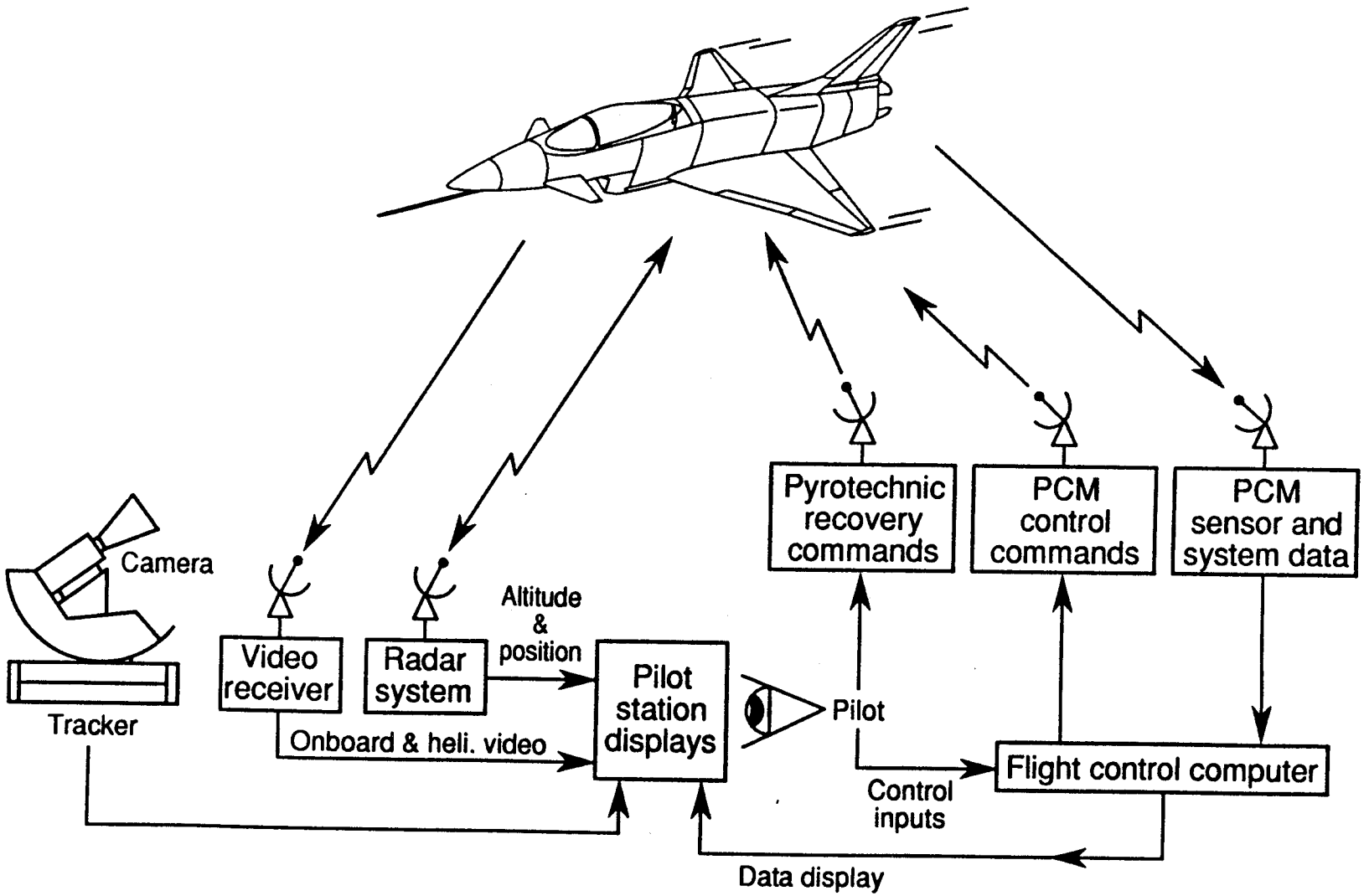

Fig. 38 Drop Model Test Procedure

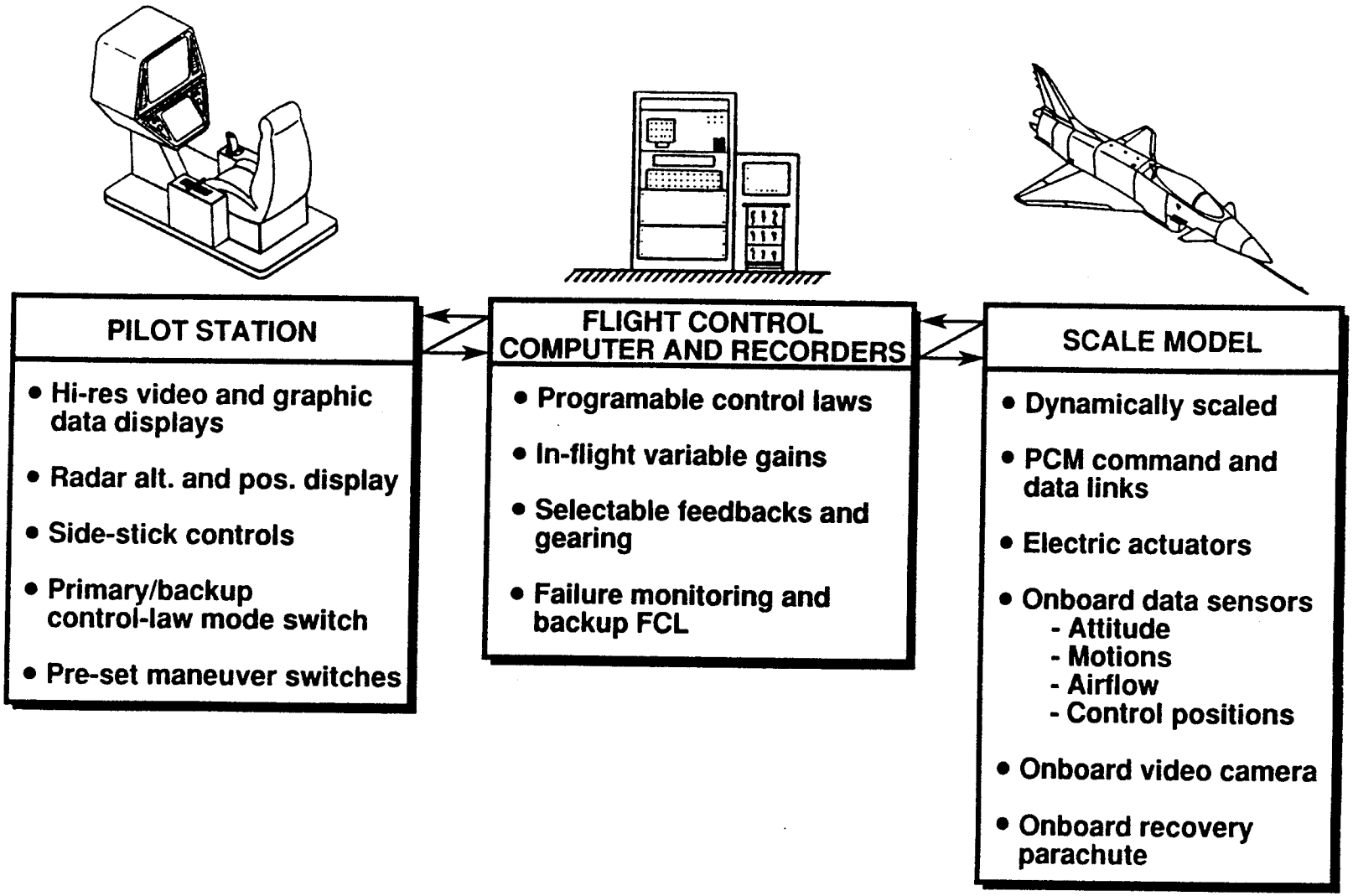

Fig. 39 Drop Model Flight Command System

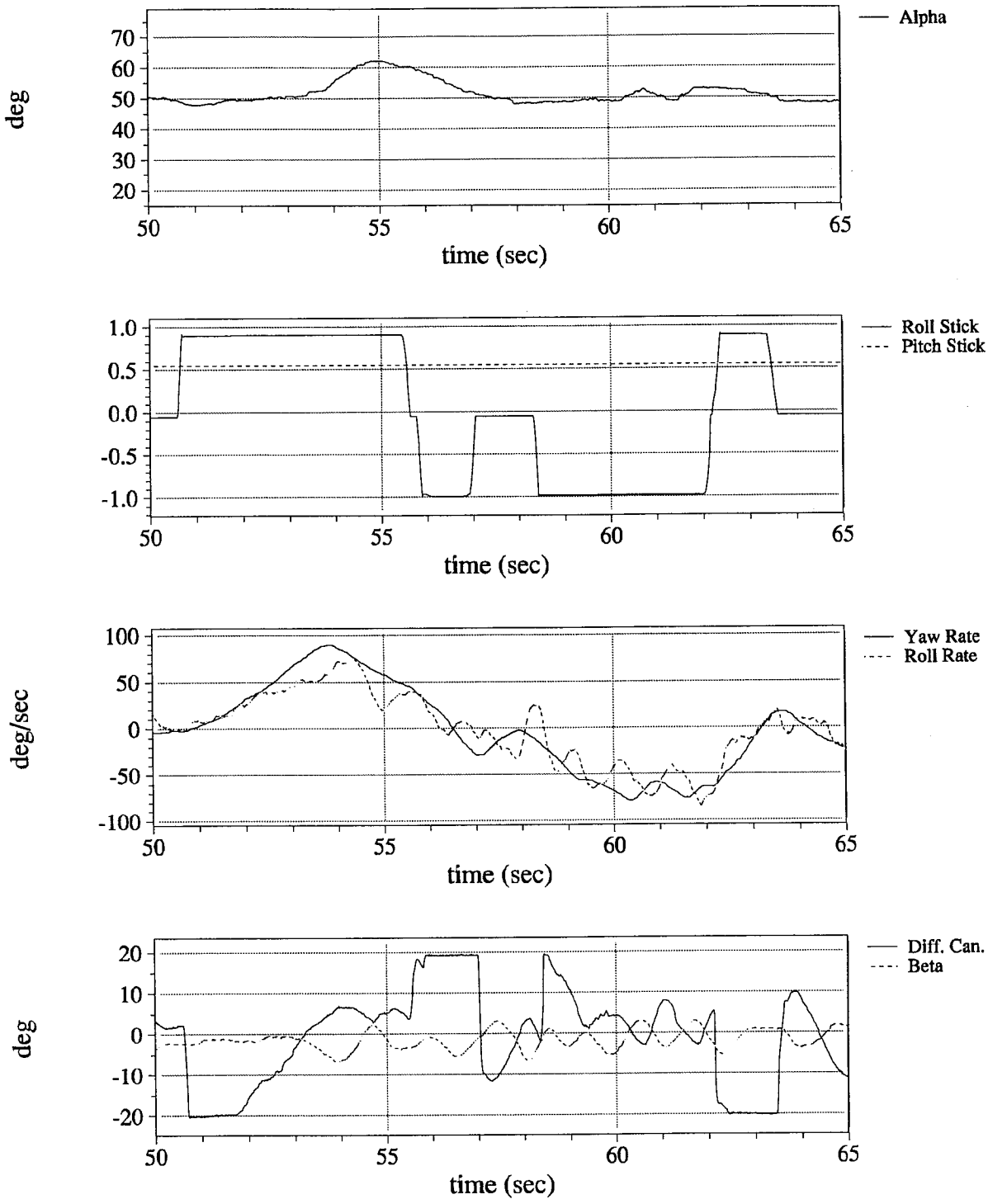

Fig. 40 Drop Model: Right and Left Rolls at $\alpha = 50°$

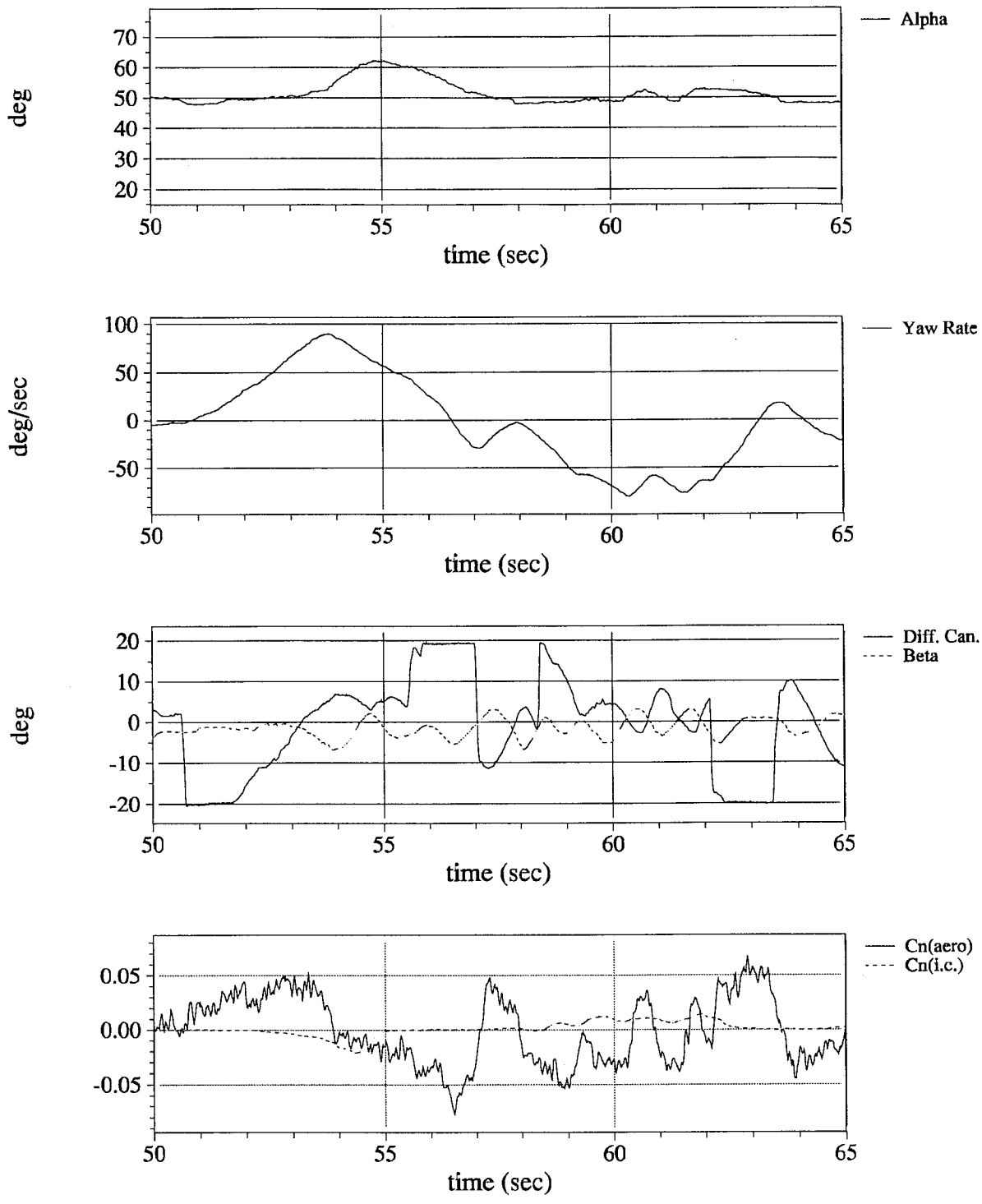

Fig. 41 Drop Model: Right and Left Rolls at $\alpha = 50°$, Directional Axis

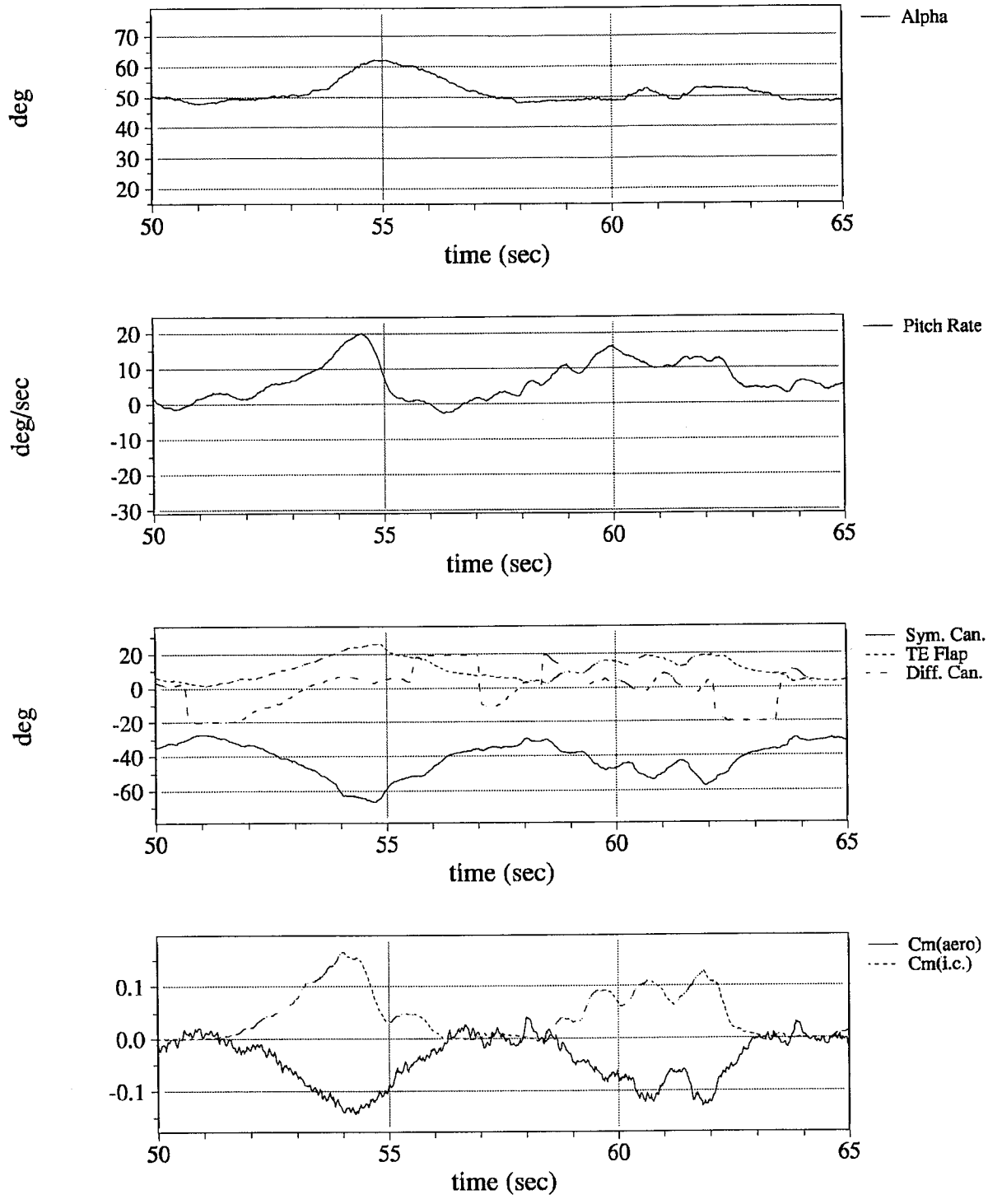

Fig. 42 Drop Model: Right and Left Rolls at $\alpha = 50°$, Pitch Axis

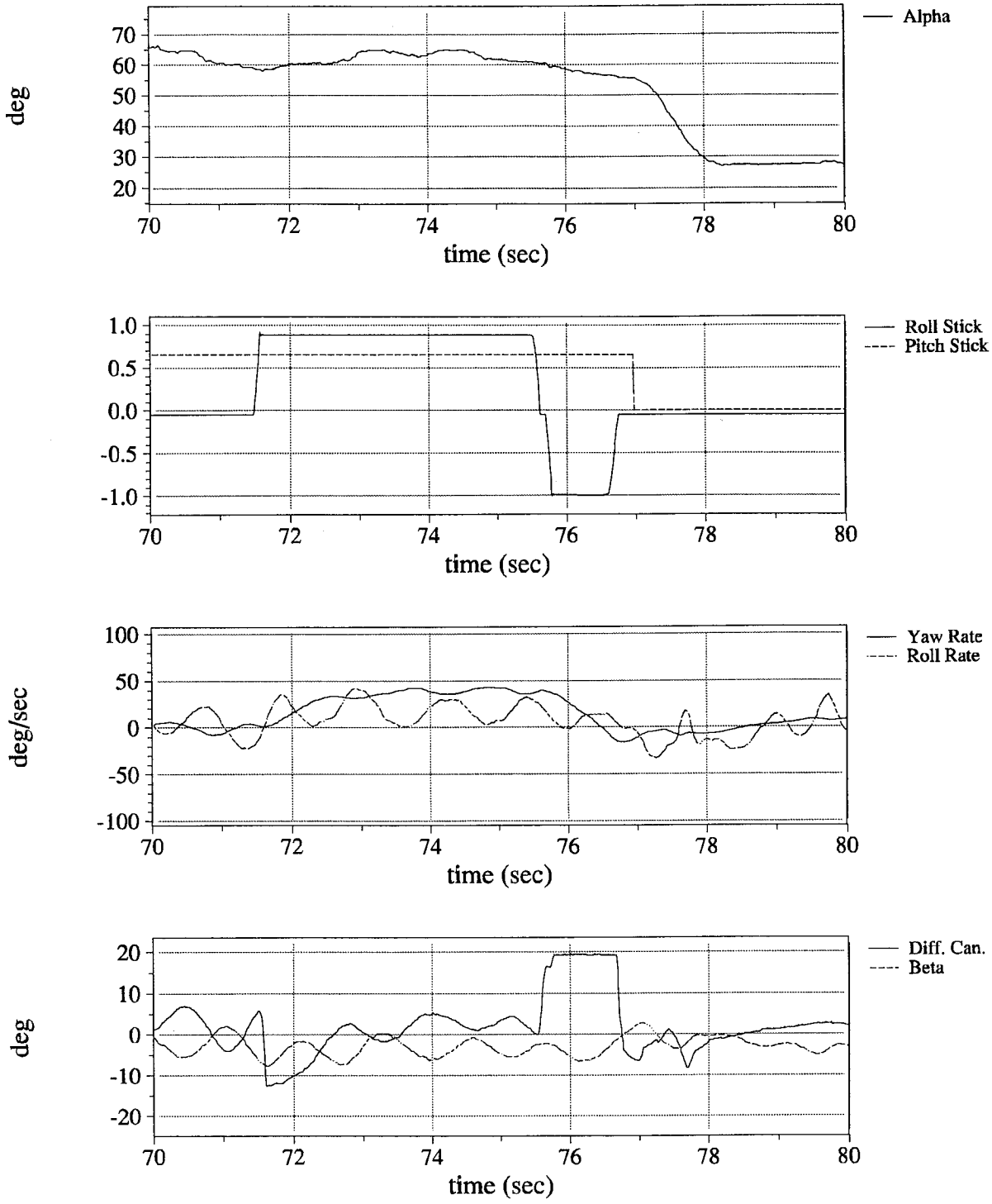

Fig. 43 Drop Model: Right Roll at $\alpha = 60°$

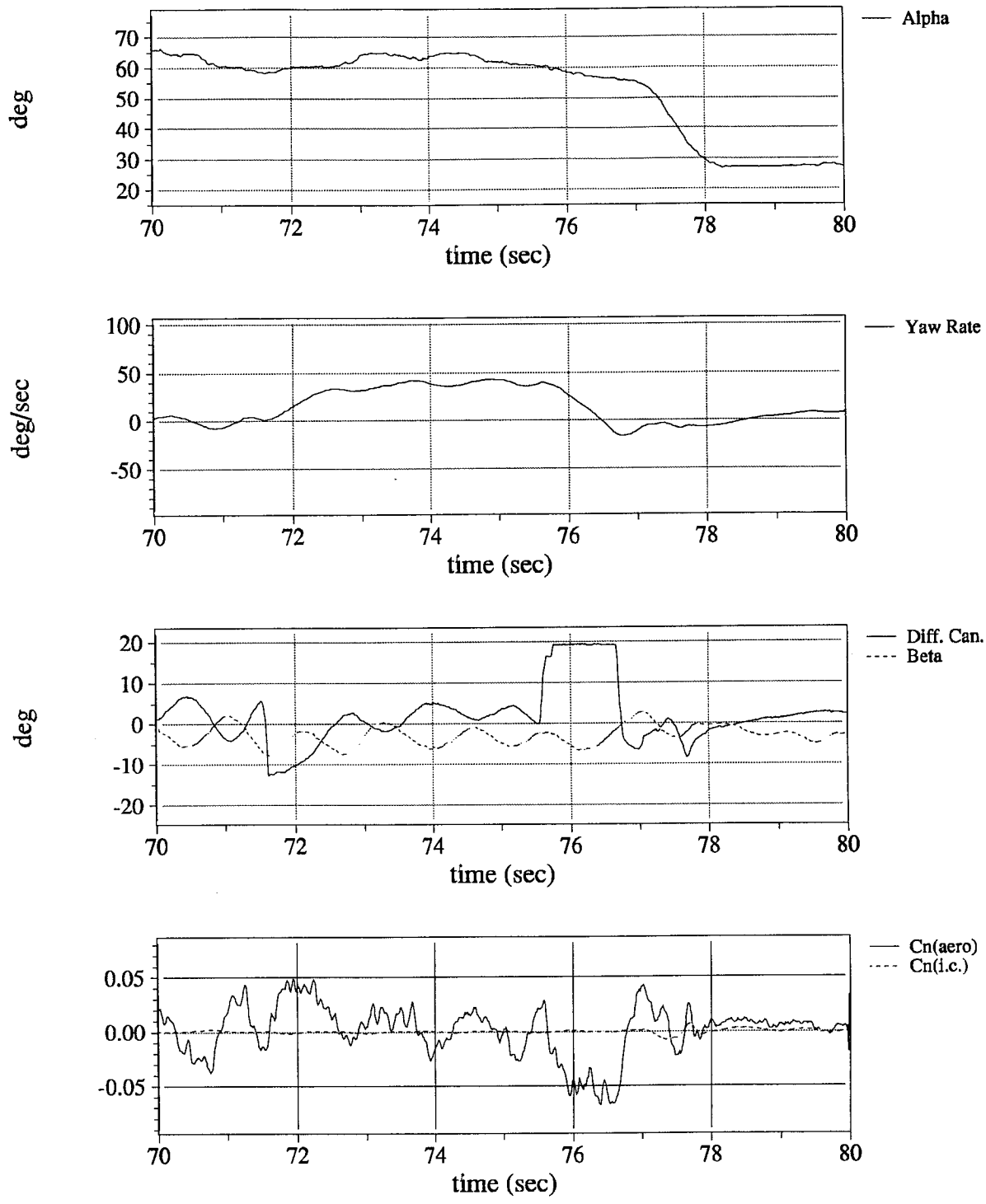

Fig. 44 Drop Model: Right Roll at $\alpha = 60°$, Directional Axis

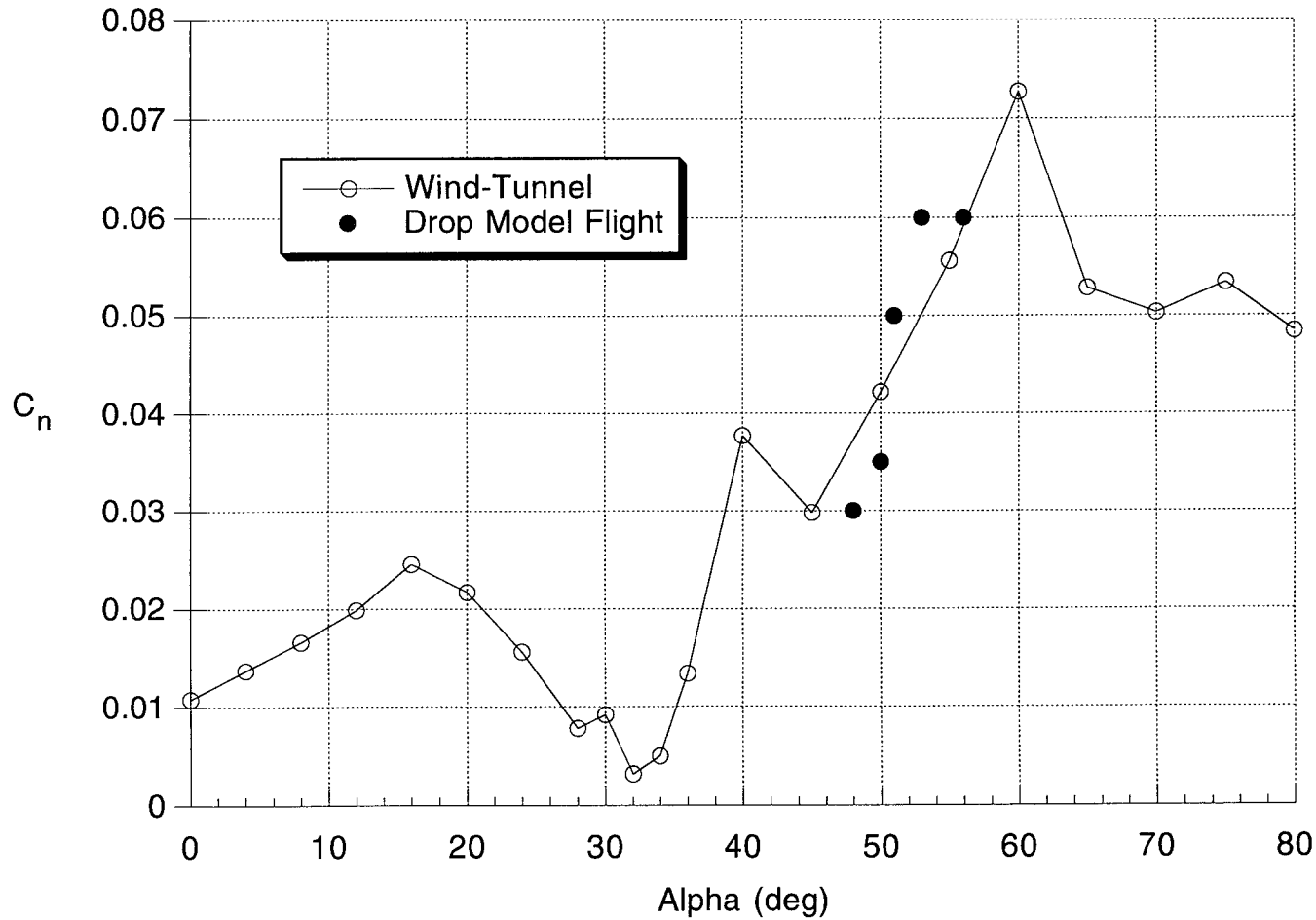

Fig. 45 Comparison of Wind-Tunnel Data and

Drop Model Flight Test Results

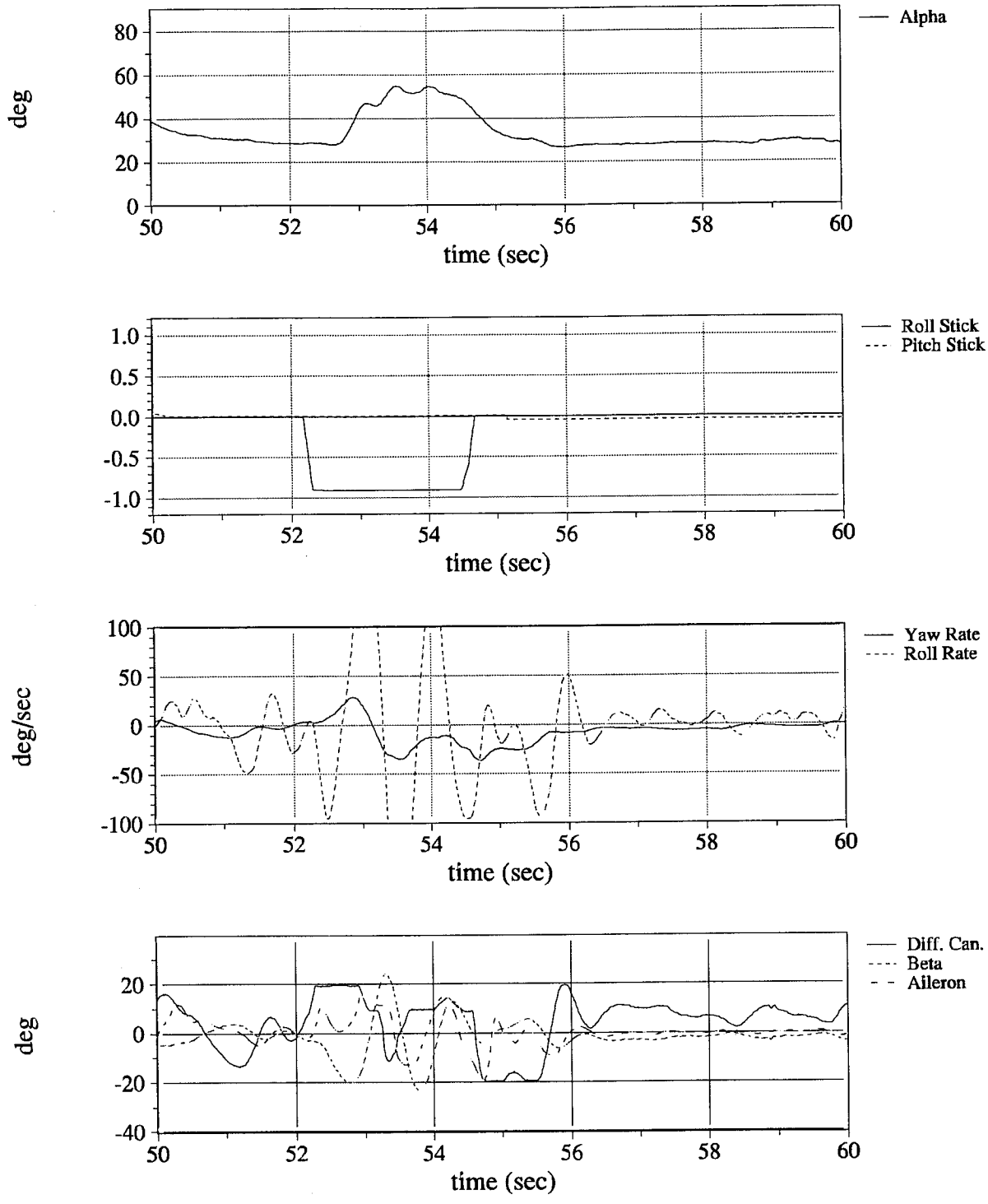

Fig. 46 Tailless Drop Model: Departure at $\alpha = 30°$

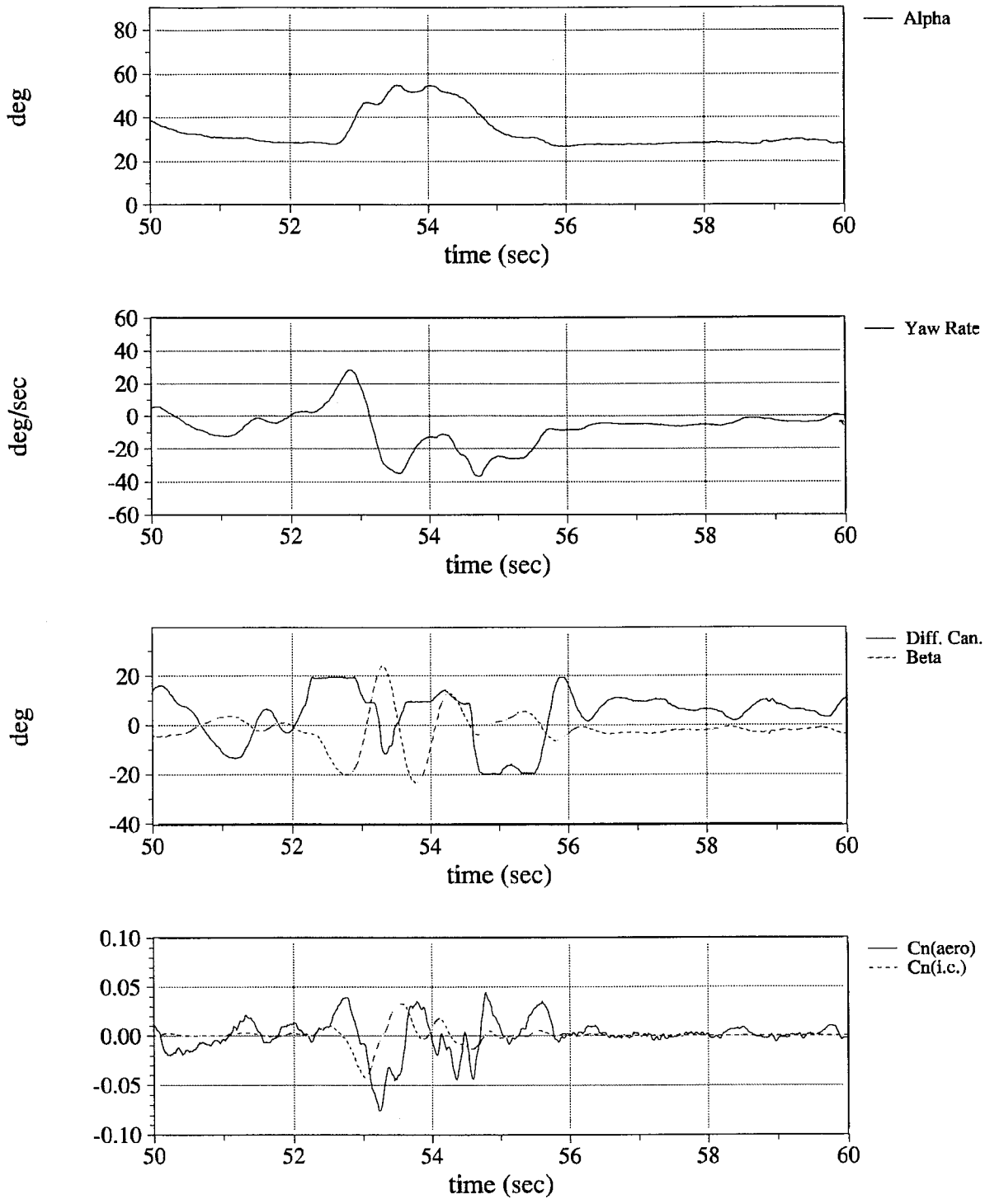

Fig. 47 Tailless Drop Model: Departure at $\alpha = 30°$, Directional Axis

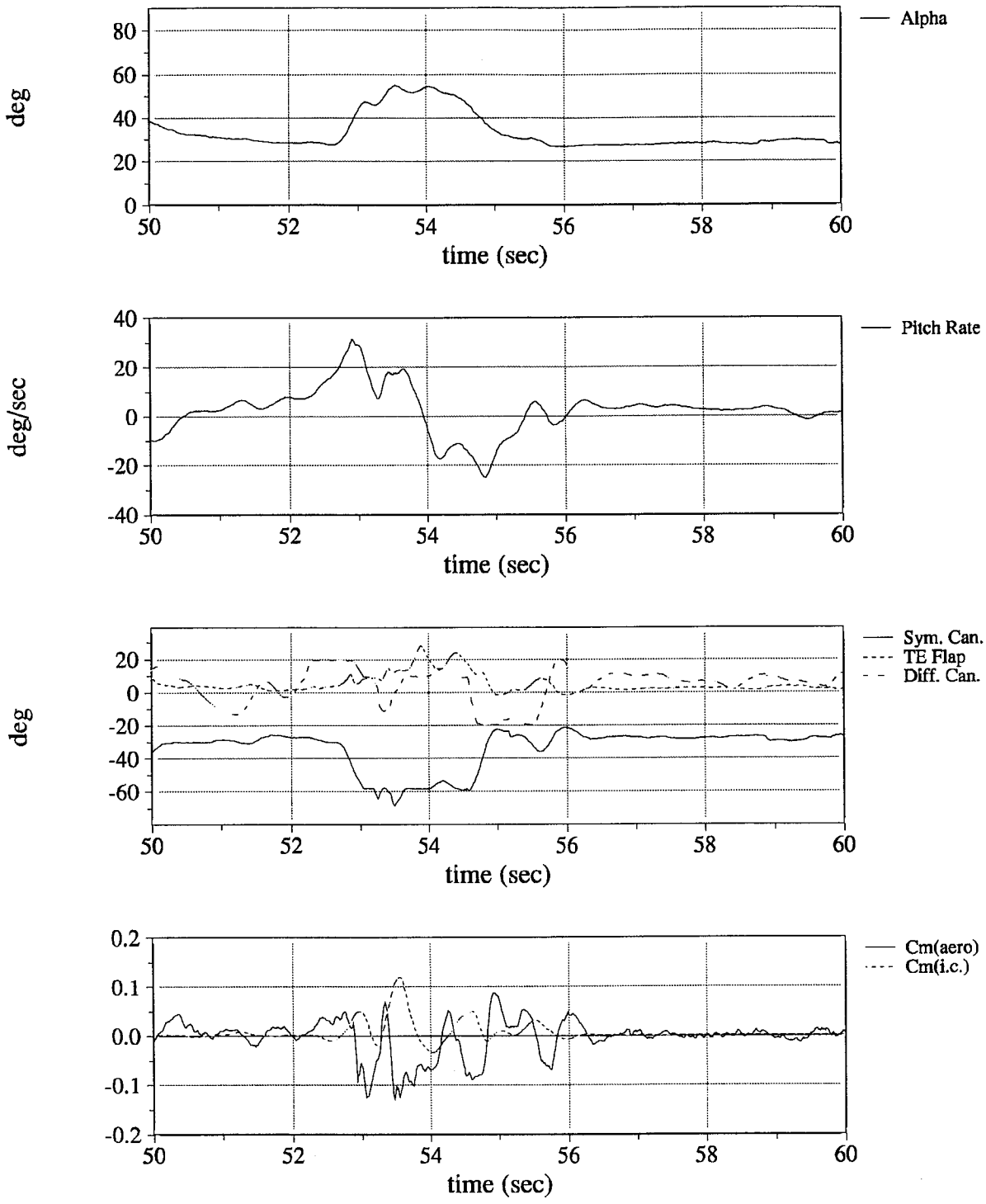

Fig. 48 Tailless Drop Model: Departure at $\alpha = 30°$, Pitch Axis

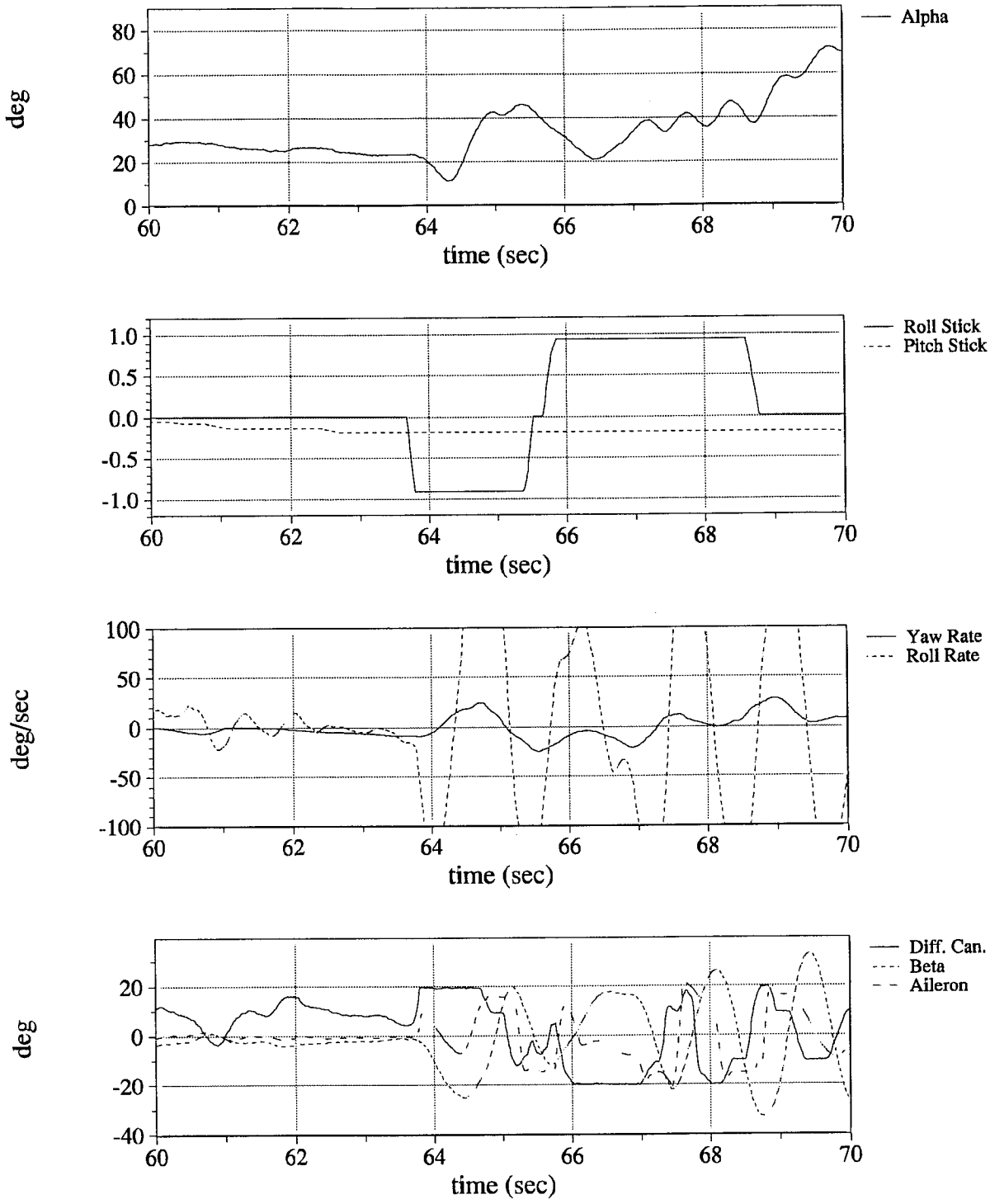

Fig. 49 Tailless Drop Model: Departure at $\alpha = 20°$

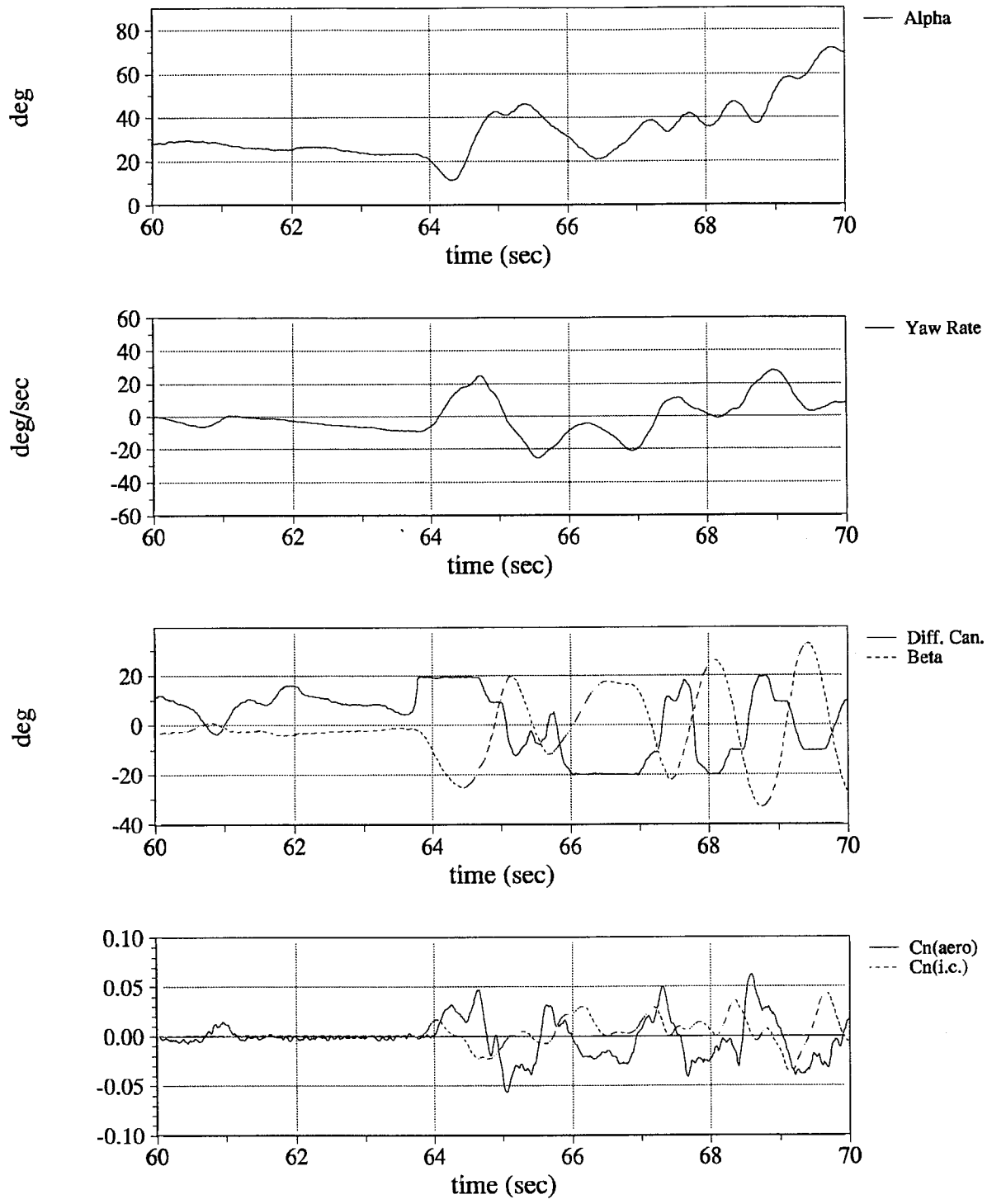

Fig. 50 Tailless Drop Model: Departure at $\alpha = 20°$, Directional Axis

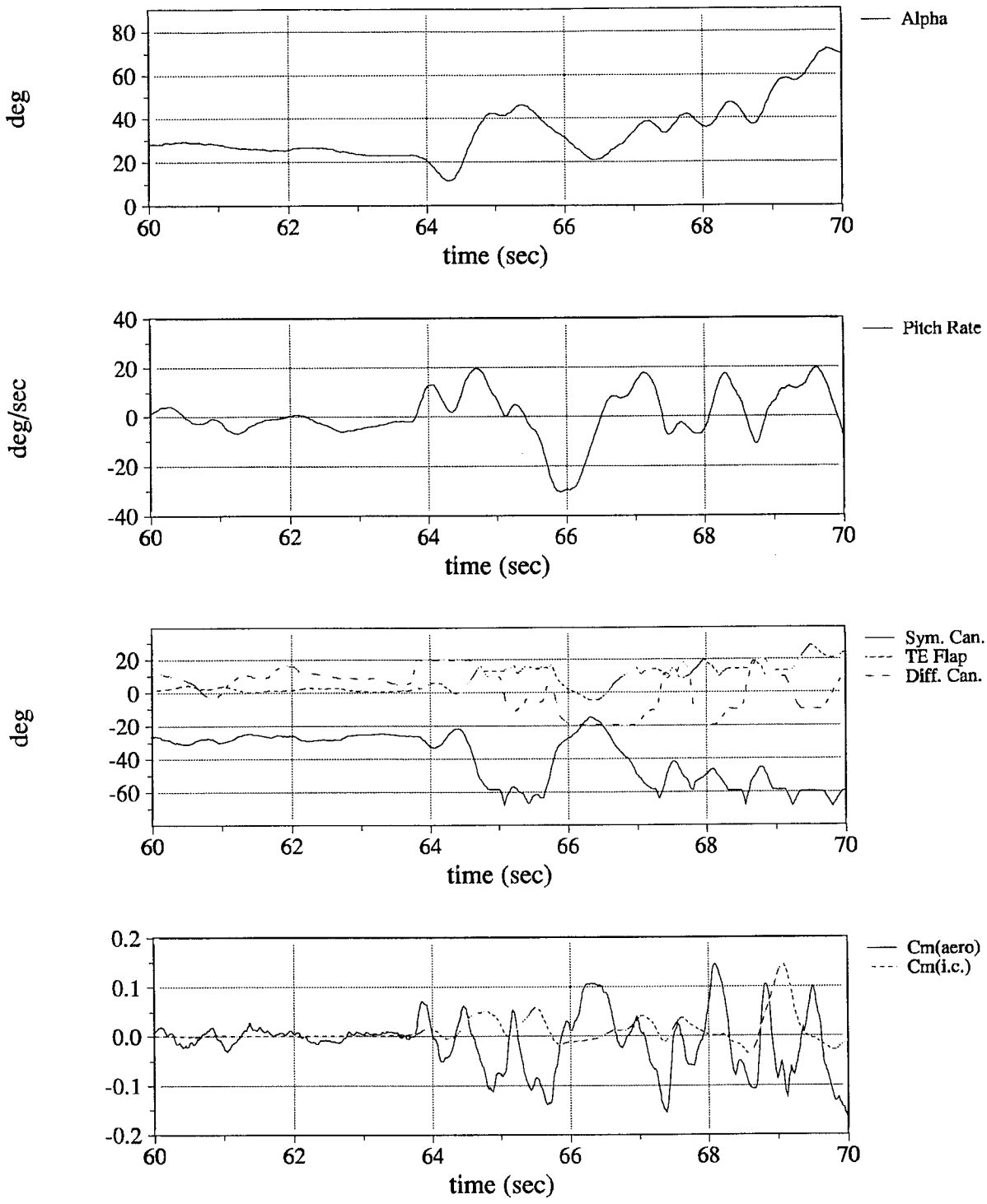

Fig. 51 Tailless Drop Model: Departure at $\alpha = 20°$, Pitch Axis

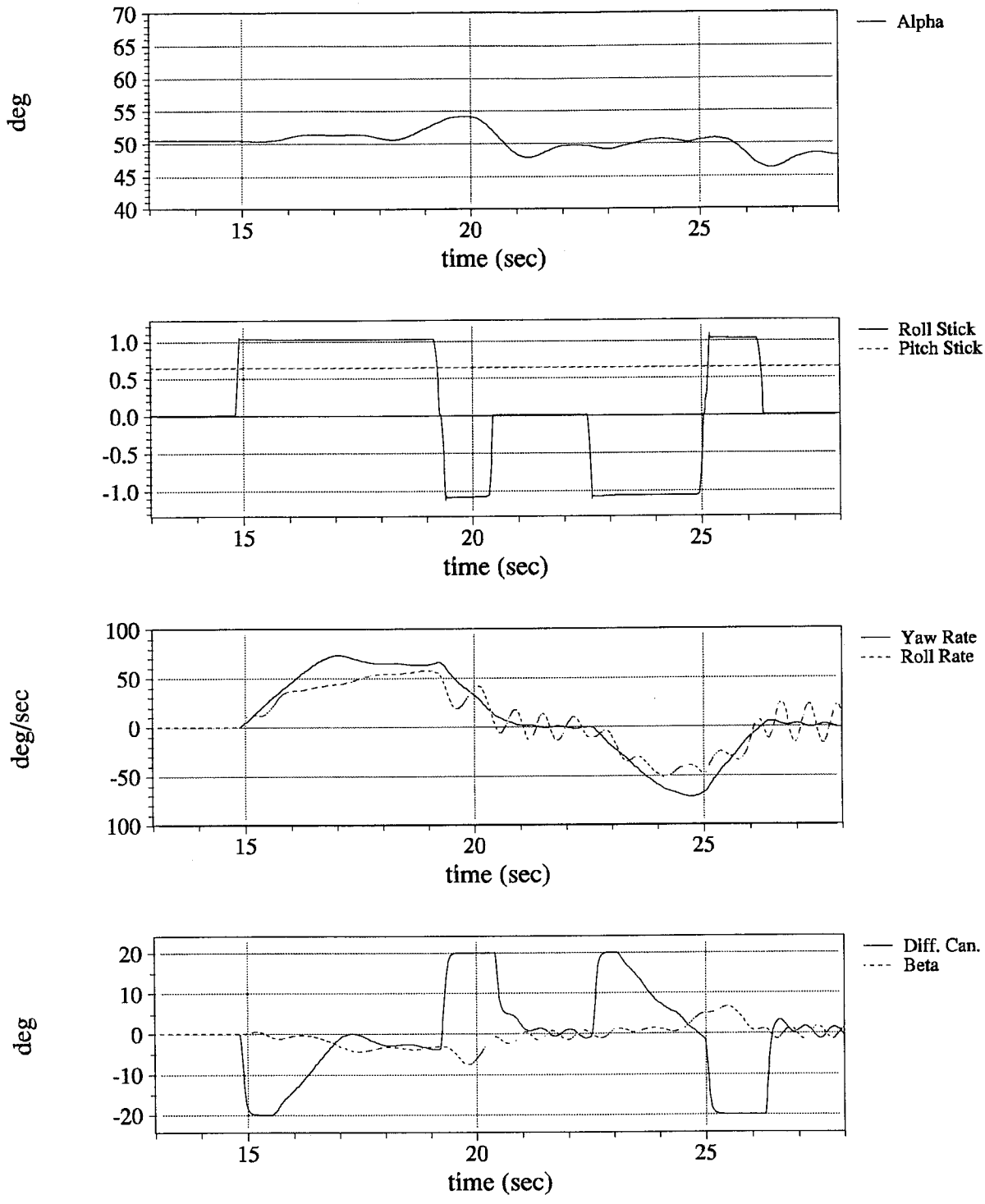

Fig. 52 Drop Model Simulation: Right and Left Rolls at $\alpha = 50°$

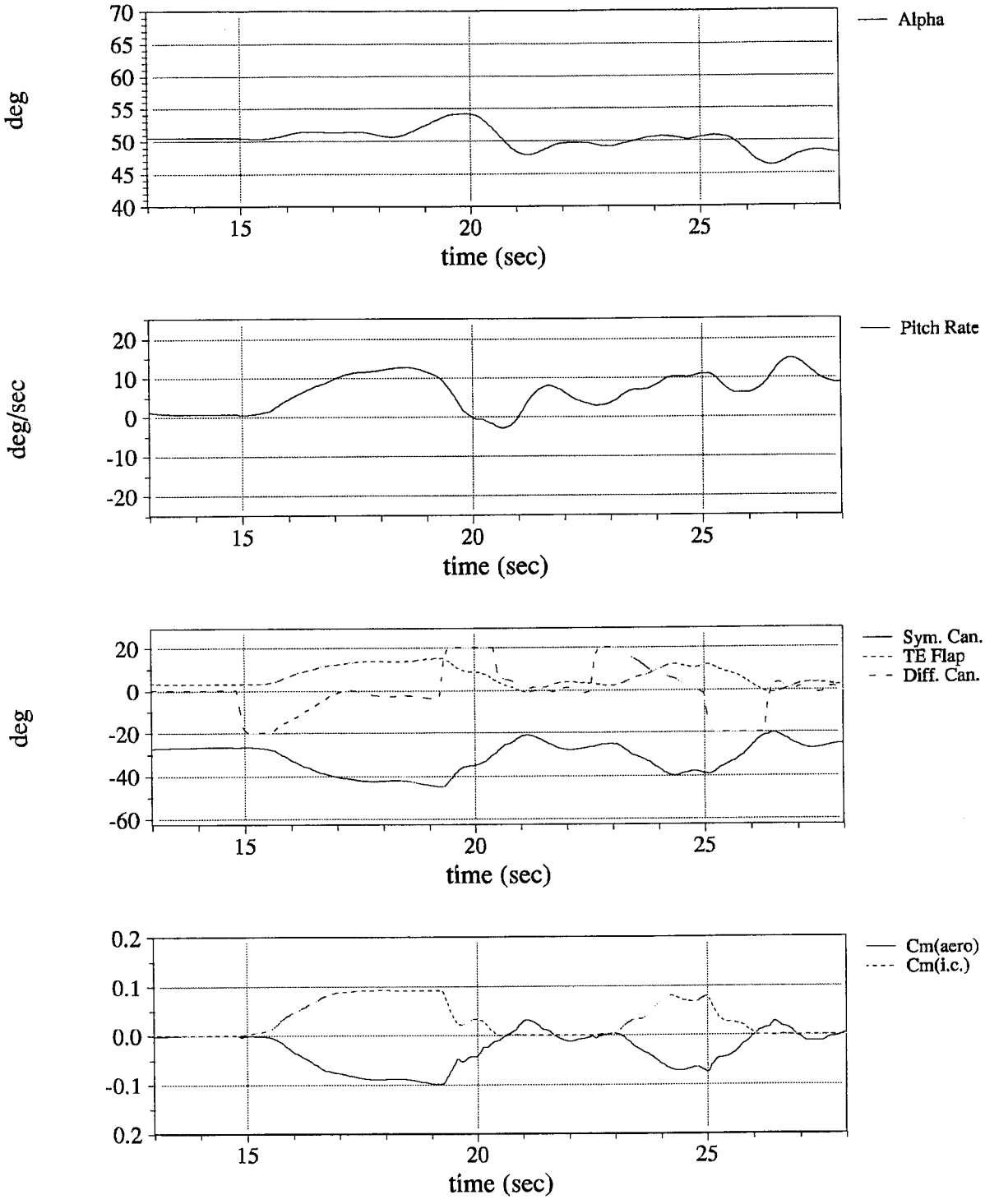

Fig. 53 Drop Model Simulation: Right and Left Rolls at $\alpha = 50°$, Pitch Axis

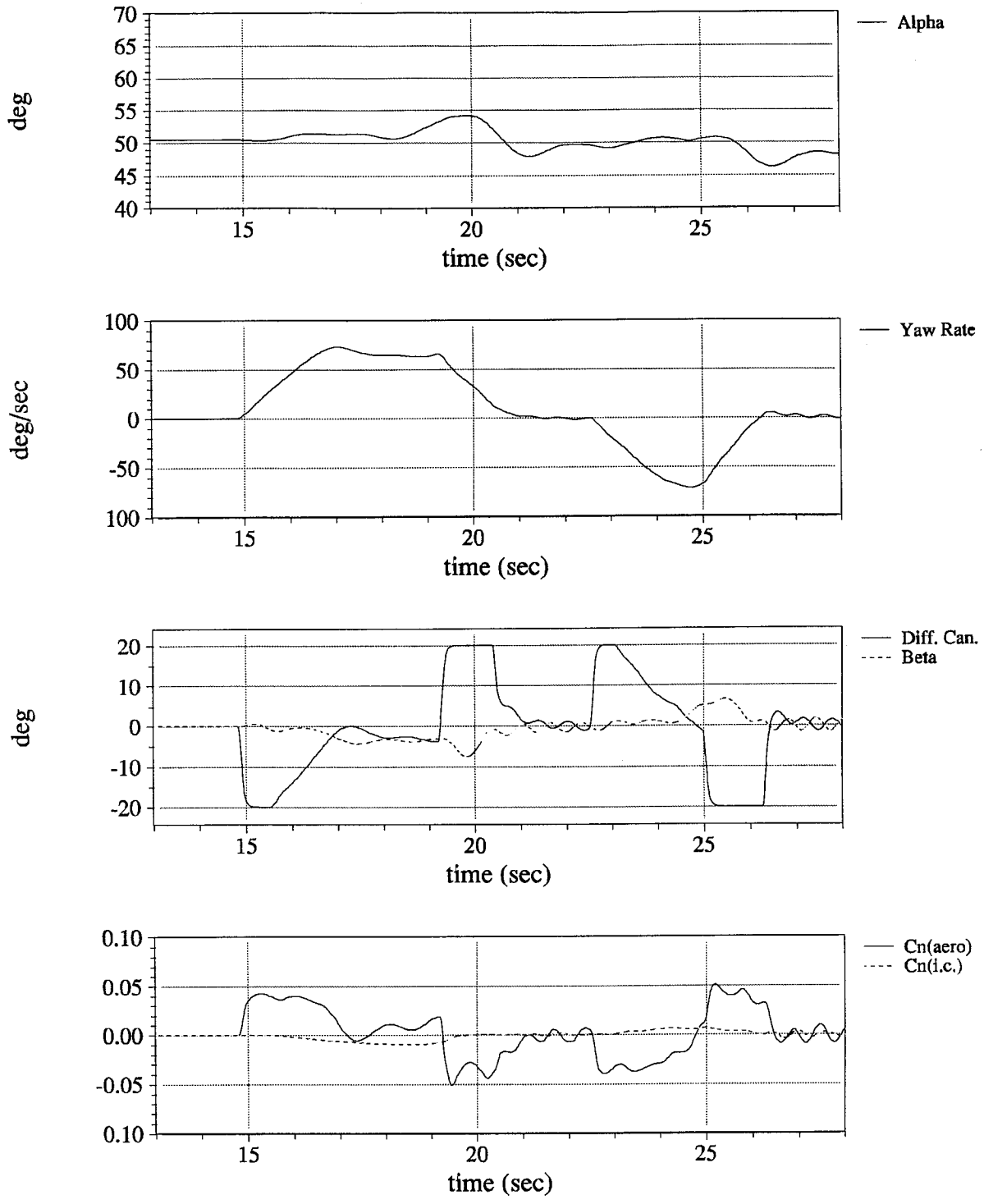

Fig. 54 Drop Model Simulation: Right and Left Rolls at $\alpha = 50°$,

Directional Axis

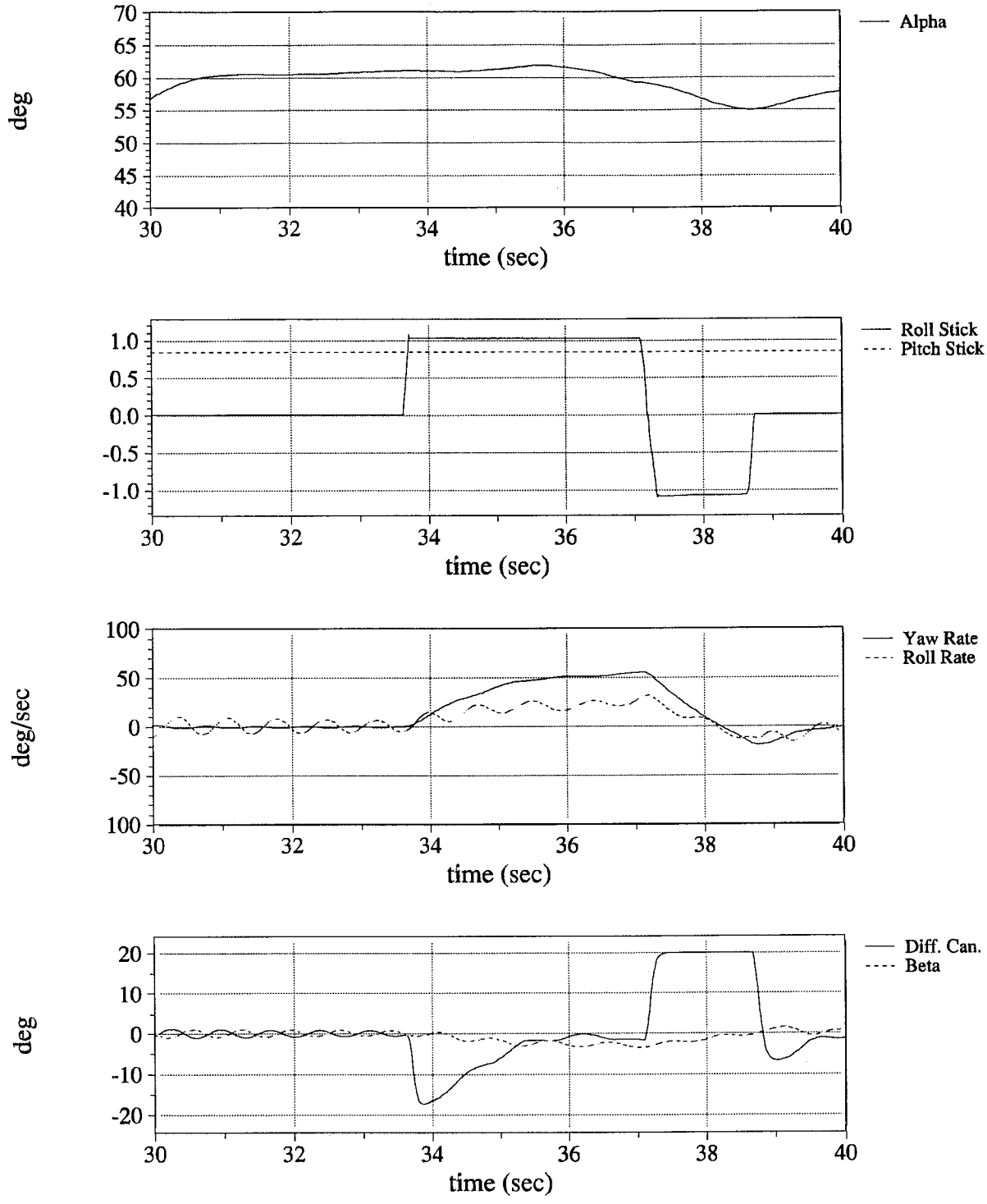

Fig. 55 Drop Model Simulation: Right Roll at $\alpha = 60°$

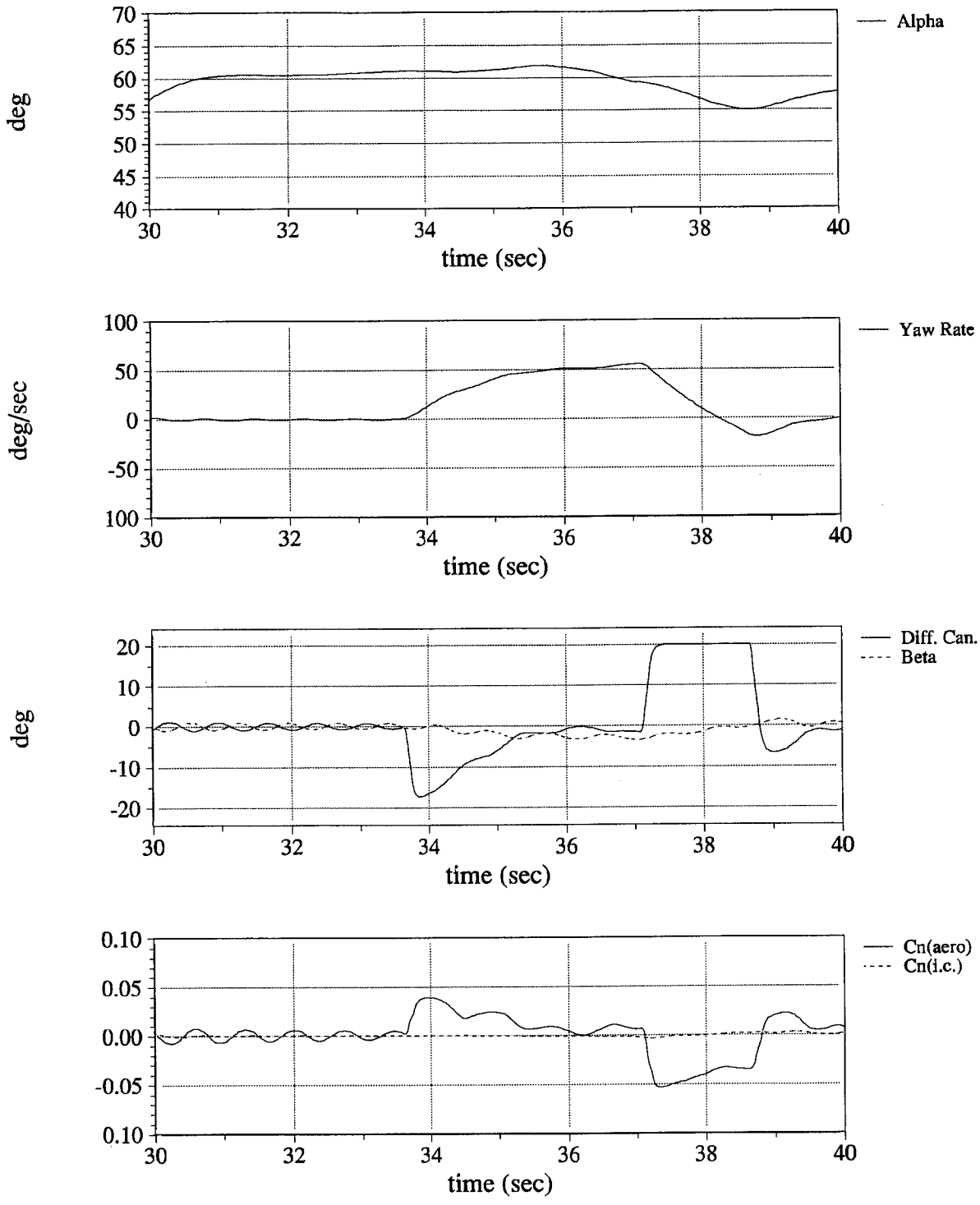

Fig. 56 Drop Model Simulation: Right Roll at $\alpha = 60°$, Directional Axis

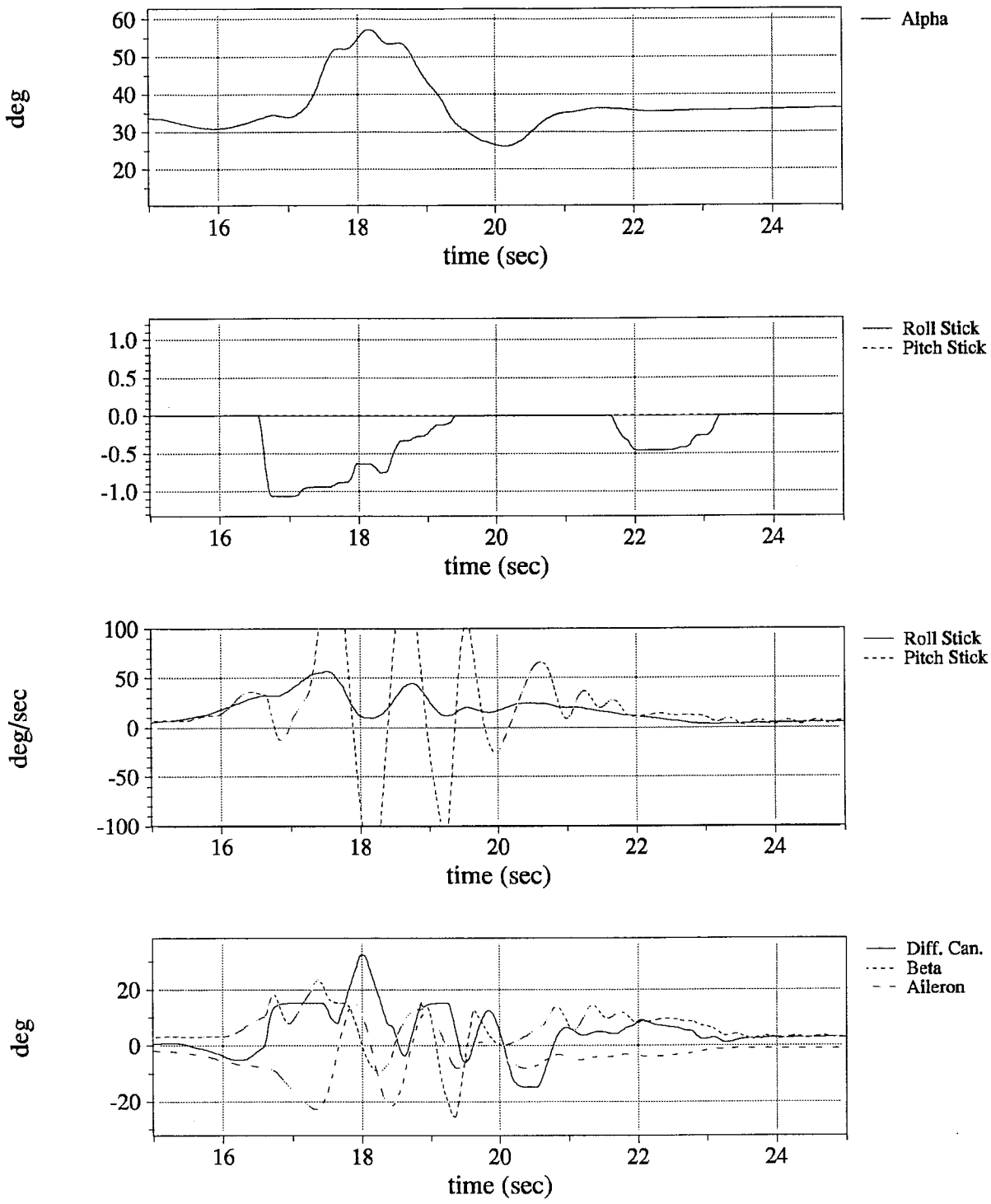

Fig. 57 Drop Model Simulation: Departure at $\alpha = 30°$

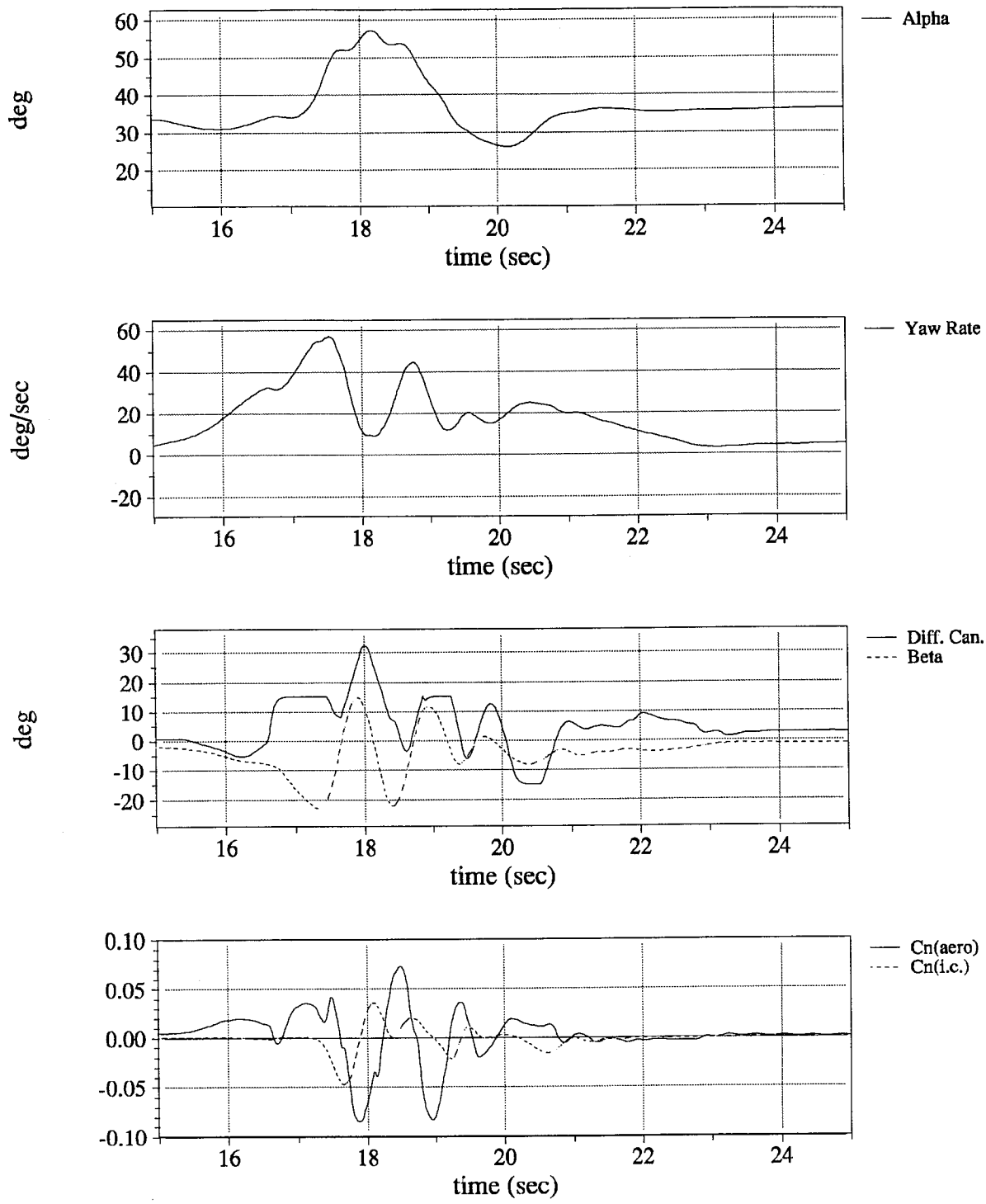

Fig. 58 Drop Model Simulation: Departure at $\alpha = 30°$, Directional Axis

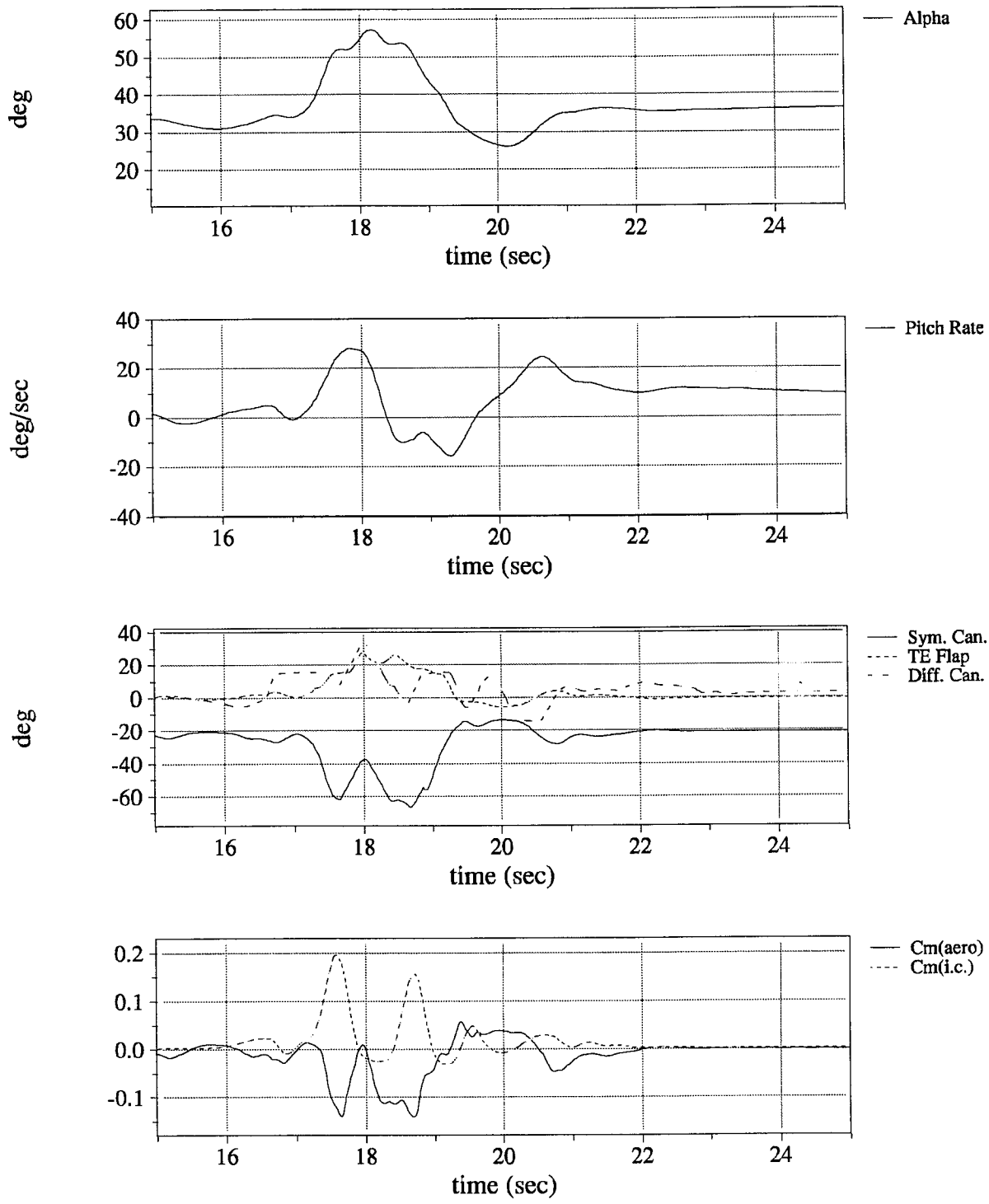

Fig. 59 Drop Model Simulation: Departure at $\alpha = 30°$, Pitch Axis

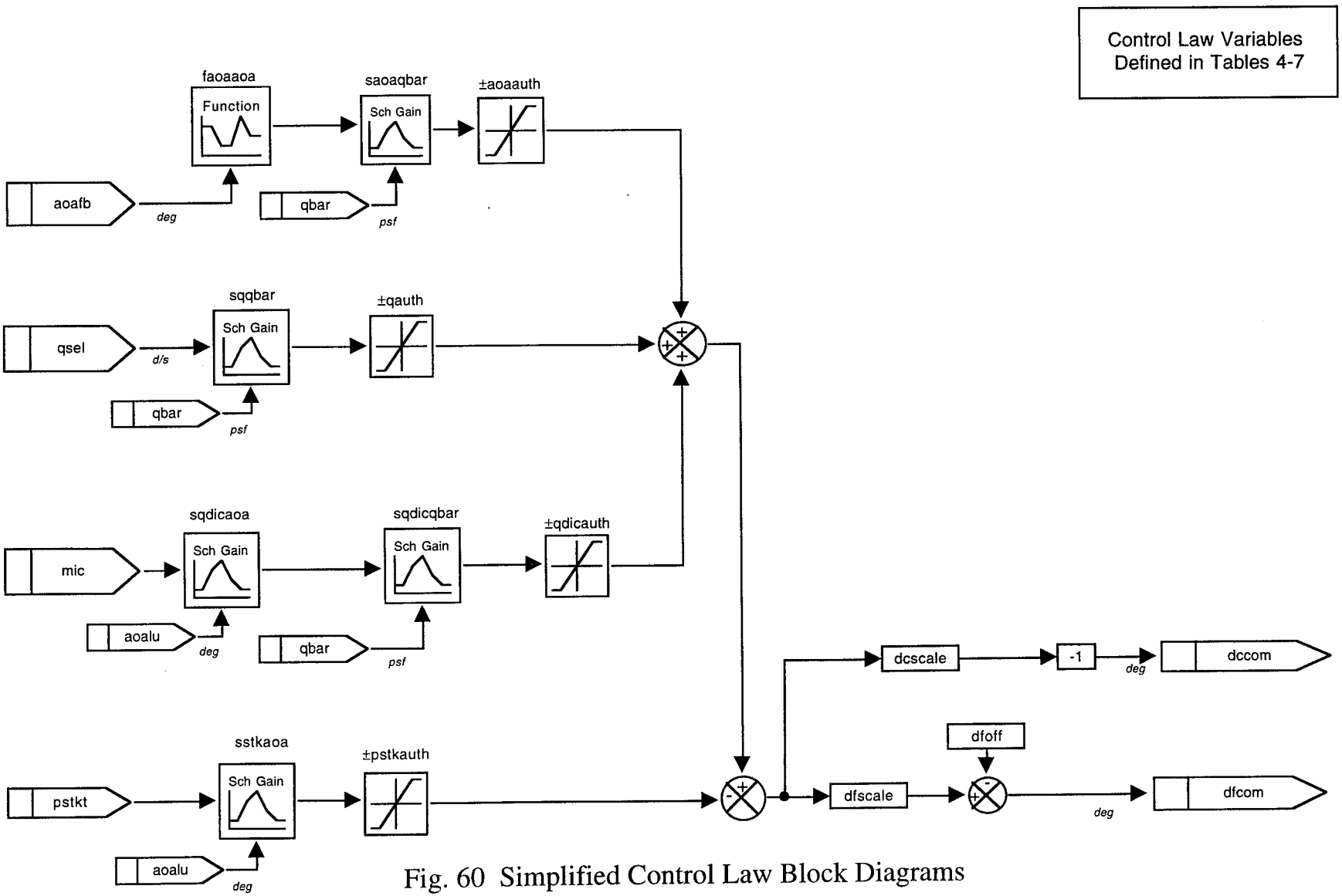

Fig. 60 Simplified Control Law Block Diagrams

a. Longitudinal

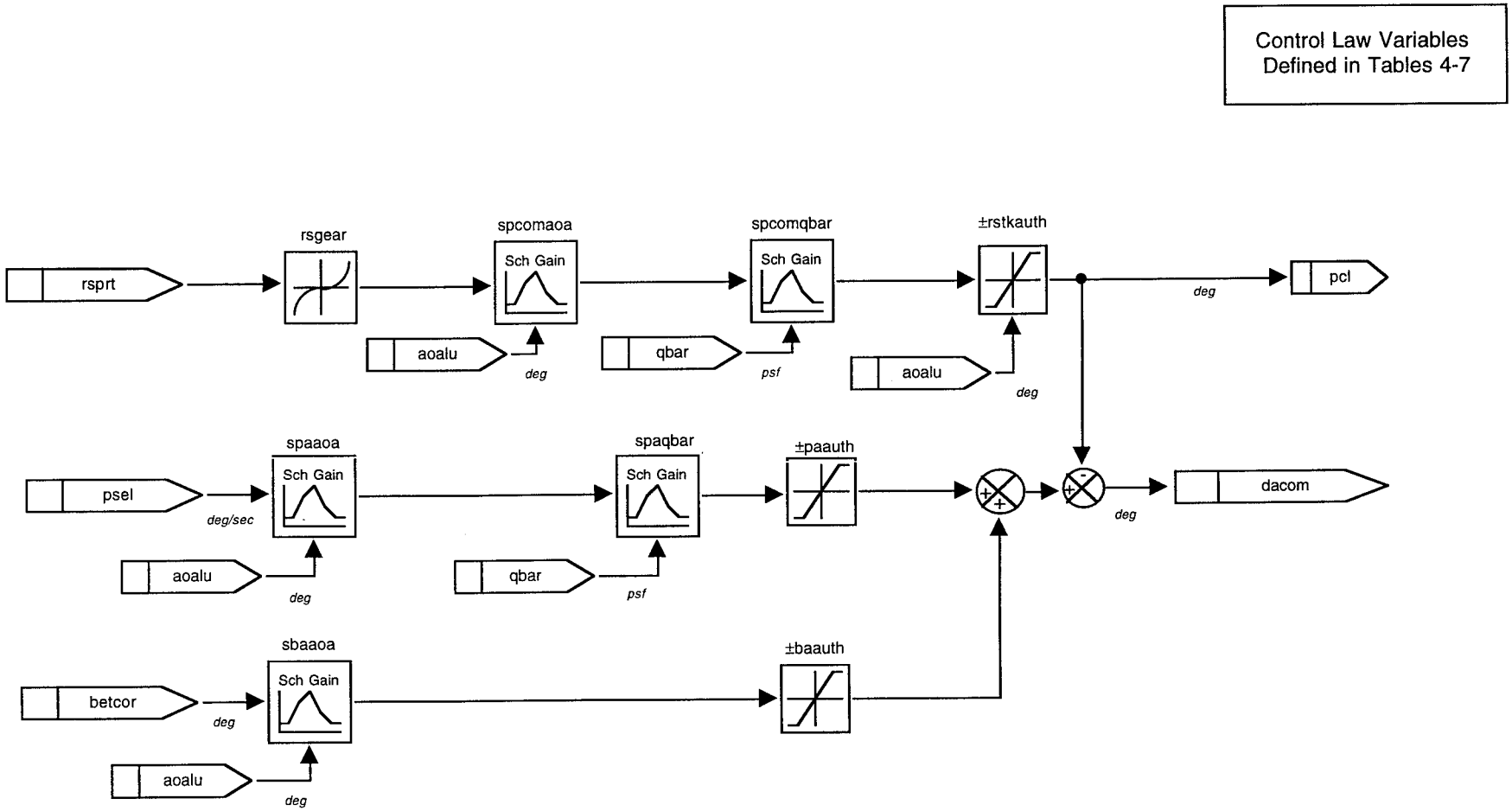

Fig. 60 Simplified Control Law Block Diagrams

b. Lateral

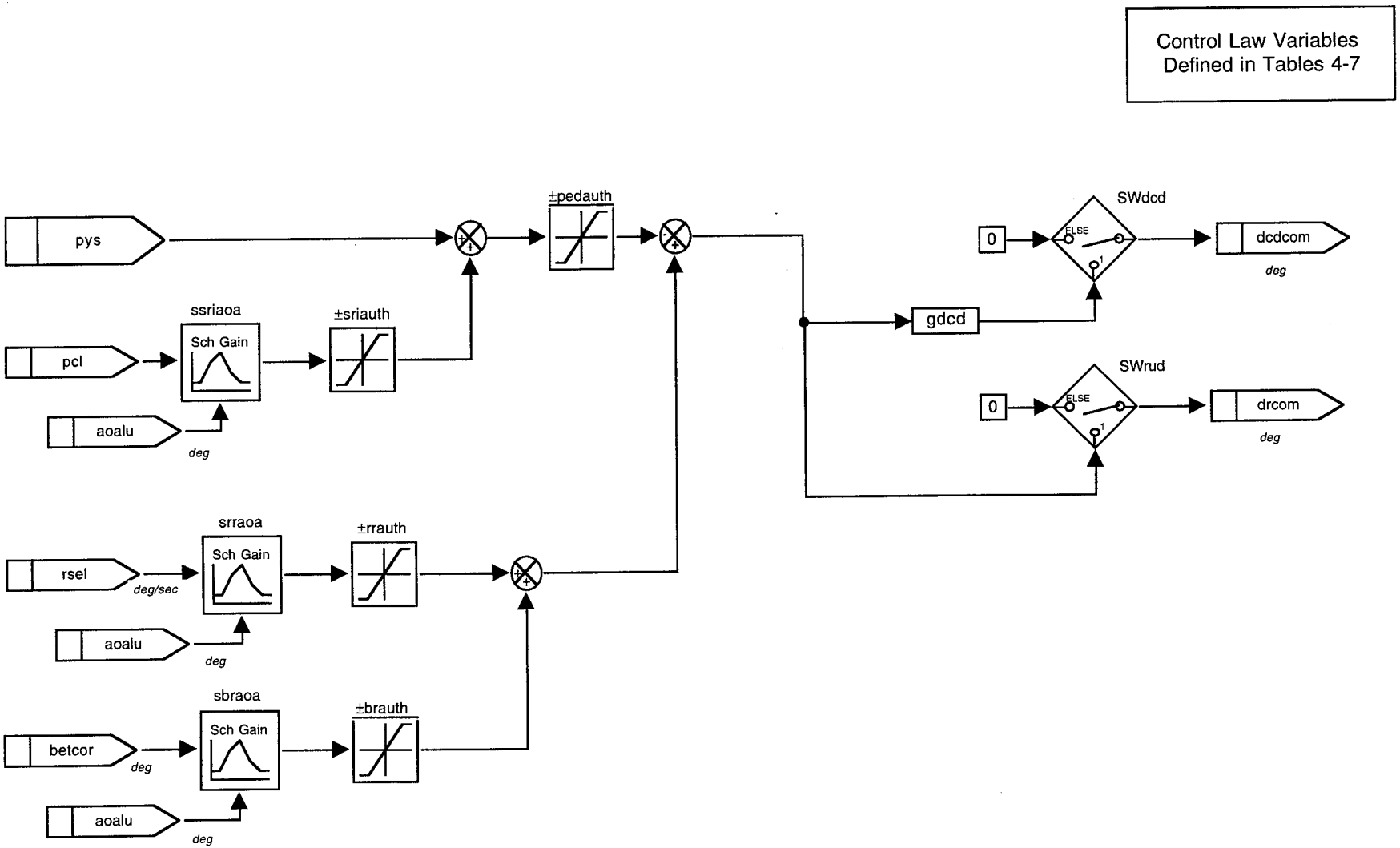

Fig. 60 Simplified Control Law Block Diagrams

c. Directional

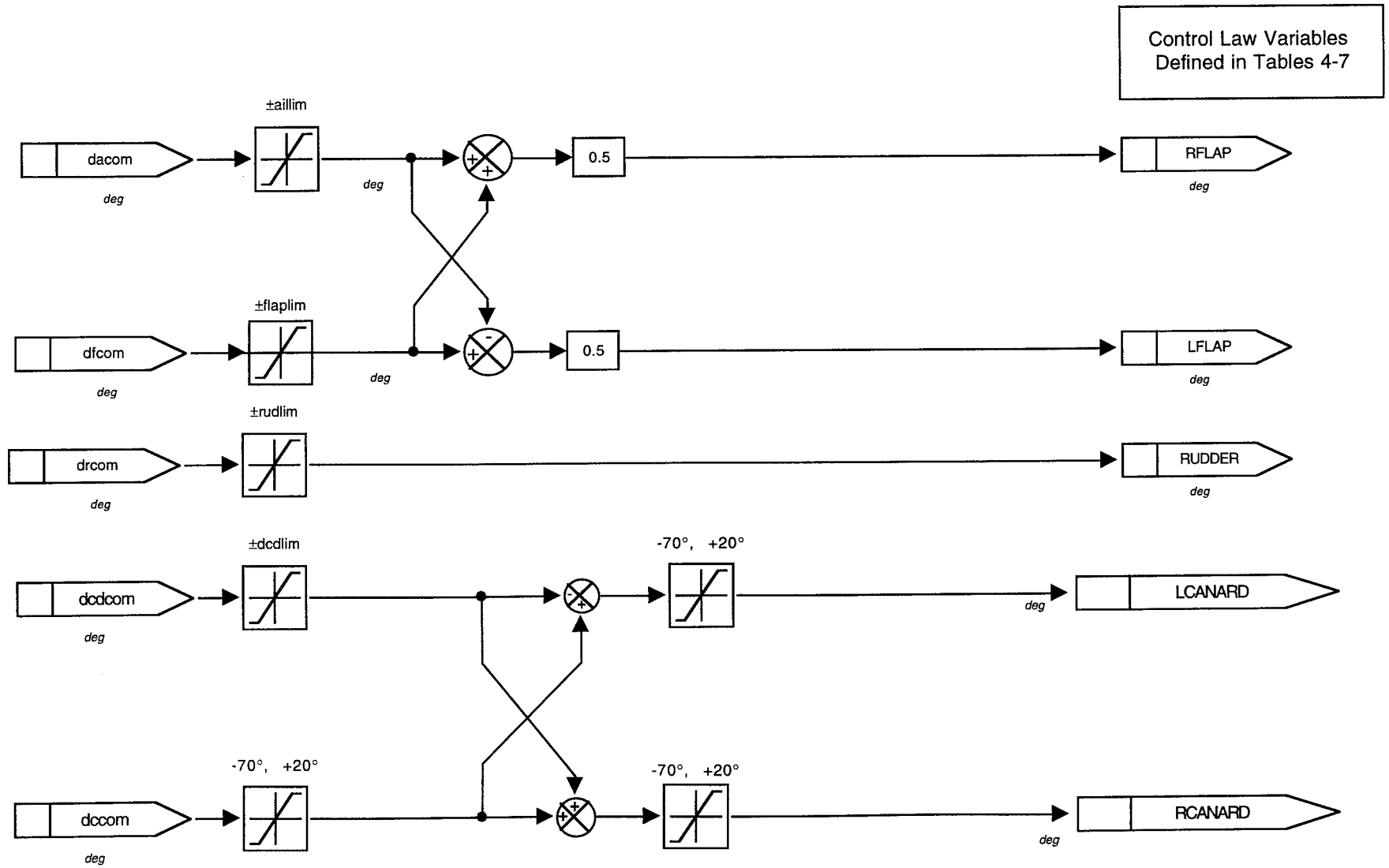

Fig. 60 Simplified Control Law Block Diagrams

d. Actuator Commands

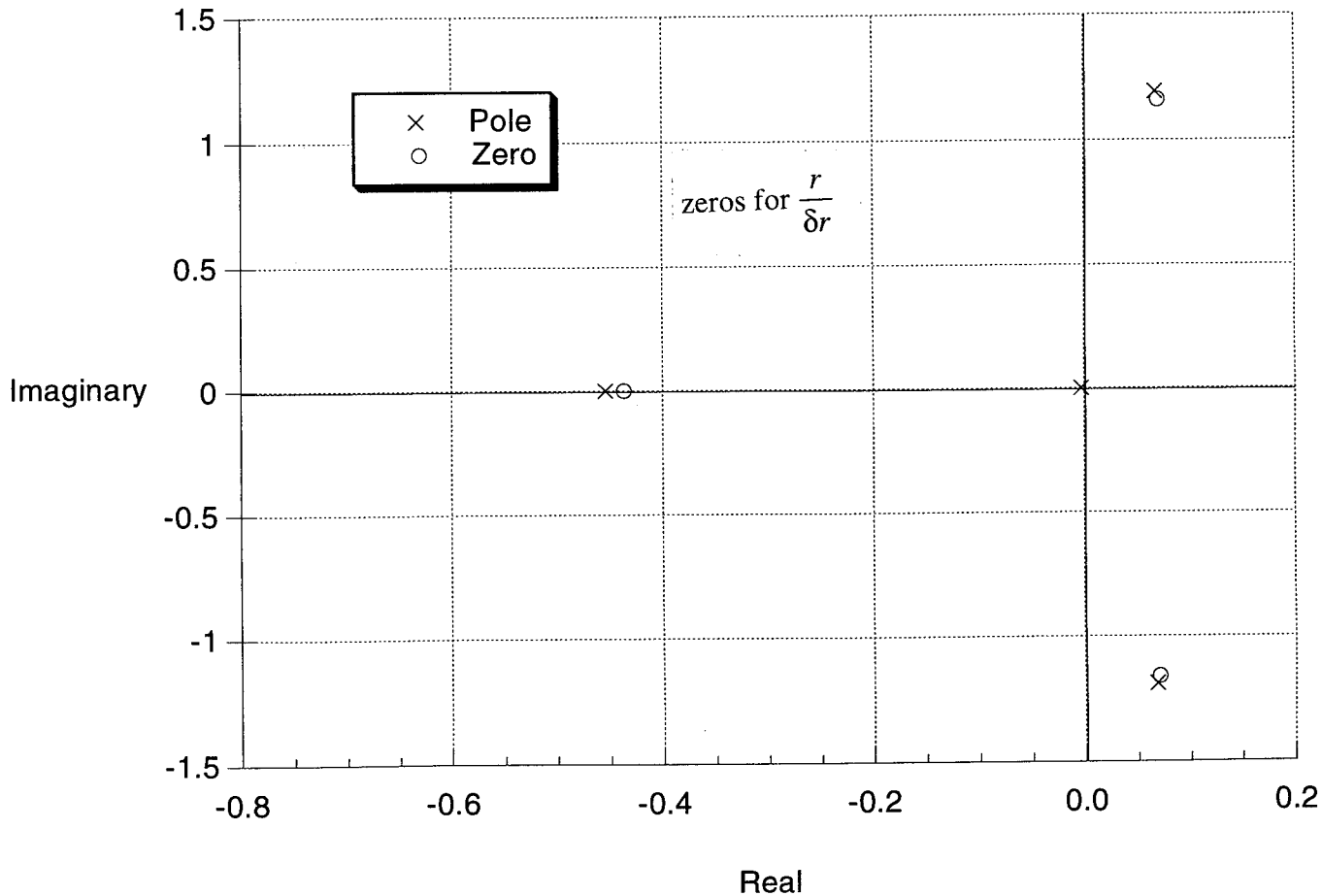

Fig. 61 Open Loop Poles for 100% Vertical Tail

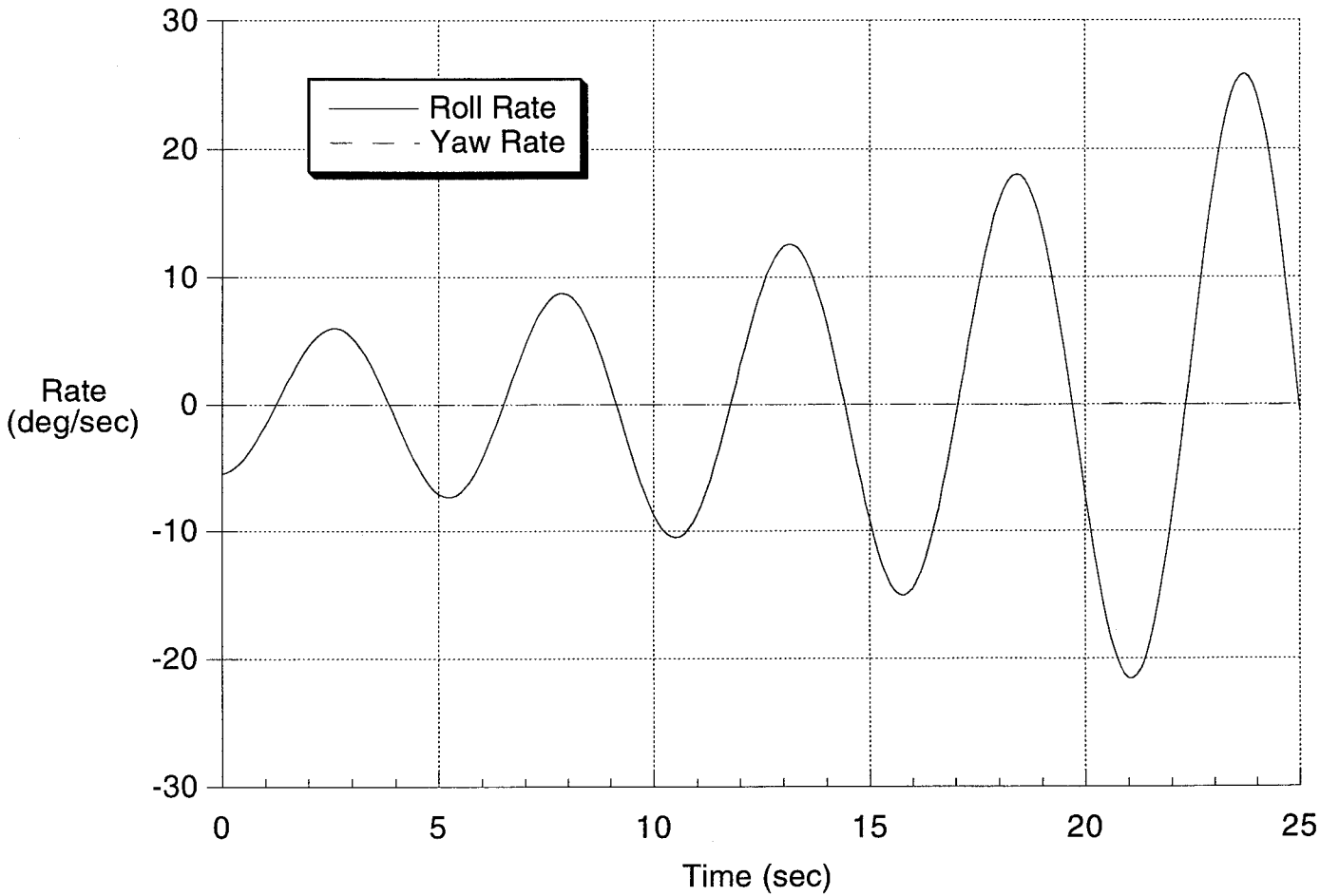

Fig. 62 Open Loop Response to Aileron Impulse with 100% Vertical Tail

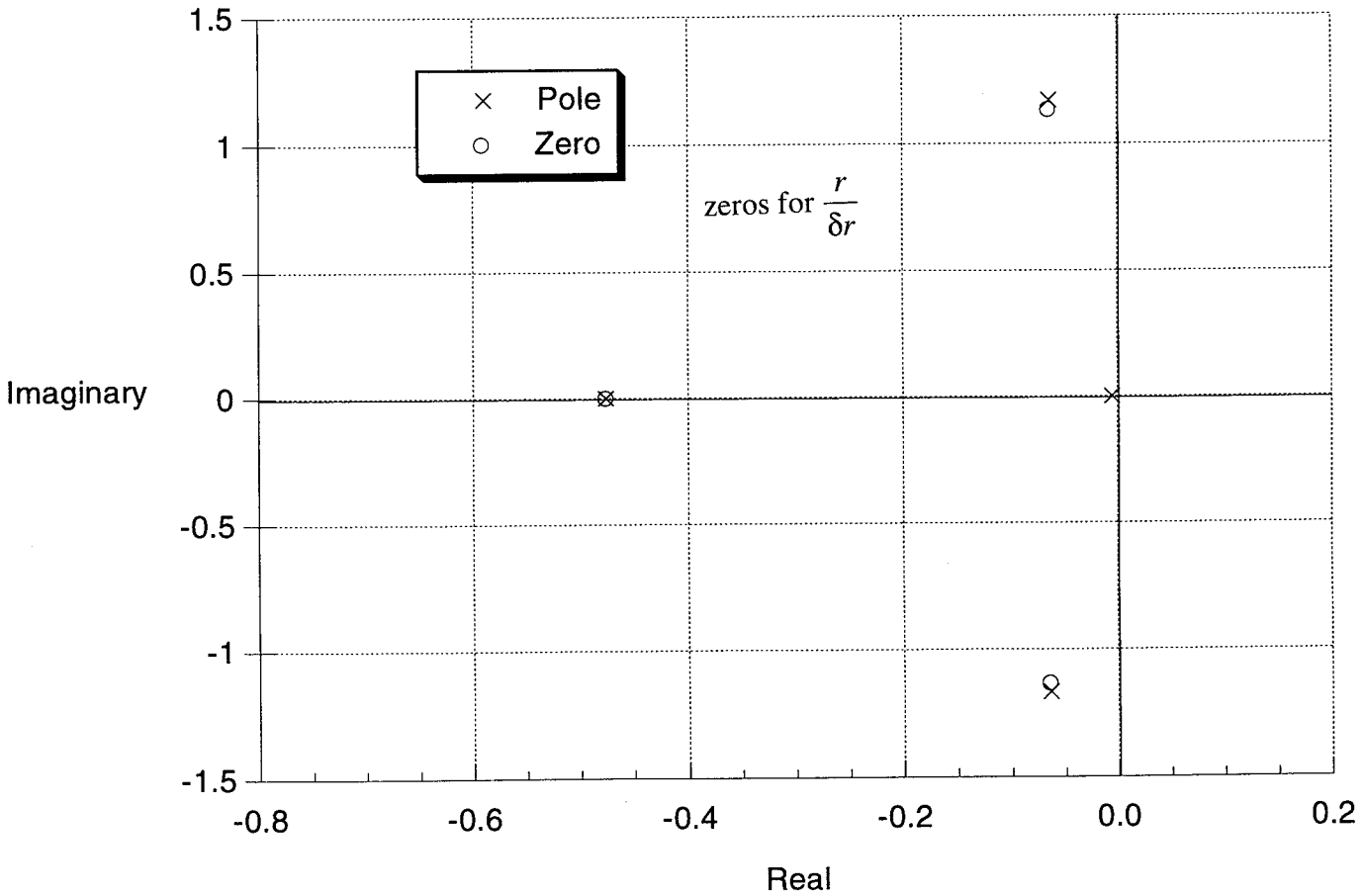

Fig. 63 Closed Loop Poles for 100% Vertical Tail

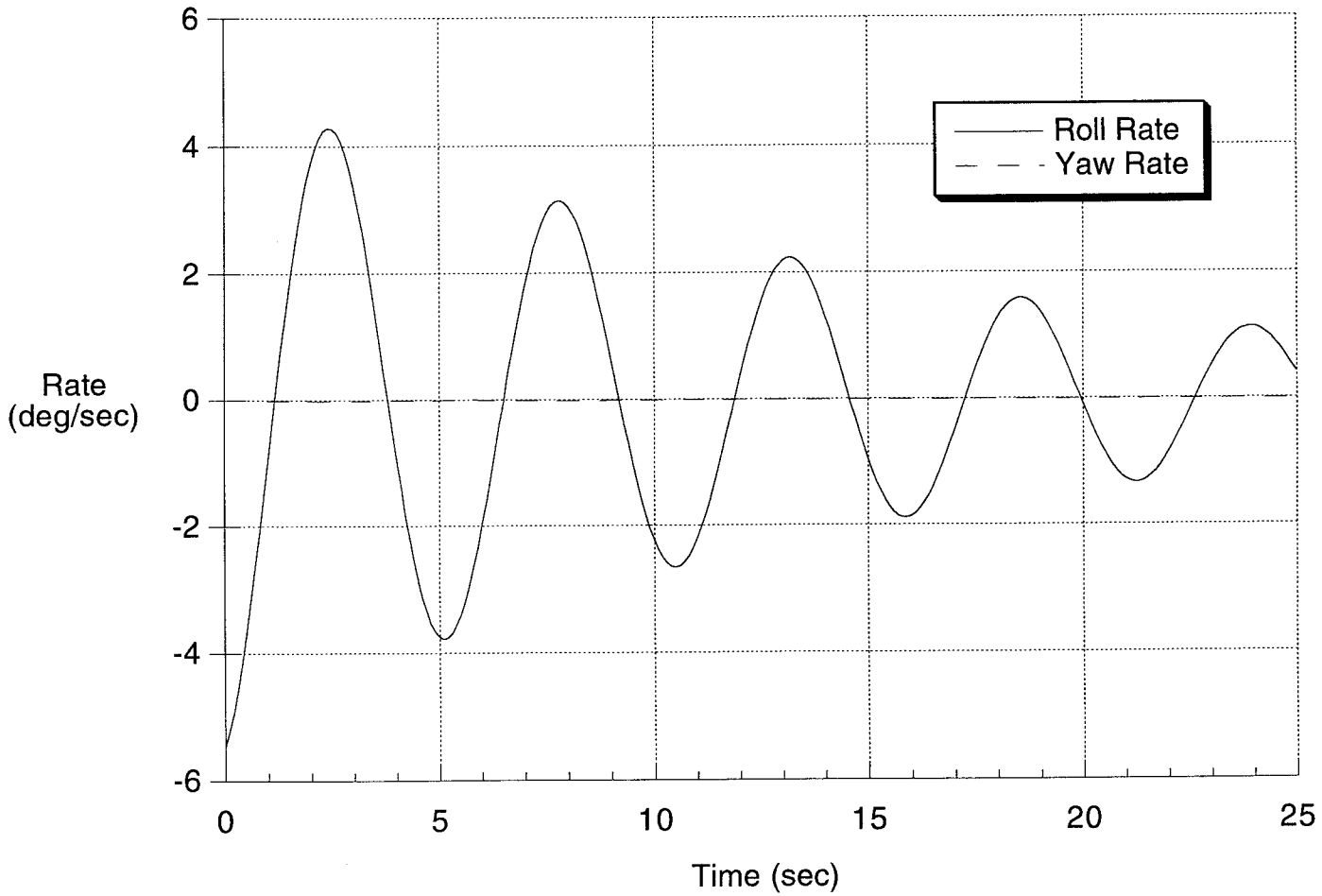

Fig. 64 Closed Loop Response to Aileron Impulse with 100% Vertical Tail

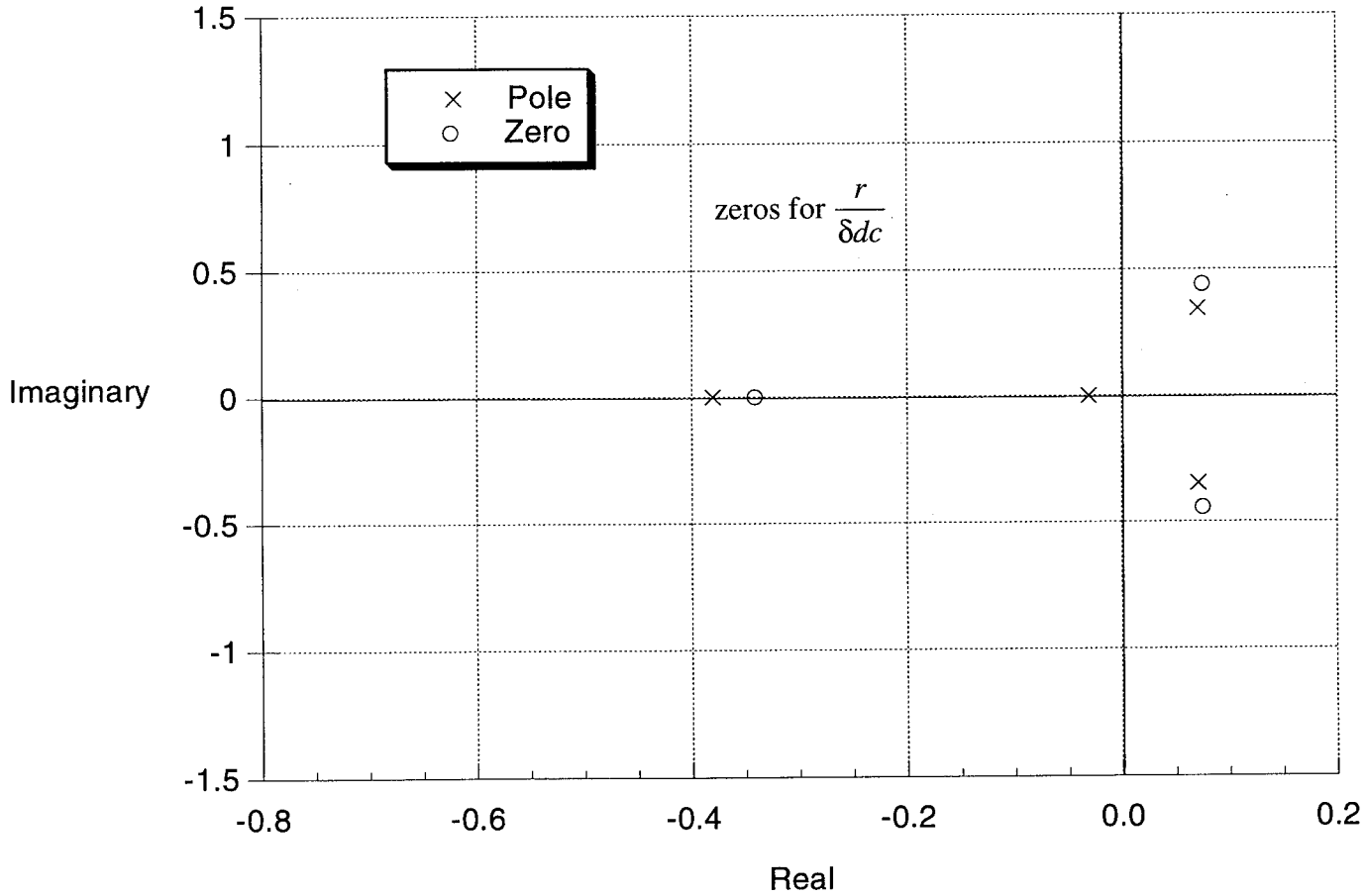

Fig. 65 Open Loop Poles for 20% Vertical Tail

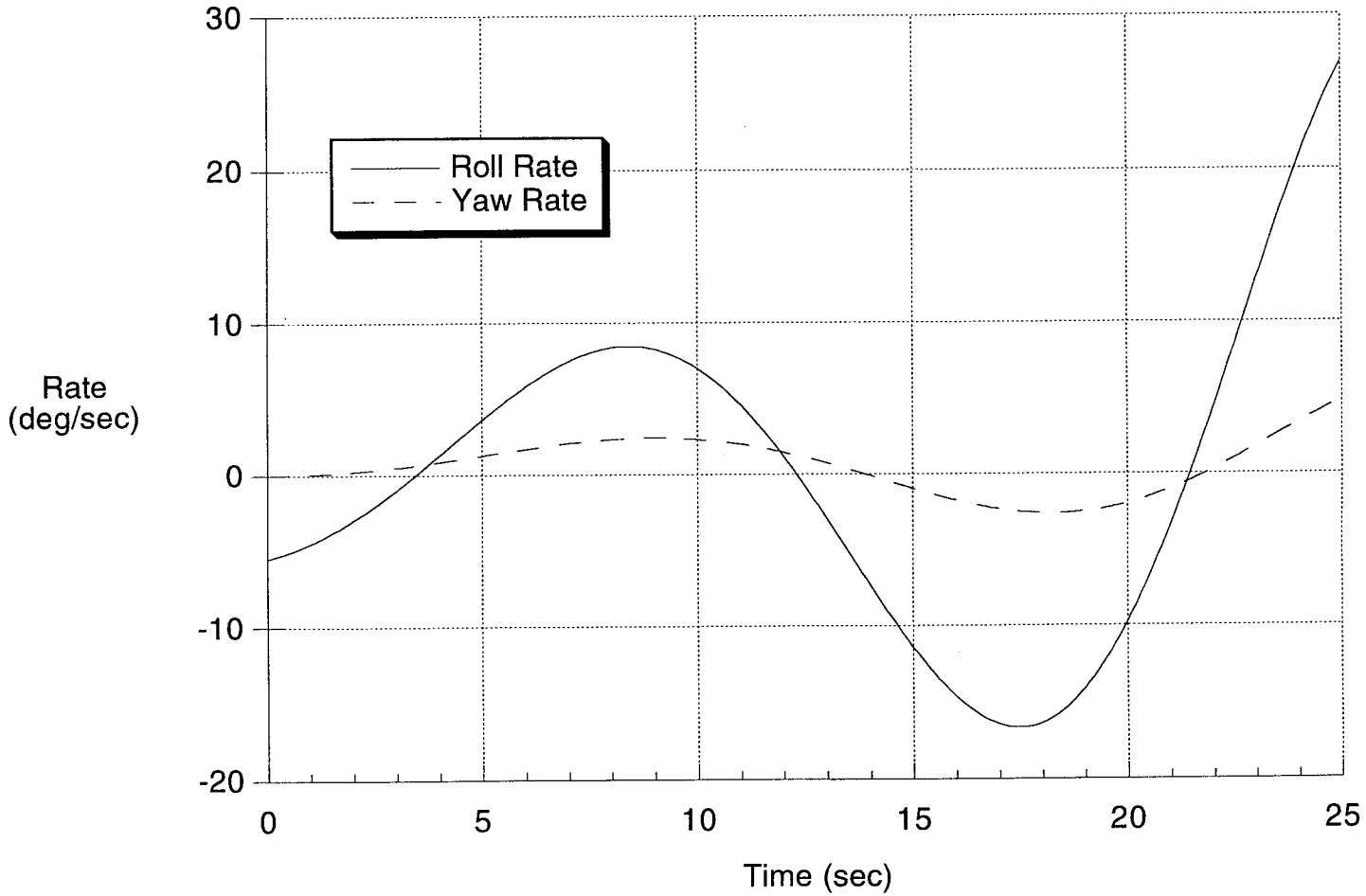

Fig. 66 Open Loop Response to Aileron Impulse with 20% Vertical Tail

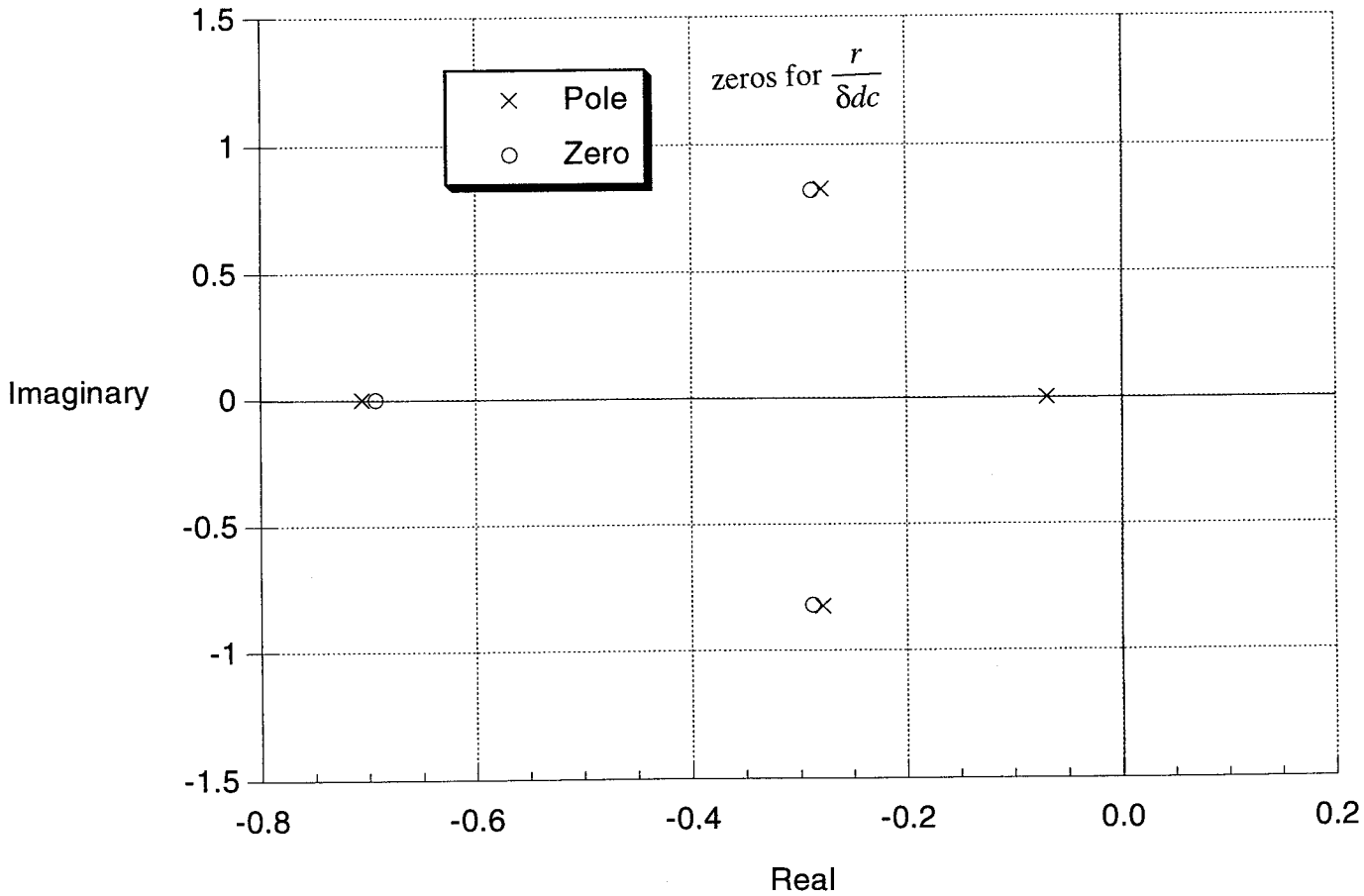

Fig. 67 Closed Loop Poles for 20% Vertical Tail

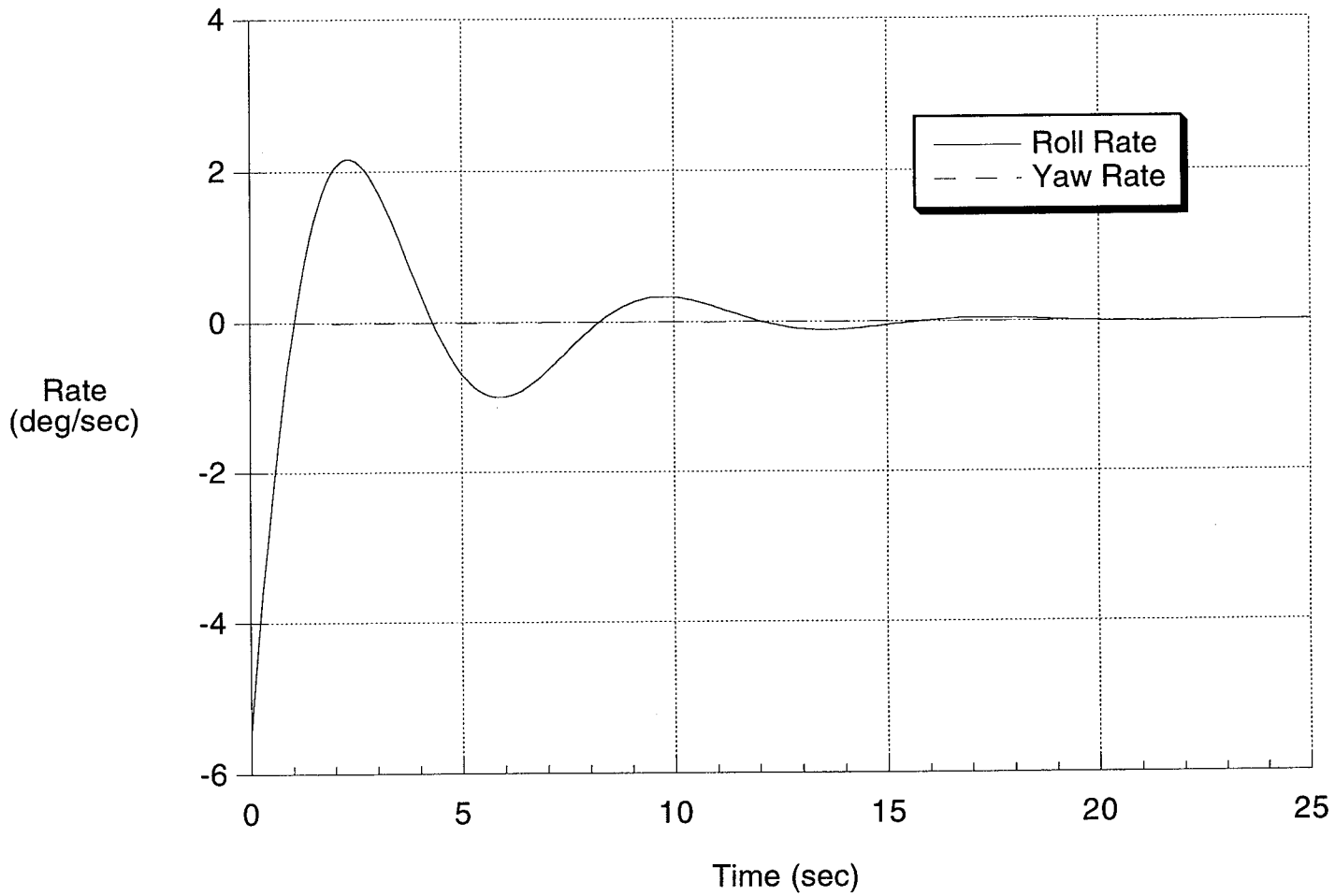

Fig. 68 Closed Loop Response to Aileron Impulse with 20% Vertical Tail

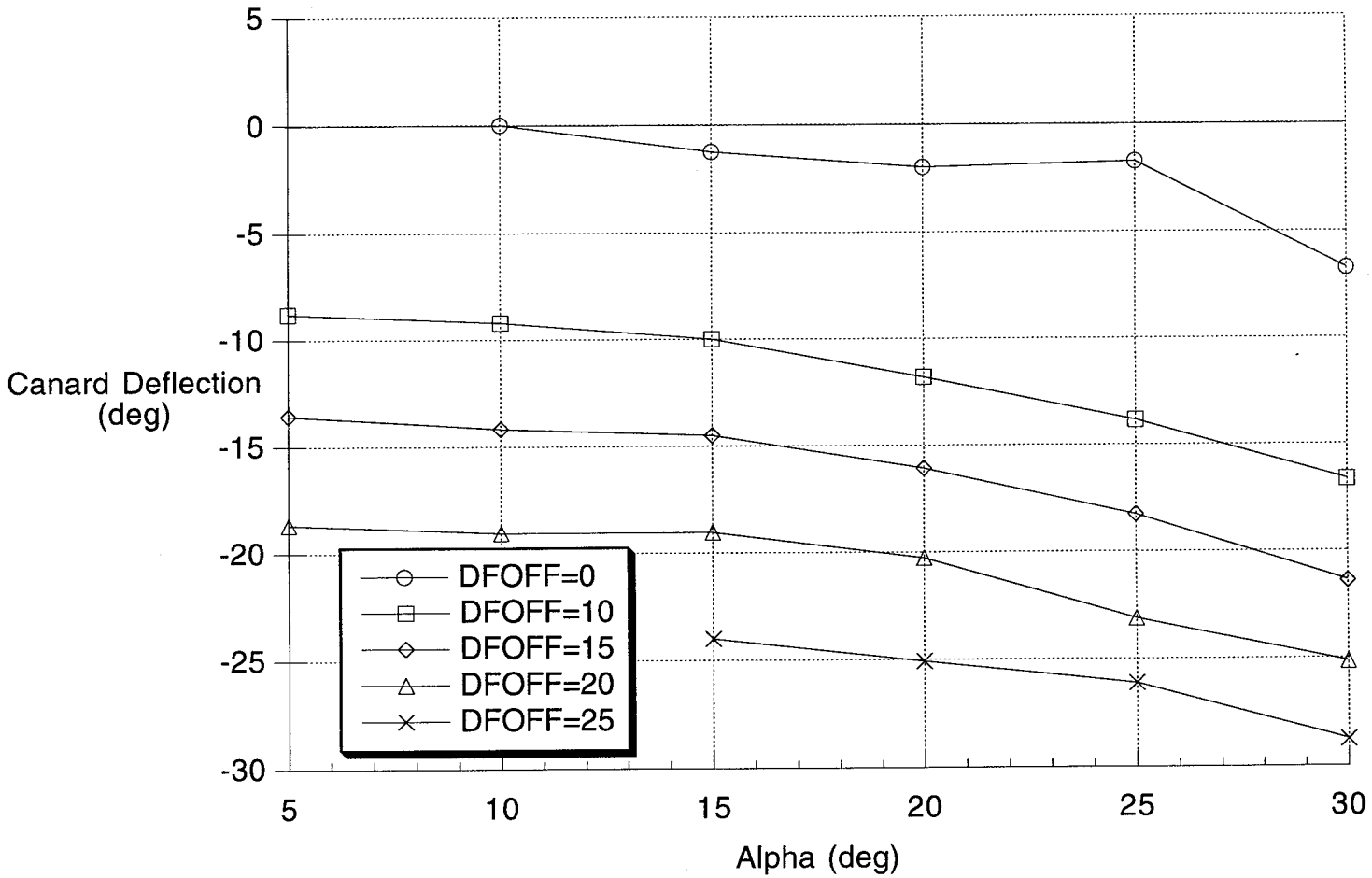

Fig. 69 Trim Symmetric Canard Deflection as a Function of Control Law ParamterDFOFF

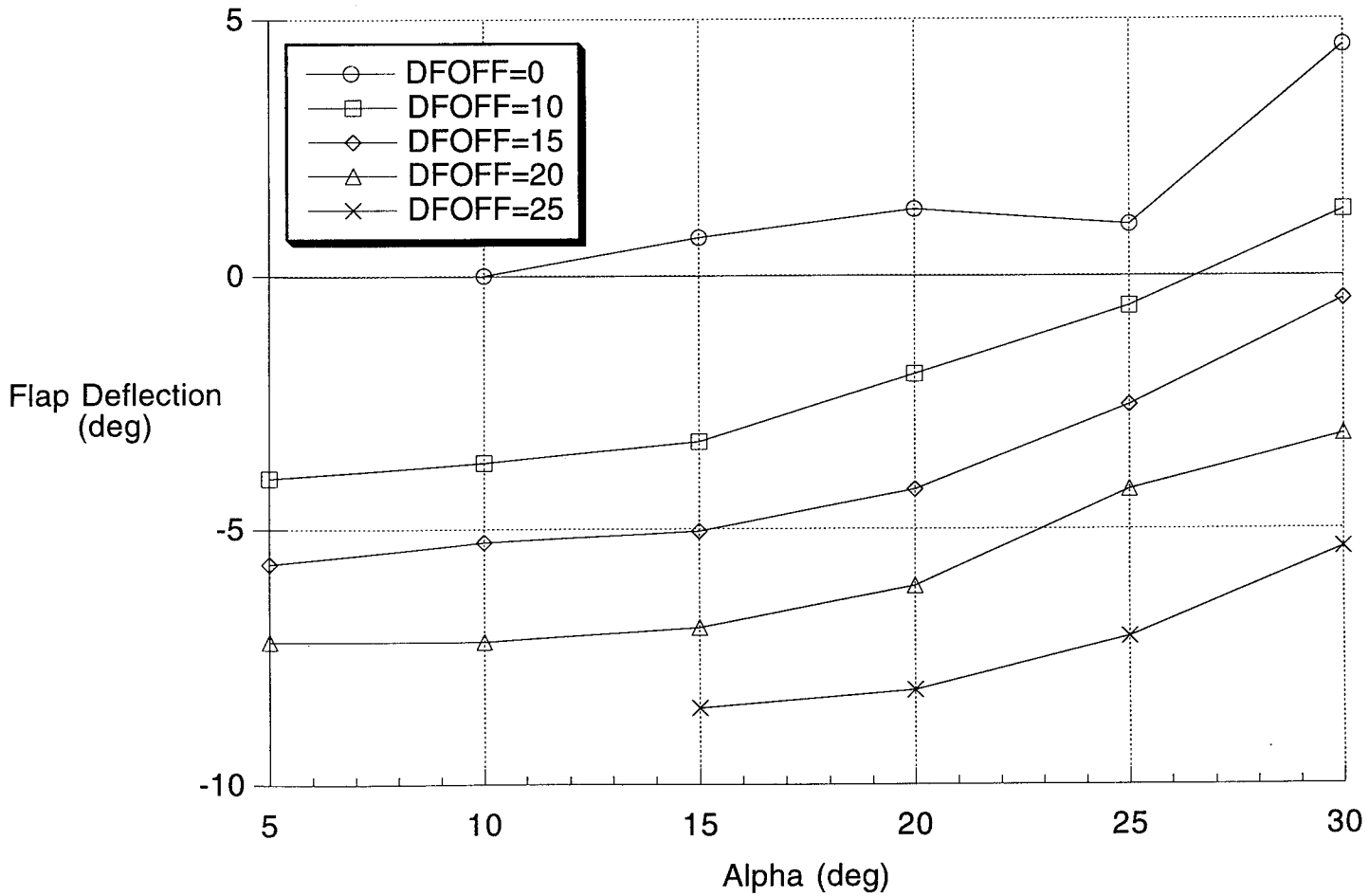

Fig. 70 Trim Symmetric Flap Deflection as a Function of Control Law Parameter DFOFF

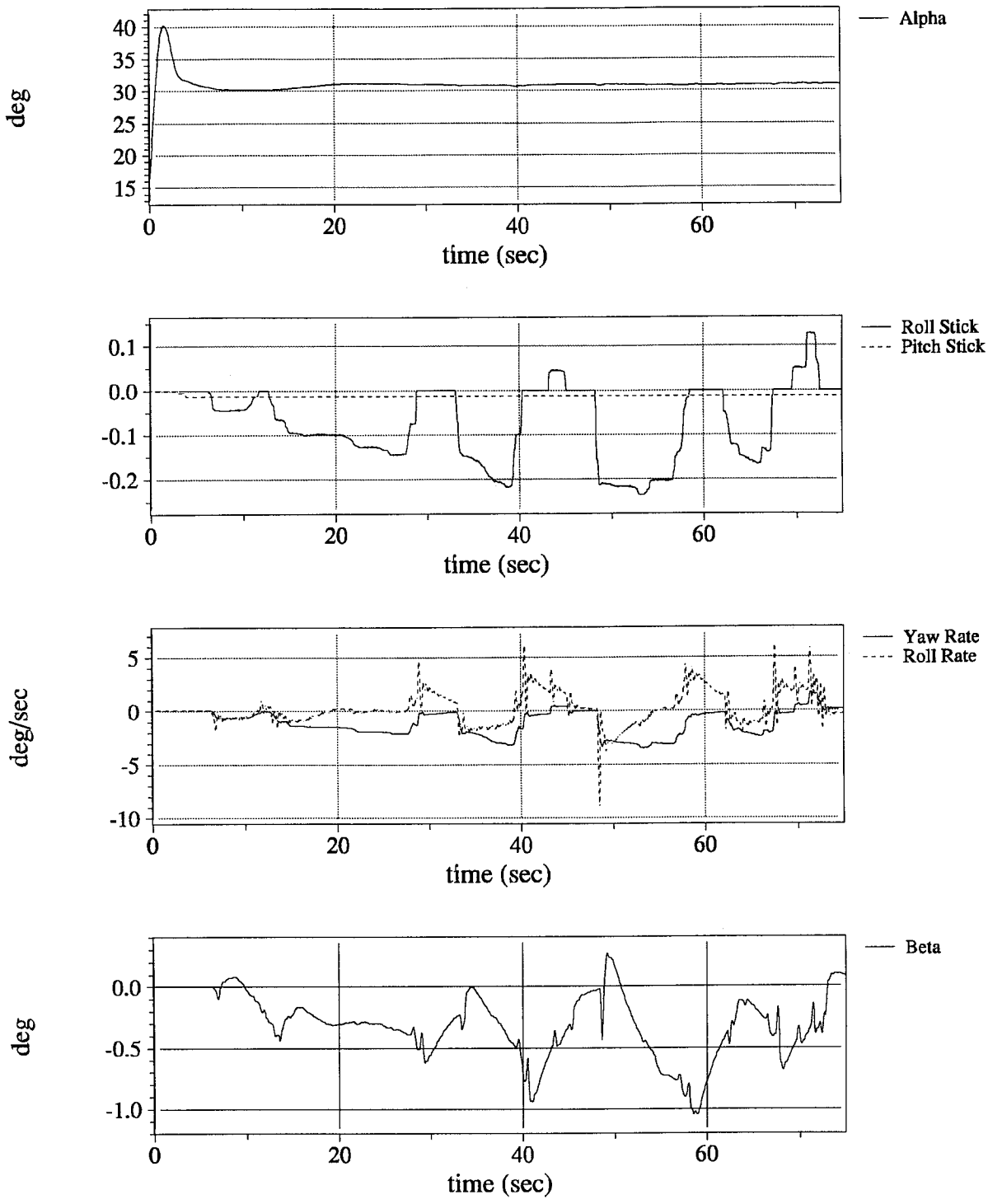

Fig. 71 Drop Model Simulation: Demonstration of Tailless Controllability at $\alpha = 30°$

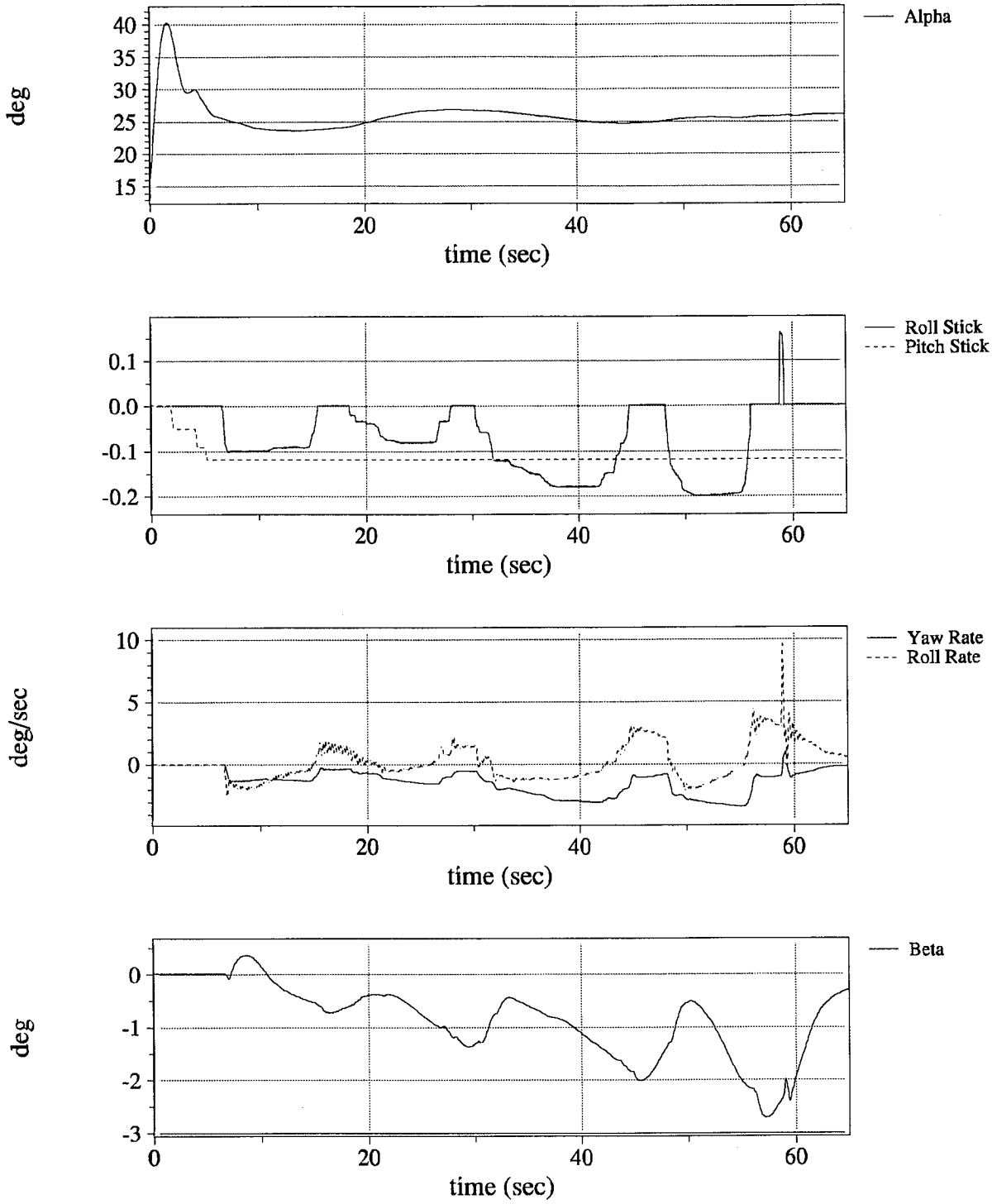

Fig. 72 Drop Model Simulation: Demonstration of Tailless Controllability at $\alpha = 25°$

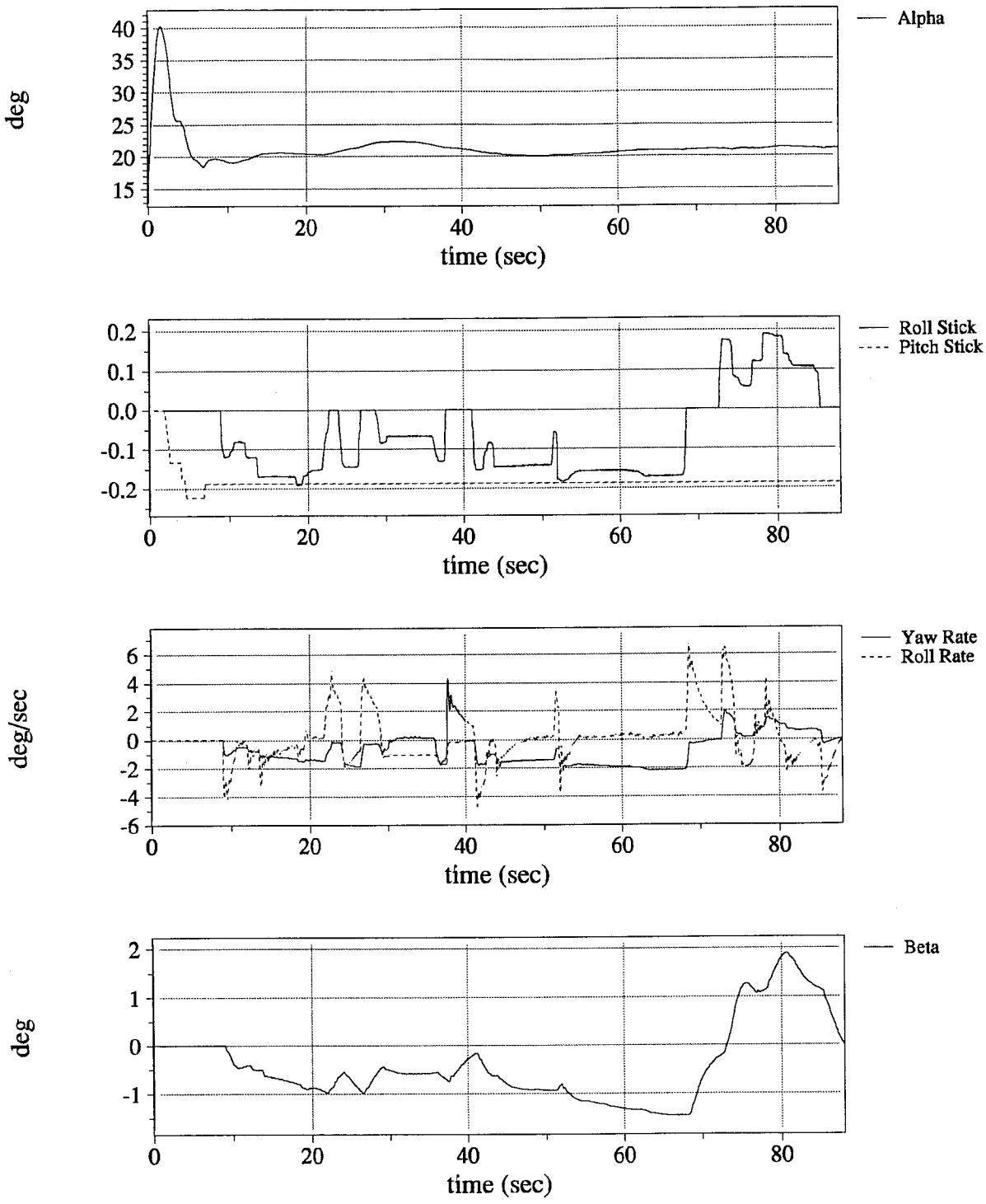

Fig. 73 Drop Model Simulation: Demonstration of Tailless Controllability at $\alpha = 20°$

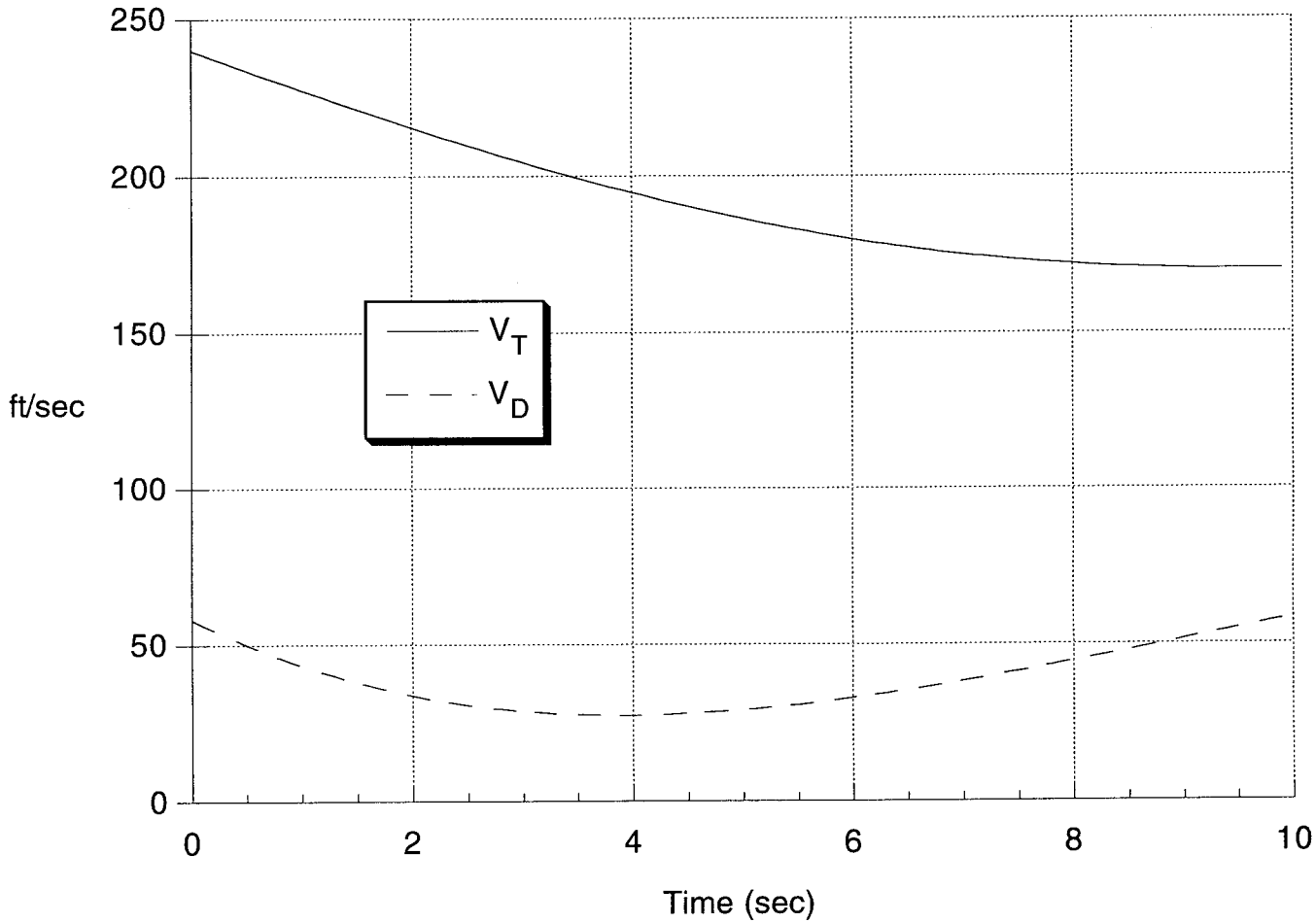

Fig. 74 Time History of Flare From $\alpha = 20°$ to $\alpha = 30°$